INTERACTION OF ELECTROMAGNETIC WAVES WITH BIOLOGICAL TISSUE

By

Inas El Babli

A Thesis
Submitted to the Faculty of Graduate Studies
in Partial Fulfillment of the Requirements
for the Degree of

Doctor of Philosophy

Department of Electrical and Computer Engineering
University of Manitoba
Winnipeg, Manitoba, Canada 2001

THE UNIVERSITY OF MANITOBA

FACULTY OF GRADUATE STUDIES

*****

COPYRIGHT PERMISSION

INTERACTION OF ELECTROMAGNETIC WAVES WITH BIOLOGICAL TISSUE

BY

INAS EL BABLI

A Thesis/Practicum submitted to the Faculty of Graduate Studies of The University of Manitoba in partial fulfillment of the requirement of the degree

Of

DOCTOR OF PHILOSOPHY

Abstract

The interaction of electromagnetic waves with biological tissue is investigated. Two problems in particular are studied. The first is three-dimensional scattering from biological tissue taking into consideration its dispersive nature. The other problem that is investigated is the three-dimensional reconstruction of the dielectric properties of a body from the scattered field data resulting from interrogation with electromagnetic waves.

The symmetric condensed node transmission line matrix method (SCN TLM) is used to study three-dimensional scattering from biological tissue. To simulate the dispersive nature of biological tissue, a second order Debye equation approximation of the permittivity in the frequency domain is used in a modified TLM technique. In this technique, the scattering matrix is independent of the dielectric properties of the medium, which are accounted for via lumped equivalent networks or sources connected to the nodes. These equivalent sources are calculated at each time step and included in the scattering procedure of the TLM. To check the validity and accuracy of the modified TLM technique for dispersive homogeneous and nonhomogeneous dielectric bodies, some of the results of the numerical simulations are compared to those obtained analytically. Assuming a nondispersive nature of biological tissue, the nondispersive or stub-loaded SCN TLM method is used to obtain the near field data and hence the specific absorption rate (SAR) distribution. The results of both cases are compared. The modified TLM technique is then applied to a nonhomogeneous and geometrically complex

dispersive dielectric body, which is the human head.

To estimate the complex permittivities of three-dimensional inhomogeneous dielectric bodies, the unrelated illumination method is used. This method, which has been tested before with two-dimensional bodies, is extended to handle three-dimensional inhomogeneous dielectric bodies. The method utilizes the method of moments (MoM) to discretize the nonlinear integral equation, which relates the scattered field data and the complex permittivity. Yet, it differs from the other reconstruction techniques in that the way of acquiring information helps overcoming the ill-posedness nature of the problem. This is maintained by the proper arrangement of the polarization and the direction of the incident electric fields aiming to illuminate the body with a group of unrelated incident fields. Numerical simulations are carried out to assess the method and to test its robustness in the presence of measured data uncertainties.

Acknowledgments

I would like to express my deepest gratitude to Professor Sebak for his faithful guidance, valuable advice, directive comments and continuos supervision and encouragement throughout the course of this research.

Special recognition to the members of my supervising committee for their constructive comments and suggestions. Also, I would like to express my heart felt thanks to the faculty of the Electrical Engineering Department, University of Manitoba and to my colleagues for providing a supportive and friendly environment.

I would also like to thank my husband and my kids for their patience, endurance and everlasting support. Special thanks to all of my family and friends for their spiritual assistance.

TO MY PARENTS TO WHOM I OWE EVERY

SUCCESS IN MY LIFE

TABLE OF CONTENTS

LIST OF FIGURES

LIST OF TABLES

CHAPTER 1

Introduction

1.1 Introduction:

The increased usage of high frequency devices by the society for a variety of purposes has made it imperative to be able to quantify the absorption of electromagnetic energy in the human body. Such knowledge is indispensable if one is to either selectively apply electromagnetic waves for therapeutic purposes or determine if the electromagnetic fields emitted by a device are harmful. Because ethical considerations make electromagnetic exposure of humans for experimental purposes difficult, it is necessary to develop realistic computer or engineering models. Computer simulations could then be carried out to obtain the required information [1].

Most of nature's phenomena can be modeled using mathematical models. Models in general are used to establish a relationship between the input to a system and the output of the system [2]. Models allow for better understanding of the system response as well as the possibility of investigating the effects of various parameters involved on the system output. In order to build a model, the domain, whether it is frequency or time domain, at which the problem will be solved has to be chosen. In addition, a certain

mathematical formulation has to be adopted. Both of these points are usually related to the problem under consideration and the information or data required as an output of the used model. Numerical techniques are essentially mathematical models that make use of the availability and advances in the high-speed computer technology.

1.2 Domain-Classification of Numerical Techniques:

There are several classification schemes for numerical techniques. One criterion for classification is the domain in which the actual physical problem is defined. If the problem is defined in the time domain, then the method is described as a time domain method. In this case, the computational domain is both space and time dependent. Alternatively, the frequency domain may be chosen, leading to the frequency domain methods. In this case the computational domain is only space dependent as the problem is solved at a single frequency. The time domain formulation is suitable for studying transients or obtaining the response over a wide frequency range. The latter can be obtained using Fourier transformation of the time domain information. The frequency domain formulation is used for studying the steady state response at a single frequency. The choice of the domain is usually based on the efficiency of handling a particular problem.

To investigate electromagnetic field problems, techniques belonging to both the frequency and time domain have been used. For most antenna applications and radar cross section analysis, frequency domain results are usually required. For certain electromagnetic compatibility (EMC) problems, the transient response may be required. Also, the nature of the material parameters affects the choice of the solution domain. The

time domain formulation is preferred for problems that include nonlinear materials. On the other hand frequency dependant or dispersive materials, although require the use of convolution in time domain modeling, are easily treated using frequency domain formulation.

1.3 Formulation-Classification of Numerical Techniques:

The starting point in modeling electromagnetic field problems is usually Maxwell's equations, which provide the basis for studying various electromagnetic phenomena. Two kinds of mathematical formulations can be used to describe electromagnetic field problems based on the form in which Maxwell's equations are given. These are the integral equation formulation and the differential equation formulation.

1.3.1 Integral Equation Formulation Based Techniques:

The integral equation formulation can be used to solve open problems and treat complex geometries. The appropriate selection of a Green's function for the problem under consideration is the starting point for the integral equation formulation. The formulation reduces the problem into an integral equation in terms of unknown currents and these Green's functions. This usually results in a system with a dense matrix equation. Assuming a time harmonic variation, the integral equation can be formulated in the frequency domain. The method of moments (MoM) [3] and the geometrical theory of diffraction (GTD) [4] are considered the leading methods in the integral equation

frequency domain formulation. The method of moments is used to discretize the integral equation thus allowing for a numerical solution for the problem at a single frequency. For frequencies above the resonance range, the geometrical theory of diffraction may be used. The integral equation can also be formulated in the time domain [5]. In such a case, it allows for the study of transients in the system. The integral equation formulation can further be divided into surface integral equation formulation and volume integral equation formulation. The surface and volume integral equation formulations have been widely used to analyze electromagnetic radiation and scattering problems. A detailed review of the numerical methods based on the integral equation formulation can be found in [6].

1.3.2 Differential Equation Based Techniques:

The differential equation formulation can be used to solve closed inhomogeneous problems more easily than the integral equation formulation. Also, as the complexity of the problem increases, the differential equation based formulations become more computationally efficient than the integral equation based formulation. The numerical solution of the differential equation formulation can be obtained via such techniques as the finite difference time domain (FDTD) [7] or the transmission line matrix method (TLM) [8], both of which are time domain methods. The finite difference time domain is based simply on the application of the central finite difference in both space and time to Maxwell's equations. The transmission line matrix method is based on the equivalence between Maxwell's equations for the electric and magnetic fields in a medium and the equations for the voltage and current on a network of transmission lines. Both approaches

lead to systems of algebraic equations that must be solved at each time step. They also require discretization of the entire simulation space in which a non-zero field distribution exists. For open region problems, they require the application of absorbing boundary conditions to truncate the simulation space to a reasonable size. Both techniques can be used as an electromagnetic modeling, simulation and analysis tools. Each of these techniques has particular advantages over the other, depending on the specific problem being studied [9]-[11].

The differential equation form of Maxwell's equations can also be formulated in the frequency domain. The finite element (FE) method is a widely used technique that belongs to this category [12]. Because of the type of the space discretization, which is tetrahedral elements for three-dimensional problems, the method can handle a wide range of geometries. Another method that belongs to this category is the finite-difference (FD) method [13]. Both of these techniques have been widely used to analyze different structures [14]-[17].

1.4 Biological Aspects of Electromagnetic Waves:

The purpose of this thesis is to study the interaction of electromagnetic waves in particular microwaves with biological tissue. The wide use of electromagnetic and microwave devices in our daily life has raised a lot of debate regarding the effects of electromagnetic radiation on living material. How much is absorbed by human tissue after an exposure and whether this absorbed energy is of any risk or can cause any mutation to human cells. In order to answer the latter part we have to find an accurate method to measure the energy deposited to a human tissue after an exposure to

microwave radiation. The dielectric properties of the biological or human tissue are frequency dependent. Thus, for accurate simulations, the dispersive nature of biological tissue has to be taken into account. Further studies can be carried out to obtain the safety exposure levels. Since microwave radiation is a non-ionizing low power radiation and due to the lack of a solid proof of being harmful, research has been and is being carried on regarding the possibility of its use as an imaging technique.

Two main issues are going to be studied in this thesis. The first is scattering and power absorption to obtain the energy deposited in dispersive biological tissue. The second is inverse scattering to explore the possibility of using microwaves in imaging or reconstruction of the dielectric properties of inhomogeneous dielectric bodies. Two different numerical techniques are used, the transmission line matrix (TLM) method and the method of moments (MoM). The choice is made based on the applicability and the efficiency of handling each respective problem.

1.5 Thesis Outline:

Chapter 2 provides a review of the TLM method and its use as a time domain numerical technique to solve various electromagnetic problems. The use of transmission lines to describe the behavior of electromagnetic fields in a medium is discussed. The symmetric condensed node (SCN) is presented together with the various capabilities of the TLM method. In Chapter 3, the use of SCN TLM to model dispersive media in a modified TLM technique is presented. The dielectric properties of the medium are modeled via a RC circuit. The circuit is connected to the TLM node and solved at each time step. In doing so, the scattering matrix of the TLM technique is made independent of

the medium. A circuit model is proposed in Chapter 3 to model second order Debye dielectrics. The derivation of the circuit model equivalence together with the expressions for the circuit components in terms of the second order Debye parameters are given in appendix A. The results of numerical simulations, for scattering from biological tissue, based on the SCN TLM are then presented. The validity and accuracy of the method are first presented using results obtained analytically and results obtained using the stub-loaded or nondispersive SCN TLM method. The modified TLM technique is then applied to various nonhomogeneous and geometrically complex dispersive bodies.

In Chapter 4, the forward and inverse scattering formulation and their use in the reconstruction of dielectric bodies are presented. Ill-posed problems as well as the different methods of regularization, that can be employed, are defined. A review of the various techniques used in microwave imaging is given in this chapter. In Chapter 5, we start with the discretization of the integral equation formulation. This is followed by a discussion of the common reconstruction procedure available. The unrelated illumination method is then presented as a tool for the reconstruction of the dielectric property distribution of inhomogeneous dielectric bodies. The results of numerical simulations to assess the capabilities and robustness of the unrelated illumination are presented. Finally, conclusion and future work are given in Chapter 6.

CHAPTER 2

The Transmission Line Matrix Method

2.1 Introduction:

The Transmission Line Matrix (TLM) method is a powerful numerical technique for solving electromagnetic field problems. The method uses transmission line networks to represent the behavior of electromagnetic fields [18]-[20]. In this model, voltages and currents behave in the same way as electric and magnetic fields. Therefore, concepts of transmission line analysis can be used to describe the electromagnetic phenomenon. The TLM method uses scattering and transmission matrices to simulate the propagation of electromagnetic fields. The simulation space is divided into a mesh of transmission lines interconnected at discrete points in space. At each of these points, the incident and reflected pulses are scattered and transmitted to other points of the mesh.

A simple two-dimensional version of the TLM method can be obtained by applying Huygens' principle and the conservation of energy [20]. This formulation shows the basic concepts involved in the method.

There are two distinct nodes used in modeling electric or magnetic fields. These nodes represent the two different polarizations for an electromagnetic wave propagating

in a plane [21]-[22]. These are the cases where transverse electric (TE) or magnetic (TM) field is perpendicular to the plane of propagation. The transmission line analogy characterizes the first case as a series node case and the second as a shunt node case. This follows from the topology of the network of transmission lines.

A three-dimensional version of the method is obtained by assembling a three-dimensional array of two-dimensional nodes. For each direction one series and one shunt node is used to represent the magnetic and electric field component in that direction [23]. The complete node describes the behavior of six field components.

Permittivity and permeability are modeled by stubs connected to the node [19]-[20]. In the shunt node case, an open-circuited stub models the relative permittivity of the region. In the series node case, a short-circuited stub models the relative permeability. In this representation the relative permittivity and permeability of the medium are isotropic and frequency independent.

The time domain TLM yields a wide-band response of the electromagnetic field problems and can be used to analyze its transient behavior [18]-[20]. The TLM algorithm follows the evolution of voltage pulses on the transmission line grid. The voltage pulses represent the discrete approximation to the field distributions. The field components are later determined as a post-processing task

2.2 Huygens' Principle and Its Discretization:

The propagation and scattering of waves in the TLM method can be viewed as the discrete equivalent of Huygens' principle [20]. According to Huygens, a wavefront W_1 at

time $t = t'$ consists of a number of secondary radiators that give rise to spherical wavelets. The envelope of these wavelets forms a new wavefront W_2 at time $t = t'+dt$. This process is shown in Fig. 2.1. In the continuous Huygens' principle, the secondary wavefronts form a circle of radius:

$$dr = vdt \tag{2. 1}$$

Where dt is the differential time step, dr is the differential radius and v is the velocity of propagation of light in the medium.

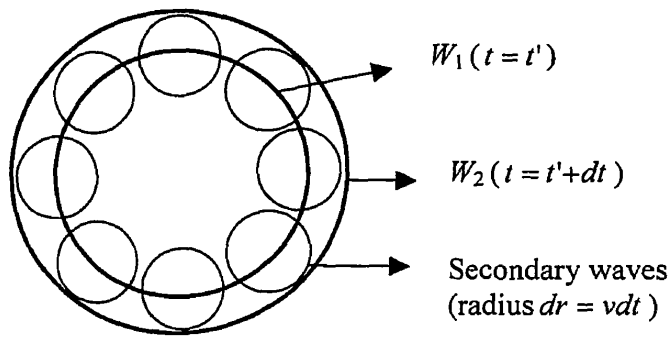

Fig. 2.1 The wavefront W_2 is formed of secondary wavefronts obtained from the primary wavefront W_1.

In the discrete equivalent, the radius of the wavefront would be:

$$\Delta r = v\Delta t \tag{2. 2}$$

where Δt is the discretized time step, Δr is the discretized spatial step and v is velocity of propagation of light in the medium. Accordingly, two-dimensional space is modeled by a

Cartesian matrix of points or nodes, separated by Δl. The time Δt is the time required for a pulse to travel from one node to the next [20].

Two different kinds of pulses exist in the mesh: pulses incident at the nodes and pulses transmitted to other nodes. The pulses scattered at a node become incident at adjacent nodes after a time delay as shown in Fig. 2.2. The delay is due to the distance between nodes and the finite speed of light. In Fig. 2.2, the pulse scattered at node *a* in the direction 4 at $t=t'$ is the same as the pulse incident on node *b* from the direction 2 at $t=t'+\Delta t$. This two-dimensional model has a network analogue in the form of a mesh of orthogonal transmission lines or a transmission line matrix.

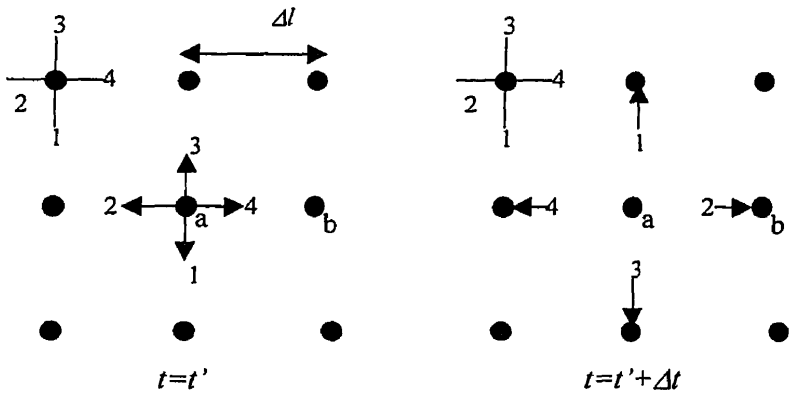

Fig. 2.2 Scattering and propagation of pulses at adjacent nodes a & b.

2.3 The TLM Method:

The transmission line model is a simple representation of electromagnetic fields propagation in a linear media. Instead of using Maxwell's equations, it represents the field behavior via transmission and reflection of pulses on transmission lines.

Consider the nodes with spatial locations as shown in Fig. 2.3. If a unit voltage impulse is incident on a node in the TLM mesh, it will be scattered in the form of a reflected impulse of -0.5v and three transmitted impulses of 0.5v. The more general case of four impulses incident on the four branches of a node is obtained by superposition. Accordingly, the scattering process of the TLM model is given by:

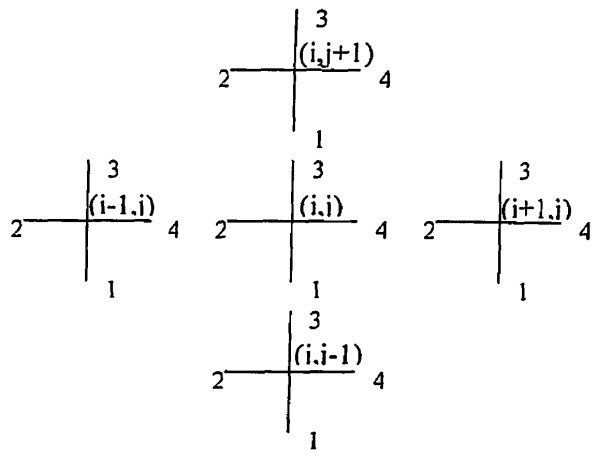

Fig. 2.3 A node and its four adjacent neighbors.

$$\begin{bmatrix} v_1^r \\ v_2^r \\ v_3^r \\ v_4^r \end{bmatrix}^t = \frac{1}{2}\begin{bmatrix} -1 & 1 & 1 & 1 \\ 1 & -1 & 1 & 1 \\ 1 & 1 & -1 & 1 \\ 1 & 1 & 1 & -1 \end{bmatrix}\begin{bmatrix} v_1^i \\ v_2^i \\ v_3^i \\ v_4^i \end{bmatrix}^t \tag{2. 3}$$

And the transfer or connection process that permits the calculation of the incident voltages at the new time step is given by:

$$\begin{aligned} v_1^{i,t+1}(i,j) &= v_3^{r,t}(i,j-1) \\ v_2^{i,t+1}(i,j) &= v_4^{r,t}(i-1,j) \\ v_3^{i,t+1}(i,j) &= v_1^{r,t}(i,j+1) \\ v_4^{i,t+1}(i,j) &= v_2^{r,t}(i+1,j) \end{aligned} \tag{2. 4}$$

The i and r superscripts denote the incident and reflected pulses, respectively. The t superscript corresponds to the time. The n (1,2,3,4) subscript refers to the port number of the node. The events described by (2.3) and (2.4) are carried out at each node in the TLM mesh. Equation (2.3) may be written in a matrix form as:

$$_k\mathbf{V}^r = \mathbf{S}_k\mathbf{V}^i \tag{2. 5}$$

where k is the number of time steps Δt that has passed since the beginning of the computation. $_k\mathbf{V}^r$ is the vector of reflected voltages and $_k\mathbf{V}^i$ is the vector of incident voltages. **S** is the scattering matrix.

Briefly, the representation of the discrete Huygens' principle by a transmission line formulation is straightforward. The transmission lines are connected at the nodes. At each node, a scattering matrix is used to obtain the reflected pulses from the incident

ones. The reflected pulses are transmitted to adjacent nodes, transforming into incident pulses. The process is repeated at each time step.

The equivalent transmission line circuit for the TM case is a shunt circuit, Fig. 2.4. Two transmission lines are connected in parallel. The total voltage across the shunt node V_y [19] is written in terms of the incident voltages on the different ports or branches as:

$$V_y = \frac{1}{2}\left(V_1^i + V_2^i + V_3^i + V_4^i\right) \tag{2.6}$$

The equivalent transmission line circuit for the TE case is a series circuit, Fig. 2.5. The transmission lines are connected in series.

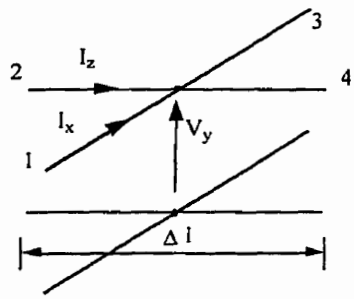

Fig. 2.4 TLM shunt node: two transmission lines are connected in parallel.

The total current I_y across the series node [19] is written in terms of the incident voltages on the different ports or branches as:

$$I_y = \frac{1}{2Z_o}\left(V_1^i - V_2^i - V_3^i + V_4^i\right) \tag{2.7}$$

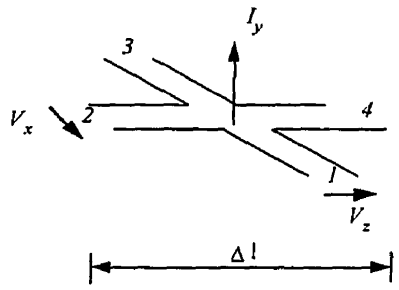

Fig. 2.5 TLM series node: two transmission lines are connected in series.

To model total and partial reflections at the boundaries, reflection coefficients are introduced in the mesh [20]. In the shunt node: electric and magnetic walls are modeled by short ($\Gamma = -1$) and open ($\Gamma = 1$) circuits, respectively. In the series case the situation is reversed. In all cases, a boundary must be placed half way between two nodes so that reflected pulses reach the boundary nodes in synchronism with other impulses in the mesh. For the appropriate truncation of the computational domain, matched or absorbing boundary conditions (ABC) have to be used, although their representation is more complex [10]. In a shunt mesh, this is usually implemented by terminating the transmission lines by the characteristic impedance of the medium.

The TLM method can model inhomogeneous media [19]-[20]. Dielectric and magnetic media are modeled by changing the impedance of the node. This can be done by adding a capacitance or an inductance to the node. Magnetic materials are modeled using inductances and dielectric media are modeled using capacitances. These capacitances and inductances are added to the node in the form of stubs. In the low frequency approximation an open-circuited stub behaves as a capacitance and a short-

circuited stub as an inductance [10]. In the two-dimensional case, these stubs are connected either to the shunt or series nodes. The open-circuited stub is connected to the shunt node, representing a medium with permittivity larger than that of vacuum. The short-circuited stub is connected to the series node, representing a medium with permeability larger than that of air.

The use of stubs in the node does not require special boundary or interface treatment. Since the transmission lines connecting the nodes (link lines) do not change, no boundary reflection or transmission coefficients are introduced. Therefore, the connection matrix of TLM is not changed by the introduction of stubs. The scattering part of TLM, however, is changed by the use of stubs [10]. The scattering matrix will have an extra term describing the reflection of a pulse in the stub. At each time step, a portion of the energy incident on the node is transmitted into the permittivity or conductivity stub in the form of a transmitted voltage pulse. At the following time step, the transmitted pulse along the permittivity stub is returned, while that along the conductivity stub is not returned because of the match termination. The scattering matrix equation of the shunt node with an open-circuited stub is [19]:

$$\begin{bmatrix} v_1 \\ v_2 \\ v_3 \\ v_4 \\ v_5 \end{bmatrix}_k^r = \frac{1}{y} \begin{bmatrix} 2-y & 2 & 2 & 2 & 2y_s \\ 2 & 2-y & 2 & 2 & 2y_s \\ 2 & 2 & 2-y & 2 & 2y_s \\ 2 & 2 & 2 & 2-y & 2y_s \\ 2 & 2 & 2 & 2 & y_s-4 \end{bmatrix}_k \begin{bmatrix} v_1 \\ v_2 \\ v_3 \\ v_4 \\ v_5 \end{bmatrix}_k^i \qquad (2.8)$$

with $y_s = 4(\varepsilon_r - 1)$ and $y = 4 + y_s$

In the series case, the matrix equation is [19]:

$$\begin{bmatrix} v_1 \\ v_2 \\ v_3 \\ v_4 \\ v_5 \end{bmatrix}^r = \frac{1}{Z} \begin{bmatrix} Z-2 & 2 & 2 & -2 & -2 \\ 2 & Z-2 & -2 & 2 & 2 \\ 2 & -2 & Z-2 & 2 & 2 \\ -2 & 2 & 2 & Z-2 & -2 \\ 2Z_s & 2Z_s & 2Z_s & -2Z_s & Z-2Z_s \end{bmatrix}_k \begin{bmatrix} v_1 \\ v_2 \\ v_3 \\ v_4 \\ v_5 \end{bmatrix}^i \qquad (2.9)$$

where $Z_s = 4(\mu - 1)$ and $Z = 4 + Z_s$

This media representation is valid only for non-dispersive isotropic dielectrics.

2.4 Three-Dimensional TLM:

The original three-dimensional TLM node was introduced by Akhtarzad and Johns in 1975 [8]. This model is constructed from two-dimensional shunt and series nodes and has been demonstrated to satisfy the Yee algorithm [7], [24]. In 1987, Johns introduced the three-dimensional symmetric condensed node (SCN) [25]. The purpose of this node was to overcome the difficulties associated with the original three-dimensional

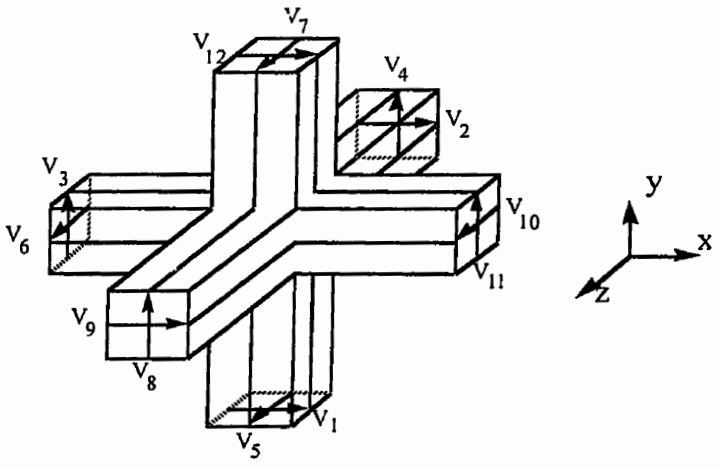

Fig. 2.6 The symmetric condensed node (SCN).

TLM node. In this model (Fig. 2.6), all six field components are condensed to the center of the node. Also, the node appears symmetric when viewed along each coordinate axis. The propagation characteristics of the node have been studied in [26]. The scattering matrix is obtained from the total voltages at the shunt node and currents at the series nodes in all three spatial directions (x,y and z) [23]. Thorough discussion of the symmetric condensed node is given in Chapter 3.

2.5 Data Extraction in TLM:

The TLM method generates large amounts of data at each time step simulation [10]. The processing of these data provides valuable insight into the behavior of the simulated structure. However, it is important to understand how to excite the TLM mesh and how to extract signals from it. The accuracy of the TLM results depends not only on the model itself, but also on the modeling of sources and on the way the field information is extracted. If the source region is not properly modeled, the results can be quite erroneous.

In the time domain TLM, the system is excited with a time domain source function at certain points of the mesh. These are called source points. The source function is time dependent. It consists of a sequence of pulses injected into the mesh as time progresses. The most frequently used distributions are the Dirac delta and the Gaussian functions. The advantage of using Gaussian functions is the bandwidth. Since these functions are band-limited (unlike the Dirac delta), higher frequency modes are not excited.

The response of a system to a source in TLM is the time domain behavior of the field at all points of the mesh. The frequency response is obtained from the time domain response with the discrete Fourier Transform (DFT). The frequency domain transformation of the time domain sequences result in the wide-band representations of the fields in the simulated regions. These results are used to characterize the simulated structure.

The output regions can also include several mesh points. In this case, the spatial distribution of the fields can be visualized. This can be done either in time or frequency domains. In the time domain visualization, a dynamic representation of the evolution of the fields through the structure can be displayed. In frequency domain, the fields can be displayed at any particular frequency. The result is an accurate representation of the field interaction at the chosen frequency.

2.6 Conclusion:

This chapter presented a review of the Transmission Line Matrix (TLM) method. The TLM method uses transmission lines to describe the behavior of electromagnetic fields propagation in a linear medium. In transmission line models, the voltage and current behave as electric and magnetic fields. The mathematical representation of the array of transmission lines is the same as that of the fields described by Maxwell's equations. The TLM method uses scattering and propagation matrices to simulate the propagation of electromagnetic fields in a medium. The space is divided into a mesh of transmission lines interconnected at discrete points in space (nodes). At each of these points, the voltages and currents are scattered and transmitted to other points of the mesh.

A three-dimensional version of the method is obtained by assembling an array of two-dimensional nodes. Series and shunt nodes are used to represent magnetic and electric field components, respectively. The complete node describes the behavior of six field components. The modeling of the medium properties is performed by stubs connected to the node. In the shunt node case, an open-circuited stub models the relative permittivity of the medium, while in the series node case, a short-circuited stub models the relative permeability.

CHAPTER 3

Modeling of Dispersive Media Using TLM

3.1 Introduction:

The TLM method has been widely used to study engineering electromagnetics in electronics problems. For example, in electrical systems the TLM has been used to study electromagnetic compatibility (EMC) [27]-[29], and can assist in the design process. This is done by establishing the degree of compatibility and interference between electronic systems and subsystems and by pointing to optimum design strategies [19]. The TLM has also been applied to the analysis and design of microwave devices including microstrip lines and resonators [30]-[33], as well as radar cross-section (RCS) problems [34]-[35]. Furthermore the TLM has been applied to the study of several radiation problems including cavity packed aperture antennas, radiation pattern and input impedance of microstrip antennas and tapered slot antennas [36]-[37]. The TLM has also been used to model dispersive dielectrics, gyromagnetic and anisotropic materials [38]-[43]. In this chapter, the TLM is used to model dispersive dielectrics that can be expressed in terms of the second order Debye approximation equation.

In the basic TLM formulation, the medium is modeled using stubs connected to the TLM node [10]. An open-circuited stub represents the dielectric material, and a short-circuited stub represents the magnetic material. In the representation of the medium parameters by stubs, the relative dielectric permittivity and permeability of the medium are frequency independent. However, this is only an approximation of the behavior of real medium [44] and valid only under certain conditions (low intensity, narrow band fields). This chapter presents the modeling of dispersive media using the symmetric condensed node (SCN) TLM. The algorithm relies on the modification of the node scattering to include the medium behavior in the TLM procedure. The modification of the node scattering is done using a nodal source approach. In this approach, sources connected to the TLM nodes represent the dielectric properties of the medium. In doing so, the TLM scattering matrix is independent of the modeled medium. Only the sources will change according to the medium properties. The nodal source approach has a physical interpretation. The sources represent the polarization and magnetization densities of the medium [44]. The medium independent scattering matrix represents the free-space propagation properties. In the absence of dielectric and magnetic media, the sources vanish. In the case of a passive medium, the sources will absorb and/or store energy. A passive network connected to the node represents this absorption and/or storage. The circuit is solved at each TLM time-step using a circuit equivalent of the node.

3.2 The Symmetric Condensed Node (SCN):

The symmetrical condensed node (SCN), shown in Fig. 3.1, is formed by combining series and shunt nodes [23]. This node can be represented by a set of equivalent shunt only and series only circuits, where a pair of transmission lines is common to both circuits as shown in Fig. 3.2. A nodal voltage V_n and loop current I_n can be determined for the shunt and series node, respectively. For the transmission line

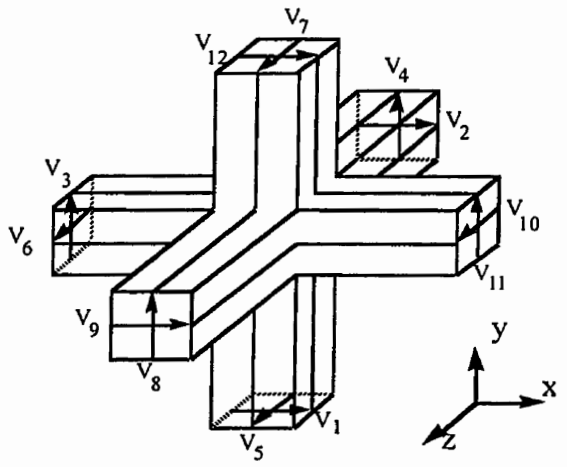

Fig. 3.1 The symmetric condensed node (SCN).

common to both representations the following equations are valid:

$$V_L^r = V_n + I_n Z_L - V_R^i \tag{3.1}$$

$$V_R^r = V_n - I_n Z_R - V_L^i \tag{3.2}$$

where the superscripts *r* and *i* are used for reflected and incident waves, respectively. The subscripts L and R denote the left and right directions, respectively.

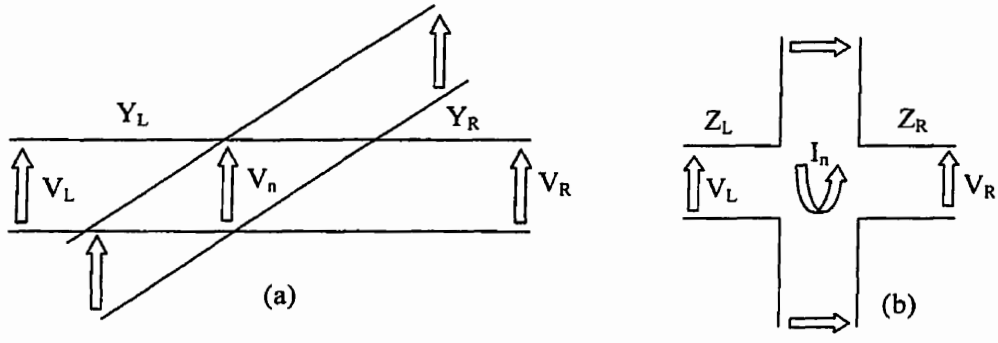

Fig. 3.2 Equivalent (a)shunt and (b)series representation of condensed node.

Applying the above procedure to all the shunt and series nodes of the symmetric condensed node (Fig. 3.3), the equations that define the SCN in terms of the voltages across shunt nodes and currents in series nodes are:

$$
\begin{aligned}
v_1^r &= v_x - Z_o i_z - v_{12}^i & v_7^r &= v_z - Z_o i_x - v_5^i \\
v_2^r &= v_x + Z_o i_y - v_9^i & v_8^r &= v_y + Z_o i_x - v_4^i \\
v_3^r &= v_y + Z_o i_z - v_{11}^i & v_9^r &= v_x - Z_o i_y - v_2^i \\
v_4^r &= v_y - Z_o i_x - v_8^i & v_{10}^r &= v_z + Z_o i_y - v_6^i \\
v_5^r &= v_z + Z_o i_x - v_7^i & v_{11}^r &= v_y - Z_o i_z - v_3^i \\
v_6^r &= v_z - Z_o i_y - v_{10}^i & v_{12}^r &= v_x + Z_o i_z - v_1^i
\end{aligned}
\qquad (3.3)
$$

where, Z_o ($= 1/Y_o$) is the characteristic impedance of the link lines of the node.

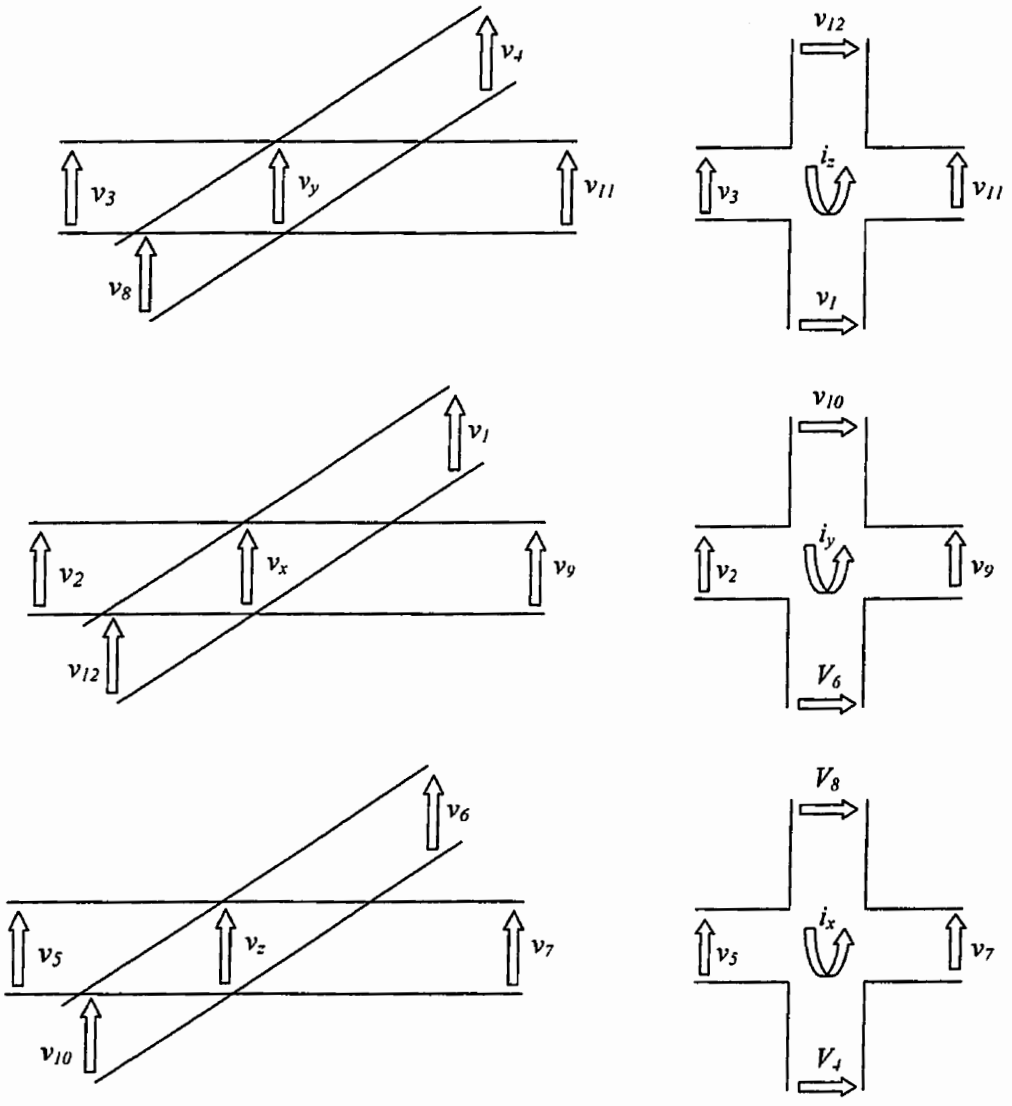

Fig. 3.3 Equivalent shunt and series representation of symmetric condensed node.

In free space the voltages across the shunt nodes v_n and the currents in the series nodes i_n (n=x,y,z) are given by:

$$
\begin{aligned}
v_x &= \frac{1}{2}(v_1^i + v_2^i + v_9^i + v_{12}^i) \\
v_y &= \frac{1}{2}(v_3^i + v_4^i + v_8^i + v_{11}^i) \\
v_z &= \frac{1}{2}(v_5^i + v_6^i + v_7^i + v_{10}^i) \\
Z_o i_x &= \frac{1}{2}(v_4^i - v_5^i + v_7^i - v_8^i) \\
Z_o i_y &= \frac{1}{2}(v_6^i - v_2^i + v_9^i - v_{10}^i) \\
Z_o i_z &= \frac{1}{2}(v_1^i - v_3^i + v_{11}^i - v_{12}^i)
\end{aligned}
\tag{3.4}
$$

Substituting the values for the voltages and currents (3.4) in equation (3.3), we end with the relationship between the reflected voltages in the different branches and the incident voltages:

$$
\begin{aligned}
v_1^r &= 0.5\left[v_2^i + v_3^i + v_9^i - v_{11}^i\right] & v_7^r &= 0.5\left[v_6^i + v_8^i + v_{10}^i - v_4^i\right] \\
v_2^r &= 0.5\left[v_1^i + v_6^i + v_{12}^i - v_{10}^i\right] & v_8^r &= 0.5\left[v_3^i + v_7^i + v_{11}^i - v_5^i\right] \\
v_3^r &= 0.5\left[v_1^i + v_4^i + v_8^i - v_{12}^i\right] & v_9^r &= 0.5\left[v_1^i + v_{10}^i + v_{12}^i - v_6^i\right] \\
v_4^r &= 0.5\left[v_3^i + v_5^i + v_{11}^i - v_7^i\right] & v_{10}^r &= 0.5\left[v_5^i + v_7^i + v_9^i - v_2^i\right] \\
v_5^r &= 0.5\left[v_4^i + v_6^i + v_{10}^i - v_8^i\right] & v_{11}^r &= 0.5\left[v_4^i + v_8^i + v_{12}^i - v_1^i\right] \\
v_6^r &= 0.5\left[v_2^i + v_5^i + v_7^i - v_9^i\right] & v_{12}^r &= 0.5\left[v_2^i + v_9^i + v_{11}^i - v_3^i\right]
\end{aligned}
\tag{3.5}
$$

In a matrix form, the previous equation defines the scattering procedure in free space. The scattering matrix that relates the reflected and incident voltages is the same as that obtained by Johns [25].

Lumped element networks or sources are used to model the medium. These networks are connected to the node by a transmission line of characteristic impedance equal to the driving point impedance of the node ($Y = 4Y_o$ or $Z = 4Z_o$) [43]. The incident and reflected voltages from these networks are related to the voltages across the shunt nodes and the currents in the series nodes:

$$\begin{aligned} v_x &= v_{ex}^r + v_{ex}^i \qquad 4Z_o i_x = (v_{mx}^r - v_{mx}^i) \\ v_y &= v_{ey}^r + v_{ey}^i \qquad 4Z_o i_y = (v_{my}^r - v_{my}^i) \\ v_z &= v_{ez}^r + v_{ez}^i \qquad 4Z_o i_z = (v_{mz}^r - v_{mz}^i) \end{aligned} \tag{3.6}$$

v_{en}^i, v_{en}^r, v_{mn}^i and v_{mn}^r (n=x,y,z) are the incident and reflected voltages from the lumped element networks (sources) connected to the shunt and series nodes respectively. The voltages across the shunt nodes v_n and the currents in the series nodes i_n (n=x,y,z) are modified in the presence of the nodal sources and given by:

$$\begin{aligned} v_x &= \frac{1}{4}(v_1^i + v_2^i + v_9^i + v_{12}^i) + v_{ex}^i \qquad Z_o i_x = \frac{1}{4}(v_4^i - v_5^i + v_7^i - v_8^i - v_{mx}^i) \\ v_y &= \frac{1}{4}(v_3^i + v_4^i + v_8^i + v_{11}^i) + v_{ey}^i \qquad Z_o i_y = \frac{1}{4}(v_6^i - v_2^i + v_9^i - v_{10}^i - v_{my}^i) \\ v_z &= \frac{1}{4}(v_5^i + v_6^i + v_7^i + v_{10}^i) + v_{ez}^i \qquad Z_o i_z = \frac{1}{4}(v_1^i - v_3^i + v_{11}^i - v_{12}^i - v_{mz}^i) \end{aligned} \tag{3.7}$$

This is the same as equation (3.4) but in this case the voltages incident from the nodal sources are included. Substituting these values of voltages and currents in equation

(3.3), we obtain the relationship between the reflected voltages in the different branches and the incident voltages from the branches and nodal sources:

$$
\begin{aligned}
v_1^r &= \frac{1}{4}\left[v_2^i + v_3^i + v_9^i - v_{11}^i - 2v_{12}^i\right] + v_{ex}^i + \frac{1}{4}v_{mz}^i \\
v_2^r &= \frac{1}{4}\left[v_1^i + v_6^i + v_{12}^i - v_{10}^i - 2v_9^i\right] + v_{ex}^i - \frac{1}{4}v_{my}^i \\
v_3^r &= \frac{1}{4}\left[v_1^i + v_4^i + v_8^i - v_{12}^i - 2v_{11}^i\right] + v_{ey}^i - \frac{1}{4}v_{mz}^i \\
v_4^r &= \frac{1}{4}\left[v_3^i + v_5^i + v_{11}^i - v_7^i - 2v_8^i\right] + v_{ey}^i + \frac{1}{4}v_{mx}^i \\
v_5^r &= \frac{1}{4}\left[v_4^i + v_6^i + v_{10}^i - v_8^i - 2v_7^i\right] + v_{ey}^i - \frac{1}{4}v_{mx}^i \\
v_6^r &= \frac{1}{4}\left[v_2^i + v_5^i + v_7^i - v_9^i - 2v_{10}^i\right] + v_{ez}^i + \frac{1}{4}v_{my}^i \\
v_7^r &= \frac{1}{4}\left[v_6^i + v_8^i + v_{10}^i - v_4^i - 2v_5^i\right] + v_{ez}^i + \frac{1}{4}v_{mx}^i \\
v_8^r &= \frac{1}{4}\left[v_3^i + v_7^i + v_{11}^i - v_5^i - 2v_4^i\right] + v_{ey}^i - \frac{1}{4}v_{mx}^i \\
v_9^r &= \frac{1}{4}\left[v_1^i + v_{10}^i + v_{12}^i - v_6^i - 2v_2^i\right] + v_{ex}^i + \frac{1}{4}v_{my}^i \\
v_{10}^r &= \frac{1}{4}\left[v_5^i + v_7^i + v_9^i - v_2^i - 2v_6^i\right] + v_{ez}^i - \frac{1}{4}v_{my}^i \\
v_{11}^r &= \frac{1}{4}\left[v_4^i + v_8^i + v_{12}^i - v_1^i - 2v_3^i\right] + v_{ey}^i + \frac{1}{4}v_{mz}^i \\
v_{12}^r &= \frac{1}{4}\left[v_2^i + v_9^i + v_{11}^i - v_3^i - 2v_1^i\right] + v_{ex}^i - \frac{1}{4}v_{mz}^i
\end{aligned}
\qquad (3.8)
$$

To obtain the reflected voltages at the sources we use equations (3.6) and (3.7), in which case we obtain:

$$
\begin{aligned}
v_{ex}^r &= \frac{1}{4}(v_1^i + v_2^i + v_9^i + v_{12}^i) \qquad v_{mx}^r = (v_4^i - v_5^i + v_7^i - v_8^i) \\
v_{ey}^r &= \frac{1}{4}(v_3^i + v_4^i + v_8^i + v_{11}^i) \qquad v_{my}^r = (v_6^i - v_2^i + v_9^i - v_{10}^i) \\
v_{ez}^r &= \frac{1}{4}(v_5^i + v_6^i + v_7^i + v_{10}^i) \qquad v_{mz}^r = (v_1^i - v_3^i + v_{11}^i - v_{12}^i)
\end{aligned}
\qquad (3.9)
$$

The last two equations can be written in a matrix form as:

$$[\mathbf{v}^r] = [\mathbf{S}][\mathbf{v}^i] + [\mathbf{T}][\mathbf{v}_s^i]$$
$$[\mathbf{v}_s^r] = [\mathbf{T}]^t[\mathbf{v}^i] \tag{3.10}$$

In this equation t denotes the transpose and the vectors $\mathbf{v}_s^i$ and $\mathbf{v}_s^r$ are given by:

$$[\mathbf{v}_s^i]^t = \begin{bmatrix} 4v_{ex}^i & 4v_{ey}^i & 4v_{ez}^i & v_{mx}^i & v_{my}^i & v_{mz}^i \end{bmatrix}$$
$$[\mathbf{v}_s^r]^t = \begin{bmatrix} v_{ex}^r & v_{ex}^r & v_{ex}^r & 4v_{mx}^r & 4v_{my}^r & 4v_{mz}^r \end{bmatrix} \tag{3.11}$$

The scattering matrix **S** is given by:

$$[\mathbf{S}] = \frac{1}{4}\begin{bmatrix} 0 & 1 & 1 & 0 & 0 & 0 & 0 & 0 & 1 & 0 & -1 & -2 \\ 1 & 0 & 0 & 0 & 0 & 1 & 0 & 0 & -2 & -1 & 0 & 1 \\ 1 & 0 & 0 & 1 & 0 & 0 & 0 & 1 & 0 & 0 & -2 & -1 \\ 0 & 0 & 1 & 0 & 1 & 0 & -1 & -2 & 0 & 0 & 1 & 0 \\ 0 & 0 & 0 & 1 & 0 & 1 & -2 & -1 & 0 & 1 & 0 & 0 \\ 0 & 1 & 0 & 0 & 1 & 0 & 1 & 0 & -1 & -2 & 0 & 0 \\ 0 & 0 & 0 & -1 & -2 & 1 & 0 & 1 & 0 & 1 & 0 & 0 \\ 0 & 0 & 1 & -2 & -1 & 0 & 1 & 0 & 0 & 0 & 1 & 0 \\ 1 & -2 & 0 & 0 & 0 & -1 & 0 & 0 & 0 & 1 & 0 & 1 \\ 0 & -1 & 0 & 0 & 1 & -2 & 1 & 0 & 1 & 0 & 0 & 0 \\ -1 & 0 & -2 & 1 & 0 & 0 & 0 & 1 & 0 & 0 & 0 & 1 \\ -2 & 1 & -1 & 0 & 0 & 0 & 0 & 0 & 1 & 0 & 1 & 0 \end{bmatrix} \tag{3.12}$$

The matrix T is given by:

$$[\mathbf{T}] = \frac{1}{4}\begin{bmatrix} 1 & 0 & 0 & 0 & 0 & 1 \\ 1 & 0 & 0 & 0 & -1 & 0 \\ 0 & 1 & 0 & 0 & 0 & -1 \\ 0 & 1 & 0 & 1 & 0 & 0 \\ 0 & 0 & 1 & -1 & 0 & 0 \\ 0 & 0 & 1 & 0 & 1 & 0 \\ 0 & 0 & 1 & 1 & 0 & 0 \\ 0 & 1 & 0 & -1 & 0 & 0 \\ 1 & 0 & 0 & 0 & 1 & 0 \\ 0 & 0 & 1 & 0 & -1 & 0 \\ 0 & 1 & 0 & 0 & 0 & 1 \\ 1 & 0 & 0 & 0 & 0 & -1 \end{bmatrix} \qquad (3.13)$$

Knowing the incident voltages from sources (as will be shown in this chapter) and different branches, we can obtain the reflected voltages and hence the incident voltages at the next time-step.

3.3 Electrical Properties of Biological Tissue:

Dispersive materials are those materials whose electrical properties are frequency dependent. These electrical properties are namely the dielectric permittivity relative to free space ε_r and conductivity σ. For biological tissue, both properties change strongly with frequency. As a matter of fact, as the frequency increases from a few hertz to gigahertz, the dielectric constant ε_r decreases from several million to only a few units. This manifests the inability of the charges in the tissue to respond to the higher frequencies of the applied fields, thus resulting in lower permittivity values.

Concurrently, for the same increase in frequency, the conductivity σ increases from a few millimhos per centimeter to nearly a thousand [47]. Fig. 3.4 shows the variation of the dielectric properties of muscle with frequency.

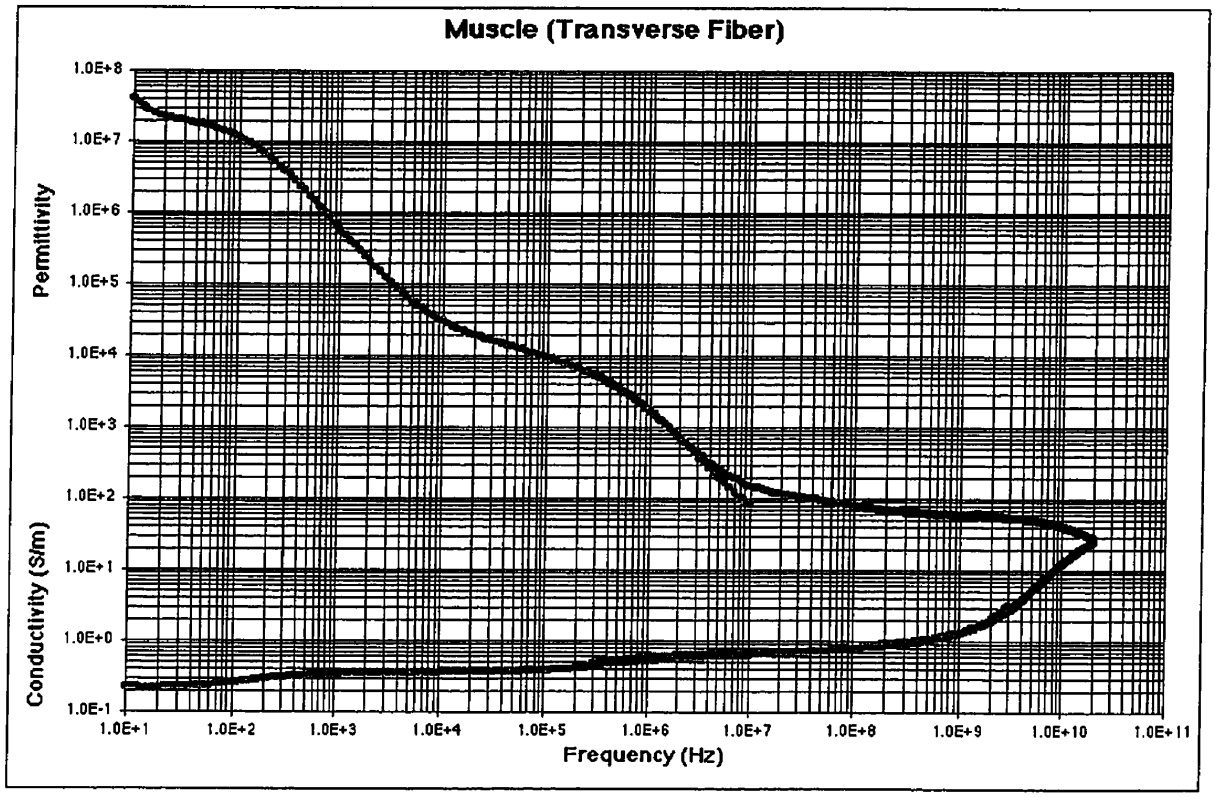

Fig. 3.4 Variation of the dielectric properties of muscle with the frequency [47].

The conductivity σ and the dielectric permittivity ε_r of a medium can be combined together to form the complex permittivity constant which is a frequency dependent quantity and defined as:

$$\varepsilon^* = \varepsilon_r - j\frac{\sigma}{\omega\varepsilon_o} \quad \text{or} \quad \varepsilon^* = \varepsilon' - j\varepsilon'' \tag{3.14}$$

ε^* can be expressed in terms of rational functions. The most popular rational functions that have been used are first order Debye approximation equation, the second order Debye approximation equation and Lorentz equation.

3.3.1 First order Debye Approximation Equation:

The complex dielectric permittivity constant of biological tissue can be expressed as a first order Debye equation:

$$\varepsilon^*(\omega) = \varepsilon_\infty + \frac{\varepsilon_s - \varepsilon_\infty}{1 + j\omega\tau} \qquad (3.15)$$

where ε_∞ is the permittivity at infinite frequency, ε_s is the zero or static permittivity and τ is the relaxation time constant.

3.3.2 Second Order Debye Approximation Equation:

The complex dielectric permittivity constant of biological tissue can be expressed as a second order Debye equation:

$$\varepsilon^*(\omega) = \varepsilon_\infty + \frac{\varepsilon_{s1} - \varepsilon_\infty}{1 + j\omega\tau_1} + \frac{\varepsilon_{s2} - \varepsilon_\infty}{1 + j\omega\tau_2} \qquad (3.16)$$

where ε_∞ is the permittivity at infinite frequency, $\varepsilon_s = \varepsilon_{s1} + \varepsilon_{s2} - \varepsilon_\infty$ is the zero or static permittivity and τ_1 and τ_2 are the relaxation time constants.

3.3.3 Lorentz Equation:

The complex dielectric permittivity constant can be expressed in terms of the Lorentz equation:

$$\varepsilon^*(\omega) = \varepsilon_\infty + (\varepsilon_s - \varepsilon_\infty)\frac{\omega_o^2}{\omega_o^2 + 2j\omega\delta - \omega^2} \qquad (3.17)$$

where ε_∞ is the permittivity at infinite frequency, ε_s is the zero or static permittivity , ω_o is the resonant angular frequency and δ is the damping constant.

3.4 Modeling of Dispersive Media in FDTD:

Modeling of dispersive materials has been widely studied using finite differece time domain (FDTD). Two main approaches have been taken to develop frequency dependent finite difference time domain $(FD)^2TD$ method. The first one utilizes the use of recursive convolution (RC) to develop frequency dispersive RC FDTD method. The second approach utilizes the use of auxiliary differential equation (ADE).

In 1990, Luebbers *et al* published the first frequency dependent FDTD formulation [48] by using a recursive convolution (RC) scheme to model dispersive media. In this formulation, the complex permittivity is converted from the frequency domain to the time domain. It is then convolved with the time domain electric fields to obtain time domain fields for dispersive materials. This discrete time domain convolution has to be updated recursively for some rational forms of the complex permittivity. Independently, in 1991 Bui *et al* [49] also developed a RC FDTD model for modeling

dispersive media. In both cases, the medium was modeled using a first order Debye approximation equation and was tested with one and two-dimensional problems. Luebbers *et al* [50] modified and generalized the frequency dependent RC formulation to handle wave propagation in any dispersive media as long as the frequency domain permittivity can be expressed as a ratio of two polynomials [51]. The main disadvantage is that the calculation time is approximately twice that of nondispersive lossy dielectric FDTD calculation. Much work have been done by other research groups to improve the RC approach with regards to its accuracy and efficiency. Applications of the FDTD RC method include Sullivan's modeling of 3-D biological problems [52].

While Luebbers and others were developing the frequency dispersive RC FDTD method, several other researchers were developing an alternate frequency dispersive method termed the auxiliary differential equation (ADE) method. The first papers utilizing this approach were by Kashiwa *et al* [53]-[55] for Debye media, Lorentz media, and media obeying the Cole-Cole Circular Arc law, respectively. While this research was progressing, Joseph *et al* [56] independently developed a similar ADE model for Debye media. Goorjian and Taflove [57] soon extended this model to include effects for nonlinear dispersive media. Independently, a third research group headed by Gandhi proposed the ADE method for treating general dispersive media [58]-[60]. In this method, a differential equation relating the flux density and the electric field together with the complex permittivity has to be formulated. This equation is then solved simultaneously with the standard FDTD equations. This method has been tested with one and three-dimensional problems. First and second order Debye approximation have been used to model the complex dielectric permittivity of biological tissue. Originally, the

disadvantage of the ADE approach was that it required a large amount of storage. However, further research has shown how to reduce this storage requirement.

3.5 Modeling of Second Order Debye Dielectrics in TLM:

Using a pulse excitation in the TLM generates results for a wide band of frequencies from a single computer run via Fourier transformation. Yet, the requirement that the material properties have to be kept constant limit the accuracy of the results obtained via a single run. This is only the case for frequency dependent or dispersive materials. To overcome this problem in the basic TLM method, several computer runs have to be carried out for narrow frequency bands. Dispersive materials whose frequency dependence can be expressed in terms of first order Debye equation have been successfully modeled in the TLM [38], [40]. In this section, we show how to model a dispersive material that can be expressed as a second order Debye equation in the TLM method [61].

The conductivity σ and the dielectric permittivity ε_r of a medium can be combined together to form the complex permittivity which is a frequency dependent quantity as shown by equation (3.14). For a dispersive dielectric medium the frequency domain permittivity $\varepsilon^*(\omega)$ can be modeled using second order Debye equation:

$$\varepsilon^*(\omega) = \varepsilon_\infty + \frac{\varepsilon_{s1} - \varepsilon_\infty}{1 + j\omega\tau_1} + \frac{\varepsilon_{s2} - \varepsilon_\infty}{1 + j\omega\tau_2} \qquad (3.18)$$

where ε_∞ is the permittivity at infinite frequency, $\varepsilon_s = \varepsilon_{s1} + \varepsilon_{s2} - \varepsilon_\infty$ is the zero or static permittivity and τ_1 and τ_2 are the relaxation time constants.

Equation (3.18) could be separated into its real and imaginary parts, giving the following equations for the dielectric permittivity and conductivity:

$$\varepsilon' = \varepsilon_\infty + \frac{\varepsilon_{s1} - \varepsilon_\infty}{1+(\omega\tau_1)^2} + \frac{\varepsilon_{s2} - \varepsilon_\infty}{1+(\omega\tau_2)^2} \tag{3.19}$$

$$\varepsilon'' = (\omega\tau_1)\frac{\varepsilon_{s1} - \varepsilon_\infty}{1+(\omega\tau_1)^2} + (\omega\tau_2)\frac{\varepsilon_{s2} - \varepsilon_\infty}{1+(\omega\tau_2)^2} \tag{3.20}$$

The second order Debye equation (3.18) can be modeled by the *RC* circuit shown in Fig. 3.5. The capacitances and resistances of the circuit model are defined in terms of the second order Debye equation parameters as:

$$R_1 = \tau_1\tau_2 / 2\Delta t(\varepsilon_{s1}\tau_2 + \varepsilon_{s2}\tau_1 - \varepsilon_\infty(\tau_1 + \tau_2))$$

$$R_2 = \tau_1\tau_2 / C_2C_3R_1$$

$$C_1 = 2\Delta t(\varepsilon_\infty - 1) \tag{3.21}$$

$$C_2 = \frac{2\Delta t(\varepsilon_{s1}\tau_2 + \varepsilon_{s2}\tau_1 - \varepsilon_\infty(\tau_1 + \tau_2))^2}{(\varepsilon_{s1}\tau_2 + \varepsilon_{s2}\tau_1 - \varepsilon_\infty(\tau_1 + \tau_2))(\tau_1 + \tau_2) - \tau_1\tau_2(\varepsilon_s - \varepsilon_\infty)}$$

$$C_3 = 2\Delta t(\varepsilon_s - \varepsilon_\infty) - C_2$$

Details of the derivation is given in Appendix (A).

Circuit theory may then be used to solve the above circuit to obtain the state equations [45] that describe it. At node 1 the current *i* incident from the node is:

$$i = C_1\frac{dv}{dt} + \frac{v - v_1}{R_1} \tag{3.22}$$

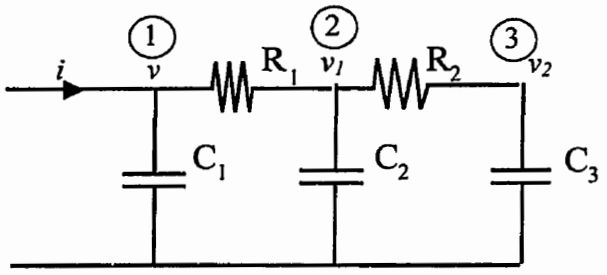

Fig. 3.5. Circuit model for second order Debye dielectric.

From the transmission line theory this current is given by:

$$i = Y(v^r - v^i) = Y(v^r - (v - v^r)) = Y(2v^r - v) \tag{3.23}$$

where Y is the admittance of the link line connecting the circuit to the node and is specified to be $4Y_o$ as mentioned before. v^r is the reflected voltage from the node to the source and v^i is the incident voltage from the source. At nodes 2 and 3, the following relations exist:

$$\frac{v - v_1}{R_1} = C_2 \frac{dv_1}{dt} + \frac{v_1 - v_2}{R_2} \tag{3.24}$$

$$\frac{v_1 - v_2}{R_2} = C_3 \frac{dv_2}{dt} \tag{3.25}$$

Rewriting the above equations and combining (3.22) and (3.23):

$$\frac{dv}{dt} = \left[\frac{-Y}{C_1} - \frac{1}{R_1 C_1}\right] v + \frac{1}{R_1 C_1} v_1 + \frac{2Y}{C_1} v^r$$

$$\frac{dv_1}{dt} = \frac{1}{R_1 C_2} v - \left[\frac{1}{R_1 C_2} + \frac{1}{R_2 C_2}\right] v_1 + \frac{1}{R_2 C_2} v_2 \qquad (3.26)$$

$$\frac{dv_2}{dt} = \frac{1}{R_2 C_3} v_1 - \frac{1}{R_2 C_3} v_2$$

The above equations can be written in a matrix form as:

$$\frac{\mathbf{d}}{\mathbf{dt}}[\mathbf{v}_n] = [\mathbf{A}][\mathbf{v}_n] + [\mathbf{B}][\mathbf{v}^r_{en}]$$

$$[\mathbf{v}^i_{en}] = [\mathbf{C}][\mathbf{v}_n] + [\mathbf{D}][\mathbf{v}^r_{en}] \qquad (3.27)$$

where:

$$[\mathbf{A}] = \begin{bmatrix} -\left(\frac{Y}{C_1} + \frac{1}{R_1 C_1}\right) & \frac{1}{R_1 C_1} & 0 \\ \frac{1}{R_1 C_2} & -\left(\frac{1}{R_1 C_2} + \frac{1}{R_2 C_2}\right) & \frac{1}{R_2 C_2} \\ 0 & \frac{1}{R_2 C_3} & -\frac{1}{R_2 C_3} \end{bmatrix} \quad [\mathbf{B}] = \begin{bmatrix} 2\frac{Y}{C_1} \\ 0 \\ 0 \end{bmatrix} \qquad (3.28)$$

$$[\mathbf{C}] = \begin{bmatrix} 1 & 0 & 0 \end{bmatrix} \quad [\mathbf{D}] = [-1]$$

where n=x,y and z, $\mathbf{v}^r_{en}$ are the reflected voltages from the node to the sources, $\mathbf{v}^i_{en}$ are the incident voltages from the sources and $\mathbf{v}_n$ is a vector formed of the node voltage and the two auxiliary voltages.

Equation (3.27) is discretized using the approximate trapezoidal scheme for numerical integration [46], in which:

$$\int_{x_i}^{x_{i+1}} f(x)dx = \frac{f(x_i)+f(x_{i+1})}{2}(\Delta x) \tag{3.29}$$

Equation (3.27) is then solved at each time step to obtain the incident voltages from the sources and hence, the reflected voltages at the different ports of the node.

$$[\mathbf{v}_n(t+\Delta t)] = \left([\mathbf{I}]-\frac{\Delta t}{2}[\mathbf{A}]\right)^{-1}\left([\mathbf{I}]+\frac{\Delta t}{2}[\mathbf{A}]\right)[\mathbf{v}_n(t)]+ \left([\mathbf{I}]-\frac{\Delta t}{2}[\mathbf{A}]\right)^{-1}\frac{\Delta t}{2}[\mathbf{B}]\left([\mathbf{v}^r_{en}(t+\Delta t)]+[\mathbf{v}^r_{en}(t)]\right) \tag{3.30}$$

$$[\mathbf{v}^i_{en}(t+\Delta t)] = [\mathbf{C}][\mathbf{v}_n(t+\Delta t)]+[\mathbf{D}][\mathbf{v}^r_{en}(t+\Delta t)]$$

Three sets of matrix equations in the form of (3.30) have to be solved to obtain $\mathbf{v_x}$, $\mathbf{v_y}$ and $\mathbf{v_z}$ and hence $\mathbf{v}^i_{ex}$, $\mathbf{v}^i_{ey}$ and $\mathbf{v}^i_{ez}$ that are used in the scattering procedure. A schematic diagram outlining the steps followed in the implementation of the TLM algorithm taking into consideration the dispersive nature of the medium is shown in Fig. 3.6.

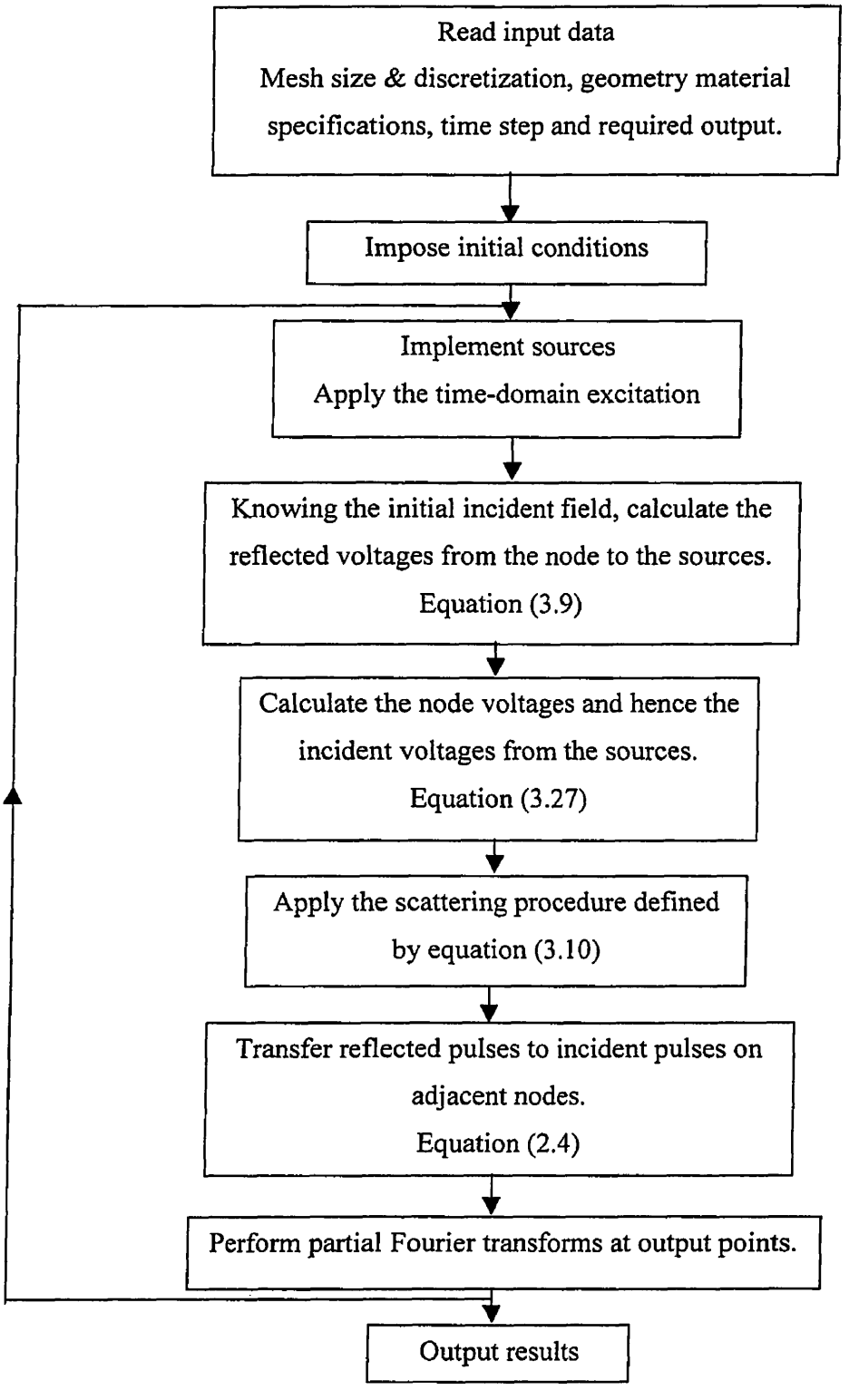

Fig. 3.6 Schematic of the dispersive TLM algorithm.

3.6 Numerical Simulations and Results:

Electromagnetic scattering and absorption by human tissue are being widely studied. Numerical techniques such as the *Finite Difference Time Domain* (FDTD) method and the transmission line matrix (TLM) method have been found to be highly versatile in calculating the specific absorption rate (SAR) distribution resulting from exposure to electromagnetic waves. A weakness in the conventional form of these techniques is that the dispersion of the tissues' dielectric properties is ignored and frequency independent properties are assumed.

In this section, the application of the symmetric condensed node transmission line matrix method (SCN TLM) to three-dimensional scattering from biological tissue is investigated. A second order Debye equation of the complex permittivity in the frequency domain is used in a modified TLM technique to simulate the dispersive nature of biological tissue. Some of the results of the numerical simulations are compared to those obtained analytically using Mie series [59], [62] or to those obtained using the stub-loaded or nondispersive TLM method.

All simulations are carried out for an incident plane wave with a Gaussian pulse excitation. To ensure the stability of the solution in all simulations, the time step Δt is given by $\ell/2v$, where ℓ is the cell size and v is the maximum velocity of the electromagnetic wave encountered anywhere in the modeled space, which includes the dielectric body and the surroundings. This is same as the constraint set by Taflove for stability in the FDTD. For our simulations $v = c$, which is the velocity of the electro-magnetic waves in air. The stability of the modified TLM is discussed in [63].

The accuracy of the scattering procedure of the modified TLM technique is first established by comparing the near field data obtained for simulating the test case of a 2/3 muscle-equivalent sphere with the analytical Mie series solution. The second order Debye equation for the 2/3 muscle-equivalent in the frequency range $20MHz$ to $20GHz$ is [59]:

$$\varepsilon^*(\omega) = 19 + \frac{10000}{1 + j\omega(0.113 \times 10^{-6})} + \frac{42}{1 + j\omega(0.119 \times 10^{-10})} \tag{3.31}$$

The diameter of the sphere is $20cm$ corresponding to the average dimensions of the human head. The sphere is divided into cells of size $1cm$. Six cells are taken from the boundaries of the sphere to the absorbing boundaries in the x-, y-, and z-directions. The time step δt is taken to be 1/60 ns. The Gaussian pulse is of the form $1000e^{-(t-t_o)^2/T^2}$ where $t_o = 210\delta t$ and $T = 80\delta t$. The incident pulse is polarized in the z-direction and propagating in the y-direction. Fig. 3.7 shows the results obtained using the analytical Mie series solution and the dispersive TLM at $100MHz$ for the total field E_z along the y-axis through

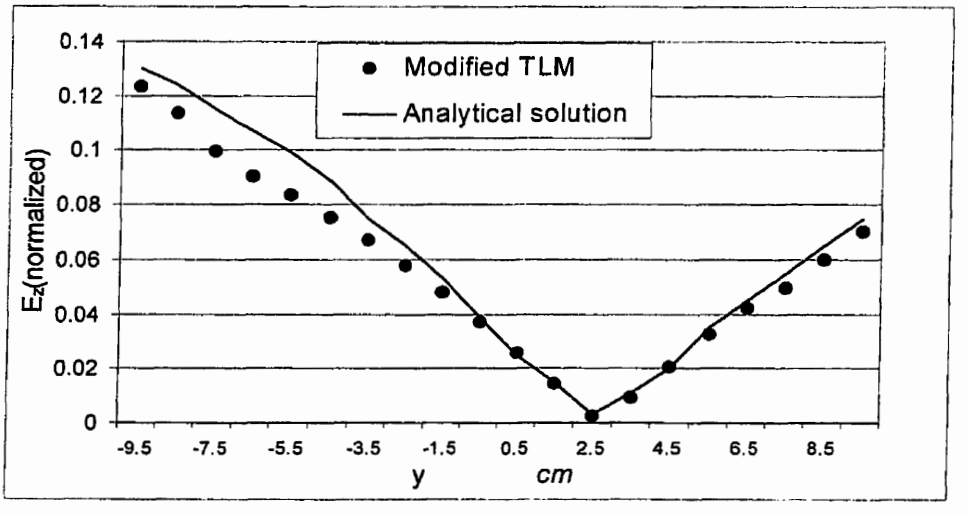

Fig. 3.7. E_z calculated by the *modified TLM* and the Mie series analytical solution at 100 *MHz*.

the center of the sphere. The computed result is normalised to the value of the incident field at $100MHz$. As shown the results are in a reasonable good agreement.

To further investigate the accuracy of the technique in handling high contrast dielectric bodies, the near field distribution in a layered dielectric sphere is obtained using the analytical Mie series [62] and the dispersive TLM methods. The sphere has two layers with radii a_1 = 7.5cm and a_2 = 15cm and permittivities $\varepsilon_1 = 72 - j\frac{0.9}{\omega\varepsilon_o}$ and $\varepsilon_2 = 7.5 - j\frac{0.5}{\omega\varepsilon_o}$. The equivalent second order Debye approximations that are used by the dispersive TLM are:

$$\varepsilon_1^*(\omega) = 50.8 + \frac{11417.67}{1 + j\omega(0.113\times10^{-6})} + \frac{18.9343}{1 + j\omega(0.119\times10^{-10})}$$
$$\varepsilon_2^*(\omega) = 5.8 + \frac{637.3}{1 + j\omega(0.113\times10^{-6})} + \frac{1.57356}{1 + j\omega(0.119\times10^{-10})} \qquad (3.31)$$

The plane wave is propagating in the z-direction and polarized in the x-direction. The space is 54x54x54, the cell size is .9375cm, δt=0.156358ps and the Gaussian pulse has t_o=210δt and T=80δt. 11 cells were taken to the absorbing boundary in each direction. Fig. 3.8 shows the results obtained using the analytical Mie series solution and the dispersive TLM at $100MHz$ for E_x along the z-axis through the center of the sphere. As shown the numerical result agrees well with the analytical result. For the last two simulations, the Mie series solutions were obtained from [59] and [62], respectively.

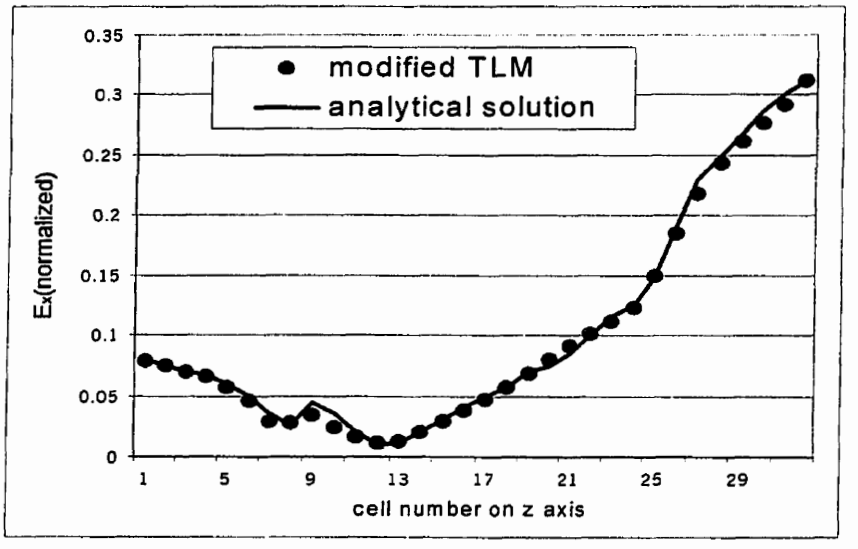

Fig. 3.8 E_x calculated by the *modified TLM* and the Mie series analytical solution at 100 *MHz* along the z-axis of a two layered sphere.

The next simulation involved the use of a $10\times10\times10\,cm$ cube filled with bone (weak scatter). The TLM mesh is formed of $50\times50\times50$ nodes. Thus, $\Delta t = 8.339\,ps$ for $\delta = 5\,mm$. The Gaussian pulse is of the form $1000e^{-(t-t_o)^2/T^2}$ where $t_o = 90\delta t$ and $T = 60\delta t$. The plane wave is propagating in the z-direction and polarized in the x-direction. The time domain near field data are obtained. Fast Fourier transformation [37] is then used to generate the frequency domain near field data and hence the specific absorption rate (SAR). SAR is a measure of the amount of energy absorbed by the tissue following irradiation by electromagnetic waves. This value is directly related to the various components of the field inside the body:

$$SAR = 0.5(\frac{\sigma}{\rho})|E|^2 \tag{3.32}$$

The density ρ is assumed constant and equals to that of water although this is an approximate value especially for bone. Assuming a nondispersive nature of the tissue, the equivalent dielectric permittivity and the loss tangent of the tissue are obtained at $100MHz$ as the real and imaginary parts of the second order Debye equation, respectively. These values are further used to obtain the SAR distribution using the stub-loaded or the nondispersive TLM method at various frequencies. As shown in Fig. 3.9, the results obtained from the modified TLM and the stub-loaded TLM techniques agree very well at $100MHz$ but they are different at $300MHz$ and $500MHz$. The difference in the distributions obtained from both techniques is due mainly to neglecting the effect of the dispersive nature of the tissue in the stub-loaded TLM. Also, the difference in the SAR distributions at $500MHz$ is larger than at $300MHz$, this is because as the frequency increases, the difference between the values used and the actual values of the dielectric permittivity and loss tangent increases.

In the following simulation the bone is replaced with brain and nerve tissue (strong scatter). The cell size δ and time step Δt are the same as before and satisfying the condition that $\delta \leq \frac{\lambda_{eff}}{10}$. The specifications of the incident pulse were not changed. Fig. 3.10 compares the results at $100MHz$, $300MHz$ and $500MHz$. The two simulated results are almost identical at $300MHz$, the frequency at which the equivalent values for permittivity and loss tangent of the tissue are used by the nondispersive TLM.

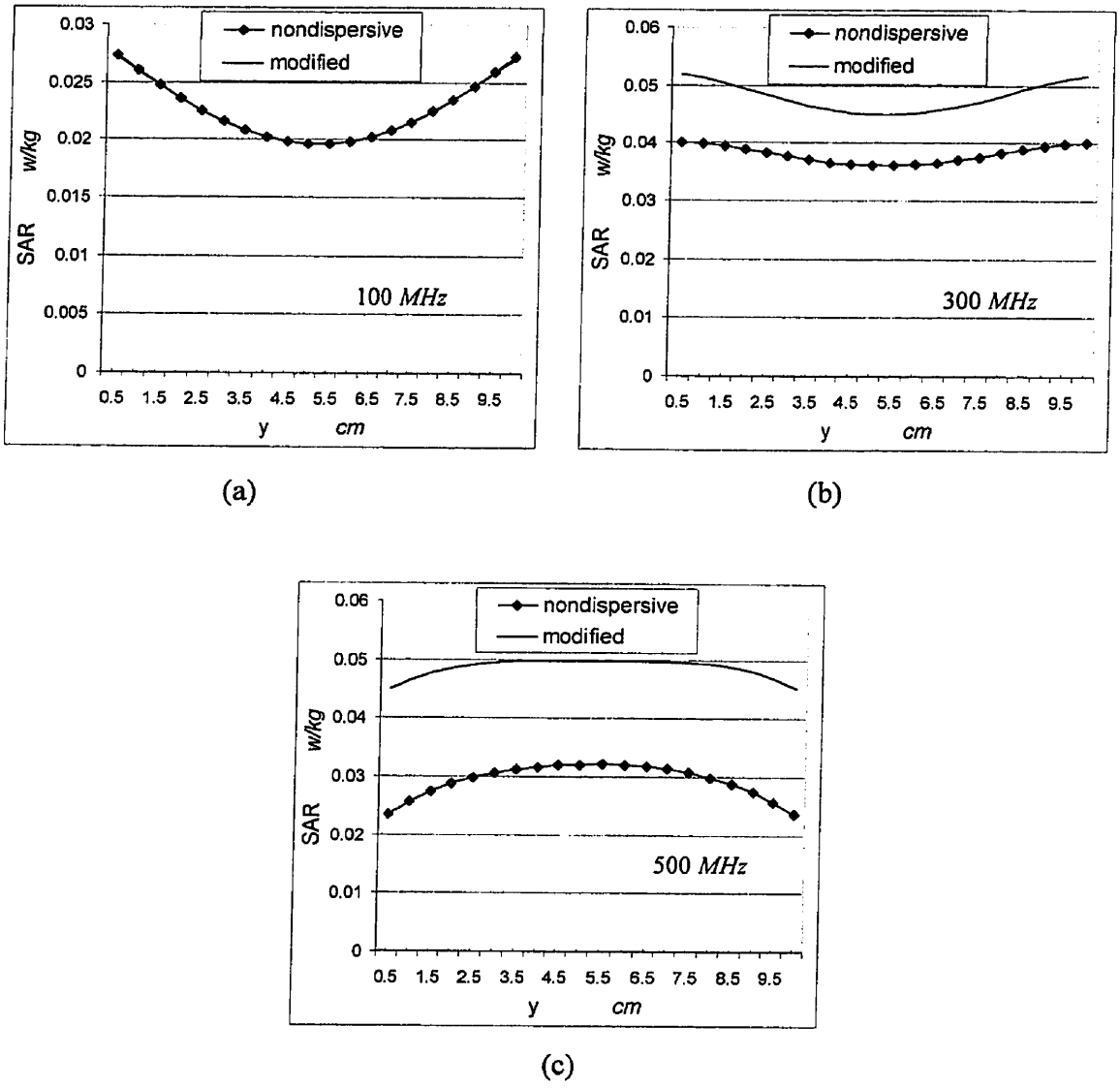

Fig. 3.9 SAR obtained from modified *TLM* and nondispersive *TLM* in the center of the cube along the *y*-axis for the case of a weak scatterer (bone).

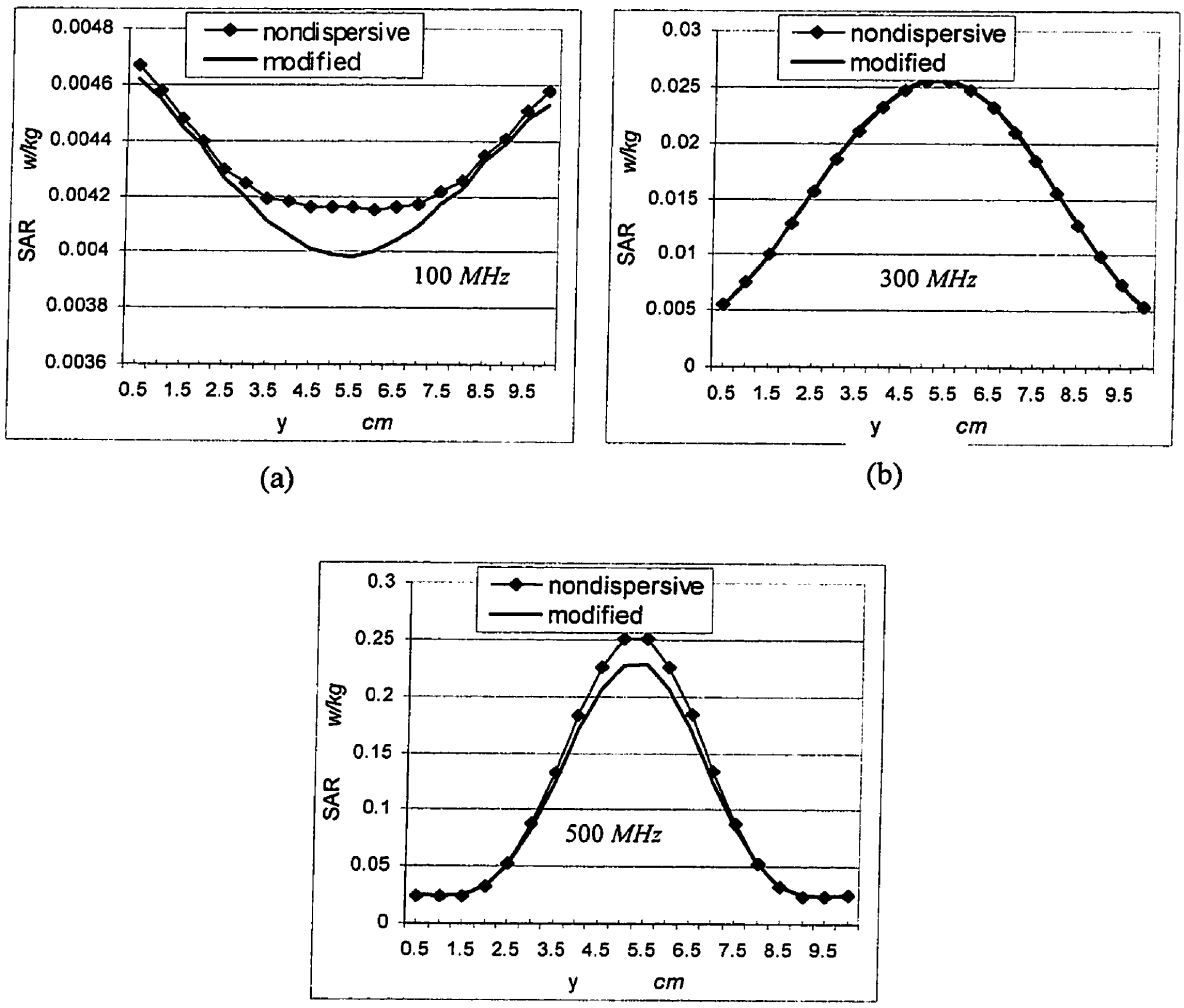

Fig. 3.10 SAR obtained from modified *TLM* and nondispersive *TLM* in the center of the cube along the *y*-axis for the case of a strong scatterer (brain & nerve tissue).

In the following numerical simulation, the method is applied to a geometrically complex inhomogeneous second order Debye dielectric body. A rough model of the human head [64] is used. The head is divided into five layers and 209 cells, $2 \times 2 \times 2\,cm$ each. Fig. 3.11 shows the consecutive layers constituting the head and different kinds of tissue involved. The TLM mesh is formed of $50 \times 50 \times 50$ nodes with $\Delta t = 0.0334ns$. Fig. 3.12 shows the SAR distribution at different layers of the head at $300MHz$. As shown the SAR distribution is different in each layer because of the

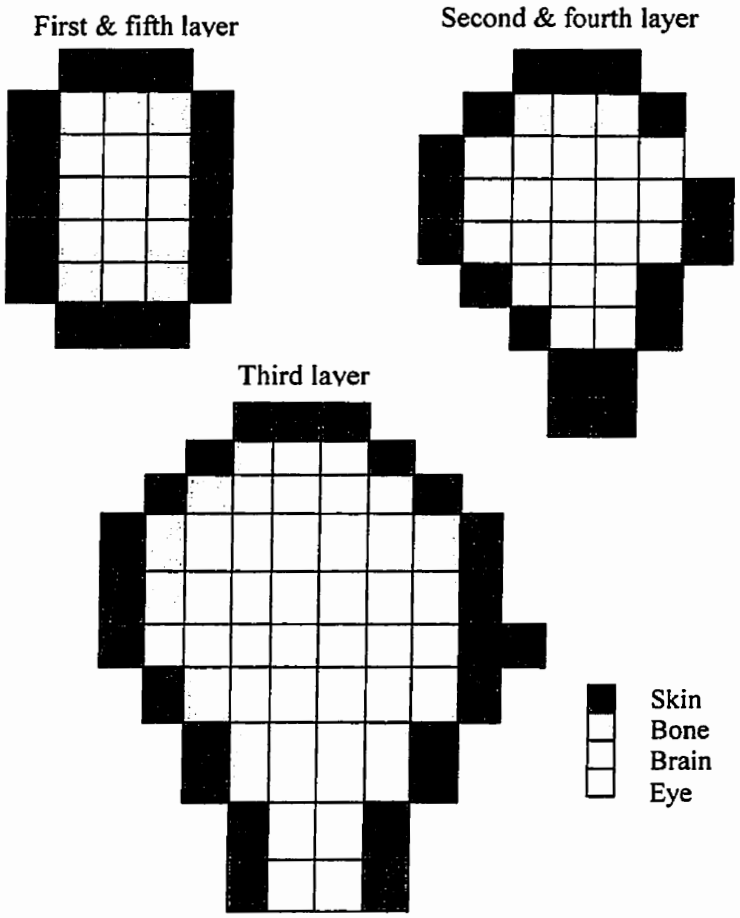

Fig. 3.11 Five different layers forming the human head.

interaction of the electromagnetic waves with the different kinds of tissue involved. The amount of energy absorbed by bone tissue is very small compared to that absorbed by the other kinds of tissue. This follows directly from the dielectric properties of the bone tissue. Using the real and imaginary parts of the second order Debye equation to obtain the permittivity and loss tangent at $300MHz$ for the brain, eye and skin tissue, shows that the three kinds of tissue have almost the same dielectric properties at $300MHz$. This explains why the absorption in these tissues is approximately the same.

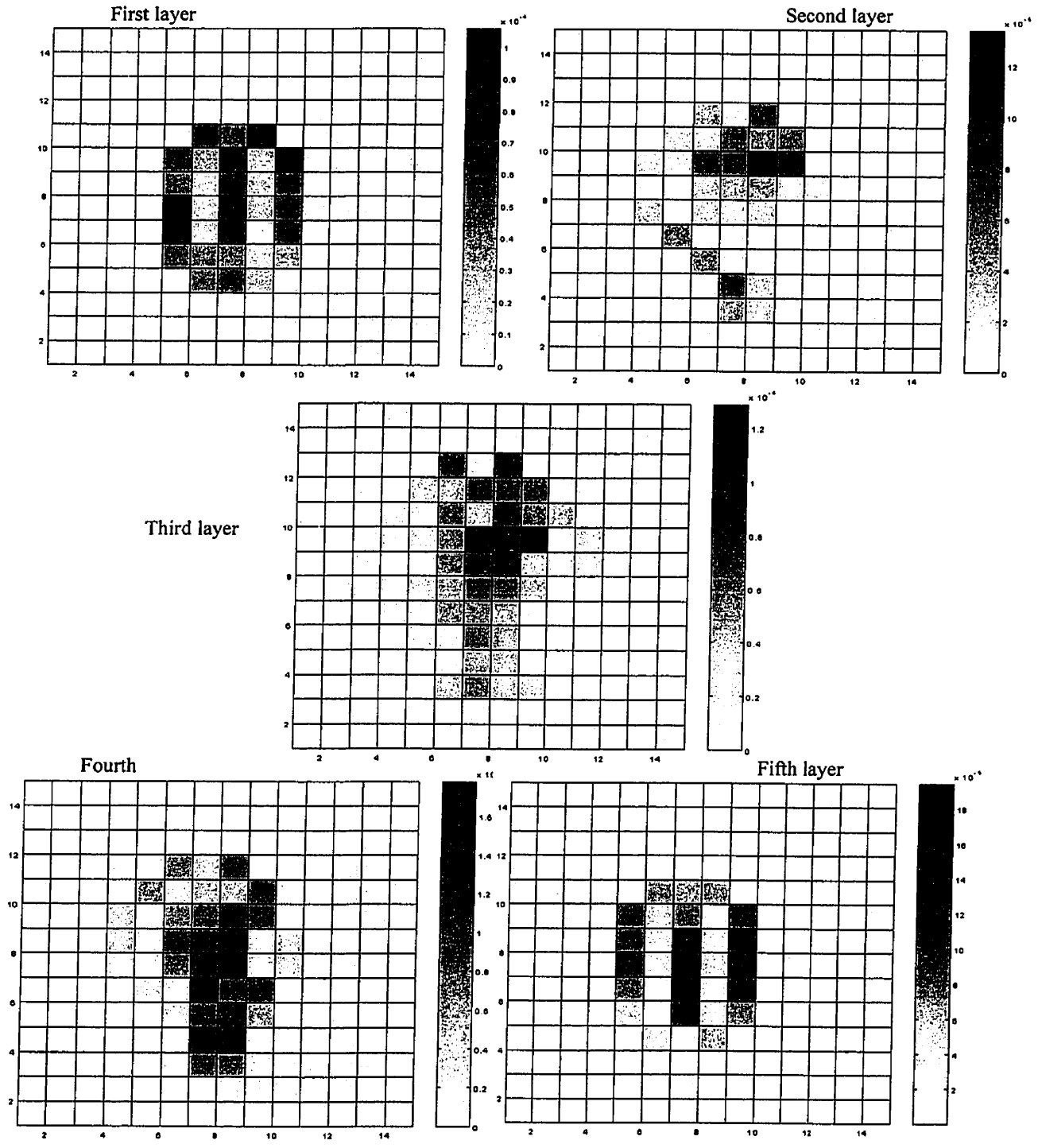

Fig. 3.12 SAR distribution in the five layers forming the head at 300 *MHz.*

The next simulation involves a refined model of the human head based on the model in [65]. The head is divided into 24 layers and 24552 cells each of dimension $7 \times 7 \times 7\ mm$. Five kinds of tissue are involved: bone, skin/fat, muscle, brain and eye. Fig. 3.13 shows a section through the middle of the head. The TLM mesh is formed of $50 \times 50 \times 50$ nodes with $\Delta t = 0.01167 ns$. The Guassian pulse had $t_o = 50\delta t$ and $T = 20\delta t$ and at least 9 cells were taken to the boundary. The incident wave was propagating in the z direction and polarized in the x direction. Fig. 3.14 shows the SAR distribution at three different layers through the head obtained using the modified TLM at $300 MHz$. From the plot, it is apparent that more energy in deposited to the brain and muscle tissue.

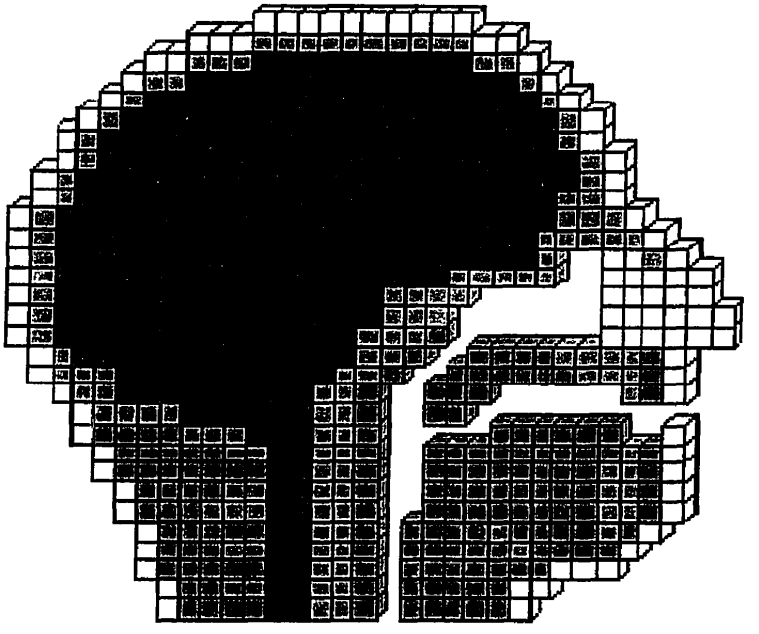

Fig. 3.13 Section through the middle of the head.

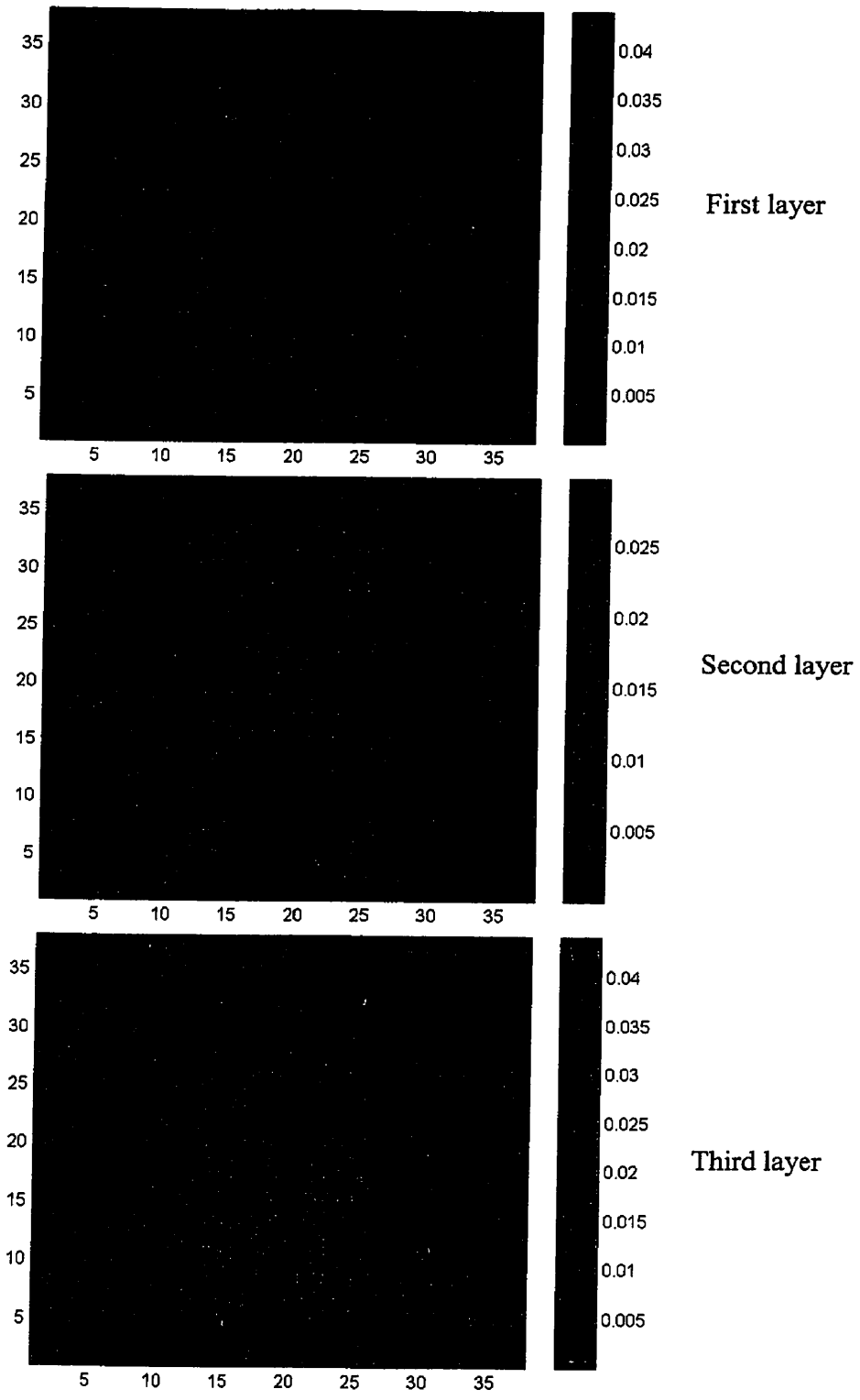

Fig. 3.14 SAR (W/kg) distribution in three layers of the head at 300*MHz*.

The last simulation involves a much finer model of the human head based on the model used in the previous simulation. The cell size in this model is $3.5\times3.5\times3.5\,mm$. So the location of each cell in the previous model is now occupied by 8 cells. The total number of cells is 196416. Five kinds of tissue are involved: bone, skin/fat, muscle, brain and eye. The TLM mesh is formed of $100\times100\times100$ nodes with Δt = 5.83737 *ps*. The incident wave was propagating in the z direction and polarized in the x direction and the Gaussian pulse had $t_0=100\delta t$ and $T=40\delta t$.

The number of iterations is twice that used in the previous simulation, thus making the simulation time the same. Fig. 3.15 shows the SAR distribution at three different layers through the head obtained using the modified TLM at 300*MHz*. These three layers are at the same position as those used in the previous example. Yet, each layer in the previous simulation is occupied by two layers in that simulation. Comparing Fig. 3.14 and Fig. 3.15, shows that although the values of the SAR distribution are different in both figures, the absorption pattern is the same. The maximum SAR values occur at the same locations. The difference in the SAR distribution values is due mainly to the resolution used.

To better compare the results of the two simulations, Fig. 3.16 shows the SAR distribution of a layer obtained using cell size = 7*mm* and the SAR distribution of the two equivalent layers obtained using cell size = 3.5*mm*. In this figure, the SAR values of the two equivalent layers are averaged at each cell to form a single layer. As shown in Fig. 3.16, after averaging, the difference in the SAR distribution obtained from both simulations became much less. The average value of the SAR distribution of the first

layer (a), in Fig. 3.16, is $0.003808 W/kg$. While for the second layer (b), the average value of the SAR distribution is $0.003658 W/kg$.

The parameters of the second order Debye equation for the tissue involved in the simulations are obtained using [60], [47] and [66] and given in Table 3.1. These parameters fit the actual data in the range $0.1 MHz$ to $1.1 GHz$.

Table 3.1: Debye constants for tissues $\tau_1 = 46.25\, ns$ and $\tau_2 = 0.307\, ns$.

Tissue	ε_∞	ε_{s1}	ε_{s2}
Bone	5.8	312.8	7.11
Brain/Nerve	48.1	2064.	56.86
Muscle	52.01	3948.	59.09
Skin	43.8	3399.	55.59
Eye	50.8	2191.	56.99

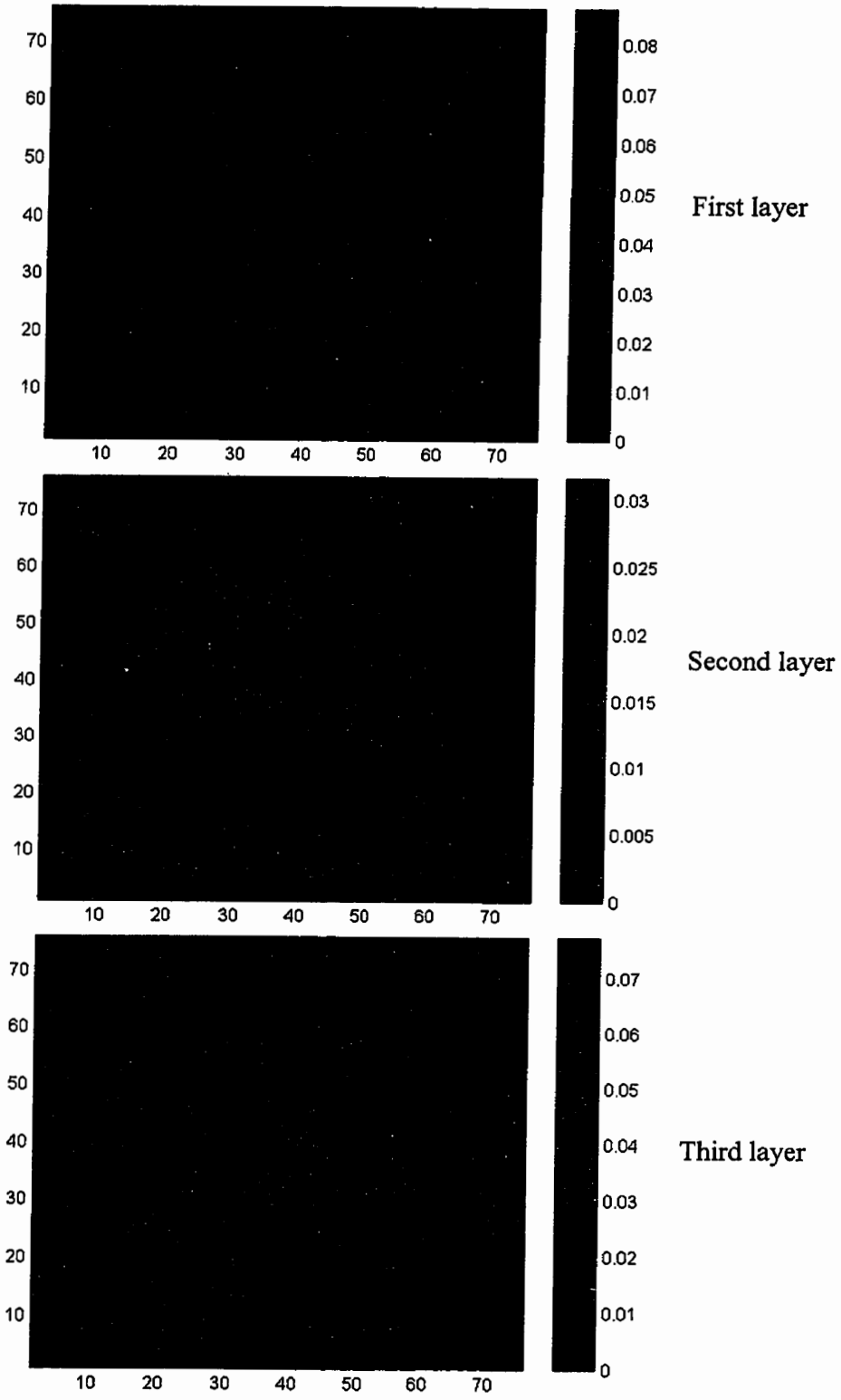

Fig. 3.15 SAR (W/kg) distribution in three layers of the head at 300*MHz*.

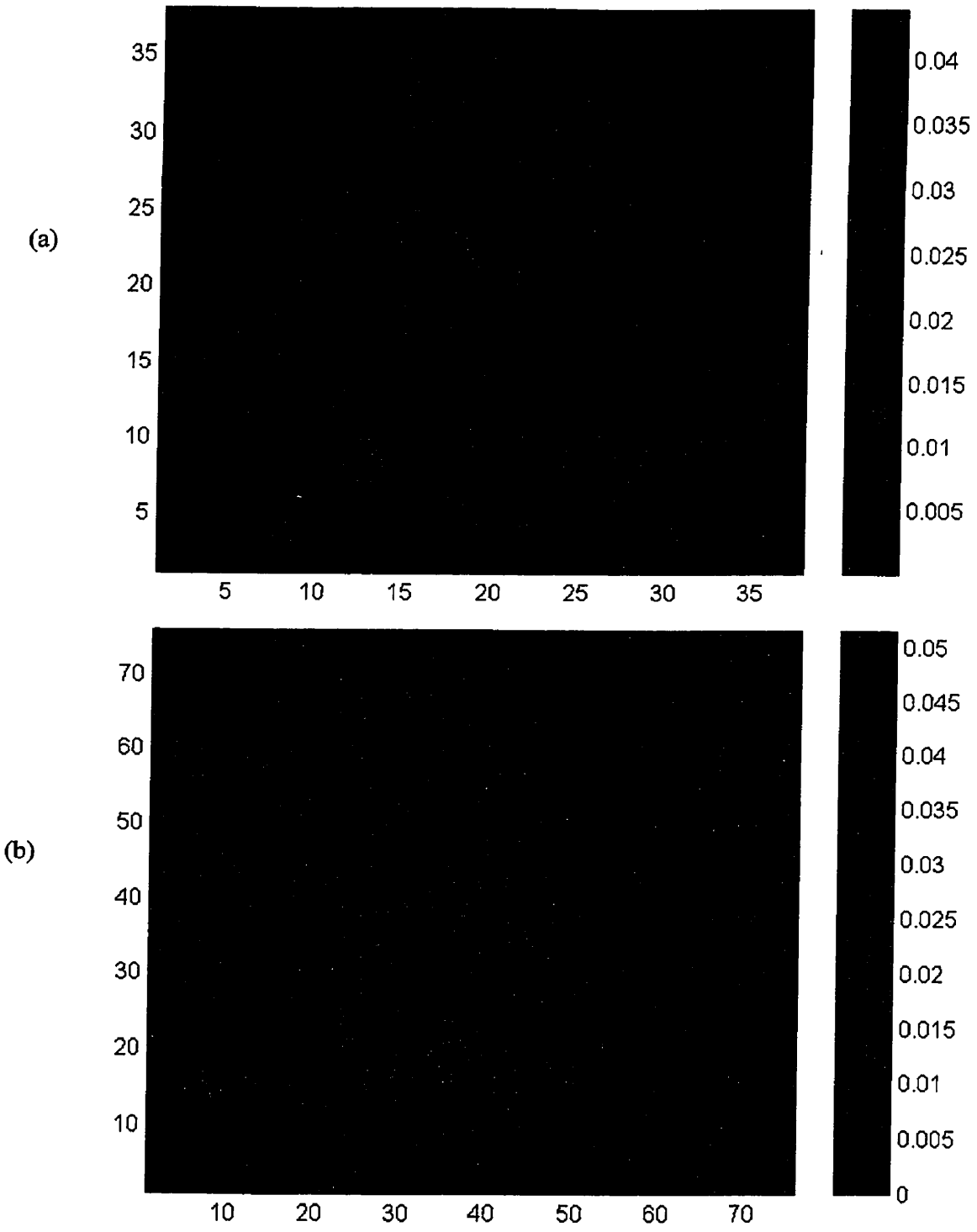

Fig. 3.16 SAR (W/kg) distribution at 300*MHz* in (a) layer of the head with cell size 7*mm* and (b) equivalent layer with cell size 3.5*mm*.

3.7 Conclusion:

In this chapter, we presented a review of the symmetric condensed node SCN TLM method. The scattering procedure for free space propagation is first presented. The dispersive nature of biological tissue is reviewed. The most common approximations that are used to model the complex permitiivity are given. A quick review of modeling dispersive materials in the FDTD method is then provided. The modeling of frequency dependent or dispersive materials in TLM method is then discussed, Sources or lumped element networks are employed in the modeling of frequency dependent materials. These networks or sources are connected to the node using transmission lines of characteristic admittance equals to the driving admittance of the node. These equivalent sources are calculated at each time step and included in the scattering procedure of the TLM. The circuit model that can be used to model second order Debye dielectrics is given. The necessary modifications to the scattering process in order to account for the dispersive nature of the medium are pointed out.

Several numerical simulations are then carried out to check the validity and accuracy of the modified TLM technique for dispersive homogeneous and nonhomogeneous dielectric bodies. The modified TLM technique is then applied to nonhomogeneous and geometrically complex dispersive body, which is the human head. Three models of the head are used a simplified model of 209 coarse cells, a refined model of 24552 cells and a much refined model of 196416 cells. The near field data and the SAR distribution obtained from the modified TLM are compared to those obtained from the stub-loaded or nondispersive SCN TLM method assuming a nondispersive nature of biological tissue.

CHAPTER 4

Reconstruction of Dielectric Bodies

4.1 Introduction:

The reconstruction of dielectric bodies using interrogating microwave and near field scattered data has been widely considered in recent years. Because of the inherent properties of microwave radiation, which can be used to detect objects, microwave imaging has been of interest in various areas such as geophysical exploration, remote sensing, nondestructive testing and medical imaging [67]-[70].

The interest in developing microwave-based techniques, when other powerful imaging techniques are available, is mainly due to the nature of the interaction between microwave radiation and the dielectric bodies, and the fact that different physical parameters are visualized. Dielectric materials are modeled via their complex permittivities that describe the nature of the propagation of microwave radiation within dielectric bodies. These complex permittivities are directly related to the morphology, blood flow, water content and temperature of the tissue, thus leading to a large dielectric contrast among different biological tissues. In human soft tissue there is only a 2% diversity in X-ray absorption, whereas the dielectric diversity of human soft tissue is very

large. For example, the dielectric constant at microwave frequencies for fat is about 4 and is approximately 80 for the cerebral fluid [70].

The fact that microwave imaging involves the use of non-ionizing, low power radiation, and is thus less hazardous than other forms of radiation, makes continuous monitoring of the human body potentially feasible. Since the dielectric constant is highly related to the water content of the tissue, microwave imaging has an advantage over ultrasound imaging in its ability to penetrate air and bone, and has been used to detect cerebral edema [71] and pulmonary edema [72].

Unfortunately, research in microwave imaging is still in the preliminary stages, basically because of the difficulties in developing adequate reconstruction algorithms. These difficulties occur because microwaves do not travel in a straight line inside an inhomogeneous dielectric object. This makes imaging techniques significantly more complicated than linear-propagation based techniques that are used for X-rays. Based upon this, reconstruction techniques are divided into two main categories. Those that involve modification of the already available X-ray linear reconstruction algorithms, usually referred to as spectral domain techniques [73]-[79], and others that are based on electromagnetic inverse scattering and are referred to as spatial domain techniques [80]-[102]. Other techniques involved the use of stochastic procedures such as the maximum entropy [103] and simulated annealing [104], [105].

In the spectral domain approach, or microwave tomography, the body under investigation is illuminated by a plane wave and the scattered field is measured using a linear array of probes in a way similar to that used in diffraction tomography. Fast Fourier transformation, is then used to obtain the spectrum of the scattered field, which is

the main advantage of this approach. This spectrum contains information about the dielectric properties of the body. By repeating the measurement for different directions of incidence, the spectral domain can be filled and inverted to obtain the image of the body. The main drawback of the spectral domain techniques is its limited validity for reconstructing lossless, low contrast dielectric bodies and in the presence of weak scatterers only.

In the spatial domain approach, the body is illuminated by an incident field and the scattered field is measured and used to reconstruct the dielectric permittivity distribution of the body. The aim is to solve the exact equation of the electromagnetic inverse scattering problem by numerical methods such as the method of moments (MoM) [3]. The problem is reduced to the solution of linear system of algebraic equations. Unfortunately, the scattering matrix which governs the external scattered field induced by internal equivalent currents is highly ill-conditioned. Thus any attempt to get its inverse makes the system ill-posed. By ill-posedness, we refer to the Hadamard sense [106], in which the existence, uniqueness and stability of the solution are not simultaneously ensured. Another disadvantage of the inverse scattering approach is that sampling the scattered field outside the body is very susceptible to noise. Because of the system ill-posedness, the effect of this noise is very strong. Several regularization techniques have been used [88], [95], [97], [101] aiming to reduce the effect of ill-conditioning. These employ a priori information either to select a suitable regularization parameter or to enforce convergence in iterative techniques. This process is normally combined with multi-illumination techniques, in which several directions or angles of incidence are used, aiming to decrease the effect of uncertainties in the measured scattered field.

Most of the recent work involves two-dimensional problems. Three-dimensional problems are usually more complex and reliable reconstructions are harder to obtain. In this thesis, the unrelated illumination method which has been tested before with two-dimensional bodies [107], [108], is extended to handle three-dimensional inhomogeneous dielectric bodies. This method utilizes the method of moments (MoM) to discretize the integral equation that relates the scattered field data and the complex permittivity. Yet, it differs from other techniques in that the way of acquiring information helps overcoming the ill-posedness nature of the problem. Numerical simulations are carried out to assess the method and to test its robustness in the presence of measured data uncertainties. To evaluate the method as a tool for medical imaging it is further tested with a model of the human head [64], and a 180-cell model of the human body [109].

In this chapter, the basic mathematical formulation of the inverse scattering problem and the definitions of some of the often used terms in microwave imaging are reviewed, together with discussion of some of the reconstruction techniques that have been used earlier.

4.2 Integral Equation Formulation:

Consider an inhomogeneous dielectric body of arbitrary shape that is characterized by a dielectric constant $\varepsilon_r(r)$ and an electric conductivity $\sigma(r)$, both generally variable from point to point situated in a homogeneous medium with known permittivity ε_o, as shown in Fig. 4.1. If an electromagnetic incident wave crosses this body, a scattered field, which is related to the properties of the dielectric scatterer, is produced. From the scattered field measurements, the location, the shape and complex

permittivities of the body may be determined. The determination of the location and shape of the scatterer is known as qualitative imaging, while quantitative imaging involves the determination of the complex permittivity distribution within the scatterer.

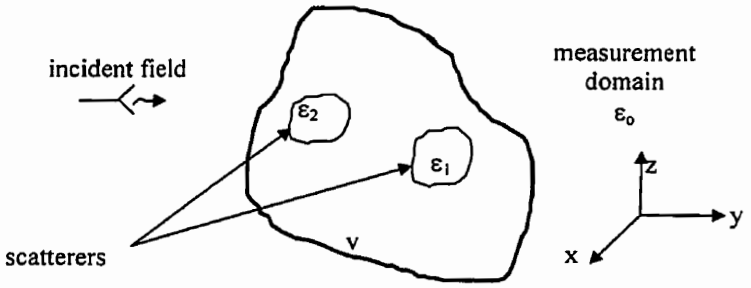

Fig. 4.1 Geometry of the three-dimensional problem.

The dielectric properties of the body V in Fig. 4.1 can be expressed in terms of the complex permittivity constant as:

$$\varepsilon^*(r) = \varepsilon'(r) - j\varepsilon''(r) \tag{4. 1}$$

where

$$\varepsilon'(r) = \varepsilon_r(r) \quad \text{and} \quad \varepsilon''(r) = \frac{\sigma}{\omega\varepsilon_o} \tag{4. 2}$$

If the body is illuminated by an incident plane wave, the induced current in the body gives rise to a scattered field $\mathbf{E}^s$. This field may be accounted for by replacing the body with an equivalent current density $\mathbf{J}_{eq}$ given by:

$$\mathbf{J}_{eq}(r) = (\sigma(r) + j\omega[\varepsilon(r) - \varepsilon_o])\mathbf{E}(r) \qquad (4.3)$$

The first term in equation (4.3) is the conduction current density, while the second term is the polarization current density. $\mathbf{E}(r)$ is the total electric field inside the body.

Using the equivalent current density, we can obtain the scattered fields by solving Maxwell's equations:

$$\nabla \times \mathbf{E}^s = -j\omega\mu\mathbf{H}^s$$
$$\nabla \times \mathbf{H}^s = \mathbf{J}_{eq} + j\omega\varepsilon_o\mathbf{E}^s \qquad (4.4)$$

$\mathbf{H}^s$ is the scattered magnetic field and μ is the permeability, assumed that of free space μ_o. To eliminate $\mathbf{H}^s$, we take the curl of equation (4.4)

$$\nabla \times \nabla \times \mathbf{E}^s = -j\omega\mu_o\left((\nabla \times \mathbf{H}^s\right) = -j\omega\mu_o(\mathbf{J}_{eq} + j\omega\varepsilon_o\mathbf{E}^s) = -j\omega\mu_o\mathbf{J}_{eq} + \omega^2\mu_o\varepsilon_o\mathbf{E}^s \qquad (4.5)$$

Substituting for $\mathbf{J}_{eq}$ in equation (4.5) and rearranging:

$$\nabla \times \nabla \times \mathbf{E}^s - \omega^2\mu_o\varepsilon_o\mathbf{E}^s = -j\omega\mu_o(\sigma + j\omega(\varepsilon - \varepsilon_o))\mathbf{E} \qquad (4.6)$$

Equation (4.6) can be further written as:

$$\nabla \times \nabla \times \mathbf{E}^s - k_o^2\mathbf{E}^s = (k^2 - k_o^2)\mathbf{E} \qquad (4.7)$$

where $k = \left(\omega\sqrt{\mu_o\varepsilon_o(\varepsilon_r - j\frac{\sigma}{\omega\varepsilon_o})}\right)$ and $k_o = \left(\omega\sqrt{\mu_o\varepsilon_o}\right)$ are the wave numbers inside and outside V, respectively.

The solution to equation (4.7) is given in terms of the magnetic vector potential **A**:

$$\mathbf{E}^s = -j\omega\left[1+\frac{1}{k_o^2}\nabla\nabla\cdot\right]\mathbf{A} \tag{4.8}$$

where

$$\mathbf{A} = \mu\int_v G_o(r,r')\mathbf{J}_{eq}(r')dv' \tag{4.9}$$

and

$$G_o(r,r') = \frac{e^{-jk_o(r-r')}}{4\pi|r-r'|} \tag{4.10}$$

is the free space scalar Green's function. The operator $\nabla\nabla\cdot\mathbf{A}$ is defined as $\nabla\nabla\cdot\mathbf{A} = \nabla(\nabla\cdot\mathbf{A})$. Assuming that $\mathbf{J}_{eq}$ is an infinitesimal elementary source at r' pointed in the x direction so that:

$$\mathbf{J}_{eq} = \delta(r-r')\mathbf{a}_x \tag{4.11}$$

Using equation (4.9), the magnetic vector potential **A** can be written as:

$$\mathbf{A} = \mu_o G_o(r,r')\mathbf{a}_x \tag{4.12}$$

If $\mathbf{G}_{ox}(r,r')$ is the electric field produced by the elementary source that is pointing in the x direction, then $\mathbf{G}_{ox}(r,r')$ must satisfy:

$$\nabla\times\nabla\times\mathbf{G}_{ox}(r,r') - k_o^2\mathbf{G}_{ox}(r,r') = -j\omega\mu_o\delta(r,r') \tag{4.13}$$

with solution

$$\mathbf{G}_{ox}(r,r') = -j\omega\mu_o\left[1+\frac{1}{k_o^2}\nabla\nabla\cdot\right]G_o(r,r') \tag{4.14}$$

$\mathbf{G}_{ox}(r,r')$ is referred to as a free space vector Green's function with a source pointing in the x direction. Similarly, $\mathbf{G}_{oy}(r,r')$ and $\mathbf{G}_{oz}(r,r')$ correspond to infinitesimal, elementary sources pointing in the y and z direction, respectively. The three vector Green's function can be combined together to form the free space dyadic Green's function:

$$\overline{\overline{\mathbf{G}}}(r,r') = \mathbf{G}_{ox}(r,r')\mathbf{a}_x + \mathbf{G}_{oy}(r,r')\mathbf{a}_y + \mathbf{G}_{oz}(r,r')\mathbf{a}_z \tag{4. 15}$$

The free space dyadic Green's function is the solution to the Dyadic differential equation:

$$\nabla \times \nabla \times \overline{\overline{\mathbf{G}}}(r,r') - k_o^2 \overline{\overline{\mathbf{G}}}(r,r') = \tilde{I}\delta(r,r') \tag{4. 16}$$

where $\tilde{I}$ denotes the unit dyad. $\overline{\overline{\mathbf{G}}}(r,r')$ is the electric field at a field point r due to an infinitesimal source at r'.

Using the free space dyadic Green's function $\overline{\overline{\mathbf{G}}}(r,r')$, equation (4.7) can be written as:

$$\mathbf{E}^s(r) = \int_v \overline{\overline{\mathbf{G}}}(r,r')(k^2(r') - k_o^2)\mathbf{E}(r')dv' \tag{4. 17}$$

$(k^2(r) - k_o^2)$ is usually referred to as the contrast or the object function **O**(r) and using (4.1) and (4.2) **O**(r) can be written as:

$$\mathbf{O}(r) = (k^2(r) - k_o^2) = k_o^2(\varepsilon_r(r) - 1 + \frac{\sigma(r)}{j\omega\varepsilon_o}) = k_o^2(\varepsilon^*(r) - 1) \tag{4. 18}$$

The treatment of the singularity in equation (4.17) is discussed in appendix B.

The total electric field **E** at an arbitrary point r can be expressed as:

$$\mathbf{E}(r) = \mathbf{E}^i(r) + \mathbf{E}^s(r) \tag{4. 19}$$

where $\mathbf{E}^i(r)$ is the incident field. Using (4.17) and substituting for the scattered field in (4.19):

$$\mathbf{E}(r) = \int_v \overline{\overline{\mathbf{G}}}(r', r)\mathbf{O}(r')\mathbf{E}(r')dv' + \mathbf{E}^i(r) \tag{4. 20}$$

Equations (4.17) and (4.20) are the basic integral equations for microwave imaging. Once the scattered fields are measured by detectors at observation points, the complex permittivity distribution of the unknown body can be reconstructed by solving these two coupled integral equations.

4.2.1 Integral Equation with Equivalent Current Modeling:

Equations (4.17) and (4.19) can be linearized [110] by introducing an equivalent current density $\mathbf{J}_{eq}(r)$

$$\mathbf{J}_{eq}(r) \equiv \frac{j}{\omega\mu_o}\mathbf{O}(r)\mathbf{E}(r) \tag{4. 21}$$

and the scattered field and total field can be written as:

$$\mathbf{E}^s(r) = -j\omega\mu_o \int_v \overline{\overline{\mathbf{G}}}(r, r')\mathbf{J}_{eq}(r')dv' \tag{4. 22}$$

$$\mathbf{E}(r) = -j\omega\mu_o \int_v \overline{\overline{\mathbf{G}}}(r, r')\mathbf{J}_{eq}(r')dv' + \mathbf{E}^i(r) \tag{4. 23}$$

The reconstruction procedure can also be performed by solving the linear equation (4.22) from the scattered field measurements to obtain the equivalent current

distribution within the object. The total field inside the body can then be calculated using equation (4.23). The object function or the permittivity distribution of the dielectric body can then be predicted using equation (4.21).

4.2.2 Integral Equation with Born Approximation:

The Born approximation is a widely accepted approximation and usually applied in microwave tomography. For low contrast inhomogeneous dielectric bodies, the magnitude of the scattered field in the object is very small compared to that of the incident field. Thus the scattered field inside the object can be neglected and the total field can be approximated by the incident field. Based on this approximation, the scattered field (4.17) can be written as:

$$\mathbf{E}^s(r) = \int_v \overline{\overline{\mathbf{G}}}(r,r')\mathbf{O}(r')\mathbf{E}^i(r')dv' \qquad (4.24)$$

4.2.3 Integral Equation with Rytov Approximation:

The Rytov approximation is another approximation that is used in microwave tomography. It is based on the fact that the change in the scattered phase over one wavelength is small. The phase Φ of the scattered field can be expressed as:

$$\Phi(r) = \frac{1}{\mathbf{E}^i(r)} \int_v \overline{\overline{\mathbf{G}}}(r,r')\mathbf{O}(r')\mathbf{E}^i(r')dv' \qquad (4.25)$$

It has been proven that the Born approximation produces a better estimate of the scattered field for small sized objects with large deviations in the refractive index. On the

other hand the Rytov approximation gives a more accurate estimate of the scattered field for large sized objects with small deviations in the refractive index. The refractive index is defined as the square root of the permittivity under the assumption that the permeability of the body is that of free space.

4.3 Ill-posed Problems:

Many problems of mathematical physics can be formulated in terms of an operator equation

$$\mathbf{Ax} = \mathbf{y} \tag{4.26}$$

Typically, **y** denotes the system output, **x** denotes the unknown being sought and **A** is the system operator. Given **A** and **y**, the objective is to determine **x**. According to the Hadamard definitions [106], the problem is well-posed if the following conditions are satisfied:

1) For each element **y**, there is a solution **x**: that is the *existence* condition.

2) The solution **x** is unique for a given **y**: that is the *uniqueness* condition.

3) For small perturbations in **y** there are small perturbations in **x**: that is the *stability* condition.

The problem is said to be ill-posed if at least one of the above conditions is violated. There are three main reasons that cause this ill-posedness, namely, incompleteness of the input data, numerical errors in the input data and/or the nature of the system operator **A**. In order to solve an ill-posed problem, special techniques have to be employed to regularize the problem [111]. The solution to the regularized problem

will be well-behaved and will offer a reasonable approximation to the solution of the ill-posed problem. In particular, an ill-posed problem may be regularized by:

a) changing the definition of what is meant by an acceptable solution,

b) changing the space to which the acceptable solution belongs,

c) revising the problem statement,

d) introducing regularization operators, and

e) using statistical techniques.

4.4 Previous Work:

In this section twelve microwave imaging methods proposed by various researchers in recent years are briefly reviewed, together with a discussion of their advantages and limitations. These are: the microwave tomography technique, the psuedoinverse method with equivalent current modeling, the Born and distorted Born iterative methods, a Newton type iterative method, an adaptive iterative algorithm, Levenberg-Marquardt method, the conjugate gradient method, the hybrid element method, the stochastic inversion method, the maximum entropy method, the simulated annealing approach, and the time domain method.

4.4.1 Microwave Tomography:

This approach is based on the Fourier diffraction projection theorem. It has been applied to cross-sectional or two-dimensional and three-dimensional imaging [73]-[79]. Conventional microwave tomography systems are based on illuminating the body by a set of plane waves. For each illumination, the forward scattered field is sampled along a

straight line, for the two-dimensional case, and on a plane for the three-dimensional case. Either Born or Rytov approximations is applied, thus forcing the assumption that the inhomogeneities in the body are weak scatterers. The Fourier transform of the forward scattered field gives the values of the two-dimensional Fourier transform of the object along a circular arc in the two-dimensional Fourier spectral domain. According to the Fourier diffraction projection theorem, by illuminating the body from different directions and repeating the same procedure the spectral domain can be filled with samples of the body over an ensemble of circular arcs. Using Fourier inversion, the body can then be reconstructed.

The main advantage of microwave tomography is using an existing efficient numerical algorithm, which is the fast Fourier transform (FFT). This makes the speed of the data processing fast enough to allow for real time imaging. However, microwave tomography is subject to both mathematical and experimental limitations. The mathematical limitations are imposed by Born and Rytov approximations. These approximations are fundamental to the reconstruction process and limit the range of objects that can be examined. The experimental limitations are due to the finite amount of the collected data, which in turn limits the resolution of the permittivity distribution reconstruction.

4.4.2 Psuedoinverse with Equivalent Current Modeling:

Ney *et al* [81] was the first to propose the method of psuedoinverse transformation to microwave imaging. In this method the linearized integral equations, via equivalent current modeling, are first transformed into matrix equations using the

method of moments (MoM). The complex permittivities are then derived using the following procedure: first the equivalent current distribution is obtained from the measured scattered field, second this current distribution is used to obtain the total field. Knowing the total field and the equivalent current, the object function is obtained and thus the permittivity distribution. The first step involves the use of the psuedoinverse transformation [82] to obtain the inverse of an ill-conditioned matrix. The psuedoinverse transformation is a very powerful method in dealing with ill-conditioned matrix equations. The solution obtained is a minimum norm least square solution. Coarsi *et al* [83]-[88] have further developed the method and applied it to two and three-dimensional electromagnetic imaging problems. So far the method has been applied only to simple geometries, with a small number of weakly scattering inhomogeneities. To obtain acceptable results, especially in three-dimensional imaging problems, the method employs the use of multi-illumination together with the constraint that the number of measurement points is larger than the number of discretization cells.

As there are no iterations involved in this method, the computation time is small compared to that of the iterative methods, which is the main advantage of the method. To improve the quality of the reconstructed image, a priori information, regarding the geometry and the dielectric properties, have been lately utilized in the reconstruction process. Yet, the filtering effect inherent in this method limits the resolution of the reconstruction especially for high noise levels in the measured scattered field.

4.4.3 Born and Distorted Born Iterative Methods:

Iterative methods with regularization in the space domain have become popular in

recent years. Wang and Chew [89] proposed the Born iterative method in which the total electric field and the distribution of the electric parameters are updated by solving the direct and inverse problem separately in each iteration. The outline of the approach can be summarized as follows:

(1) The linearized inverse scattering problem is solved using the Born approximation.

(2) The scattering problem is solved for the field in the object and at the measuring points using the object function obtained in the first step.

(3) The calculated fields in step (2) are used to solve the inverse problem and obtain the next order object function.

(4) Repeat step (2) comparing the scattered field at the observation points, obtained using the reconstructed object function, with measured fields at the same observation points. When the difference is acceptable, the iteration terminates.

It should be noted that the Green's function remains unchanged during the iteration procedure (only the field in the scatterer is updated). One immediate extension of this method is to update the Green's function in each iteration together with the field in the scatterer. This is known as the distorted Born iterative method [90]. The outline of this method is almost the same as that of the Born iterative method, except that in the second step an updated Green's function should be calculated using the last reconstructed permittivity distribution. Both methods have been tested with two-dimensional objects only.

The results obtained using these two methods show that, for noiseless cases, the distorted Born iterative method is superior to the Born iterative method because of its faster convergent speed. While for noisy cases, the Born iterative method is more robust

than the distorted Born iterative method. Also, it was shown [112] that the Born iterative method can handle electrically large scatterers with low permittivity contrast.

4.4.4 The Newton Iterative Methods:

Joachimowicz *et al* [91] proposed a Newton iterative method to construct the complex dielectric permittivity distribution. In this method, the integral equations are first transformed into matrix equations using the method of moments (MoM). Then an iterative procedure is developed as follows:

(1) Starting from an initial guess of the permittivity distribution and hence the object function, the total field inside the body is calculated.

(2) The forward scattering problem is then solved for the field at the measuring points.

(3) The error between the scattered field computed in (2) and the measured field (obtained through solving the forward scattering problem using the exact permittivity distribution) is calculated

(4) The first order estimation of the object function error is obtained and the object function is updated using this error

The iterations go on until the error in the calculated scattered field is acceptable. In this procedure, step (4) involves obtaining the inverse of an ill-conditioned matrix, so standard Tikhonov regularization [92] is used to stabilize the results. Yet, the regularization factor used in this process involves a parameter that can only be determined empirically.

The main advantage of this techniques is its flexibility in considering a priori information. It provides quantitative imaging even with strong diffraction effects.

However, it requires the use of a multi-illumination technique in order to obtain accurate reconstructions. Also, the required computational time is extensive.

4.4.5 An Adaptive Iterative Algorithm:

Liu *et al* [93], [94] proposed an adaptive algorithm that optimizes the iterative process by using, selectively, a different iterative technique for each iteration. The iterative techniques involved are the Born iterative technique and the Newton iterative technique. A decreasing ratio of error in the scattered field is used as a criterion for selecting a more suitable technique for each iteration. This algorithm requires the use of multi-view illumination and Tikhonov regularization. It has been applied successfully to two-dimensional objects in the presence of noise in the measured field data.

4.4.6 Levenberg-Marquardt Method:

This method has been proposed lately by Franchois *et al* [95] to obtain a quantitative reconstruction of the complex dielectric property distribution of biological objects. The method is a modification of the Gauss-Newton iterative method and is equivalent to the distorted Born iterative method. The method of moments is applied to discretize the nonlinear integral equation relating the scattered field data and the complex permittivity. The resulting system of nonlinear equations is linearized in each iteration, regularized, via Tikhonov regularization, and then solved for an updating correction of the complex permittivity in the iterative procedure. The regularization parameter used can either be obtained empirically, or using a generalized cross validation (GCV) method. In fact, this method is very similar to Newton iterative method and its main modification

and advantage is using the GCV method to get the regularization parameter.

The Levenberg-Marquardt method requires the use of multi-view illumination and imposes a priori bounds on the complex permittivity in order to accelerate the convergence. The method has only been applied to two-dimensional objects immersed in water. The use of the generalized cross validation method for choosing the regularization parameter has proven to be successful in the case of weak homogeneous scatterers and strong homogeneous scatterers with an initial guess in the neighborhood of the solution. For strongly scattering inhomogeneities, the reconstruction is of lesser quality.

4.4.7 The Conjugate Gradient Method:

The conjugate gradient method was discussed in [97] as a tool to handle ill-posed matrix equations resulting from the method of moments. This iterative method is similar to the steepest descent method which involves the search for the minimum of a function in a direction suggested by its negative gradient. It starts with an initial guess that generates the first residual vector and the direction vector. Then, the system is solved iteratively. The conjugate gradient method has the advantage of having a rate of convergence practically insensitive to the initial guess, although a good initial guess reduces the number of iterations. The method has been applied to two and three-dimensional microwave imaging problems [97]-[98], and good reconstructions were obtained.

4.4.8 The Hybrid Element Method:

Meaney *et al* [99] proposed this method for two-dimensional image

reconstruction problems. The used computational methodology is a hybrid coupling of the finite element and the boundary element methods. In calculating the electric fields from the current estimates of the electrical properties, it seeks to take advantage of the strong points of the finite element method in the regions where the electrical properties are inhomogeneous or not known. It also utilizes the strengths of the boundary element method in the regions where the medium is homogeneous, unbounded in nature and the electrical properties are known. Coupling of these two methods occurs only at the boundary of the inhomogeneous dielectric object. The method employs a Newton iterative procedure together with multi-view excitation for image reconstruction. The reconstruction technique is very similar to that used by Joachimowicz *et al* [91]. The regularization employed is a blending of both Tikhonov and Marquardt approaches with regularization coefficients being determined empirically. One of the advantages of this method is the ability to use nonuniform meshing to handle available a priori information. The results obtained show that it operates best for smaller objects with low contrast. For the case of large objects and, or steep gradients, the method provides only qualitative images.

4.4.9 Stochastic Inversion Method:

The stochastic treatment of ill-posed problems has been successfully used in image processing and recognition techniques and seismology studies. Qin *et al* [100] applied the stochastic inversion of matrices to microwave imaging of two-dimensional dielectric bodies. The method requires an initial accurate guess, as inappropriate guesses can cause the algorithm to be slowly convergent or even divergent. The reconstruction

process can be summarized in the following steps. The linearized integral equation is discretized using the method of moments. The next step is to use the Tikhonov regularization to solve the inverse problem, the solution obtained is used as a priori data. Finally, using this a priori data, the stochastic inverse is applied to compute the equivalent current distribution within the body and hence the complex permittivity distribution.

The main advantage of this method is that it requires less computation time compared to other iterative techniques. Also, various criteria for choosing the regularization parameter [101], [102] were proposed. Single-view illumination yields accurate reconstruction only for simple objects with very small inhomogeneities. As the number of inhomogeneities increases, this requires the use of multi-view illumination.

4.4.10 The maximum Entropy Method:

Baribaud [103] applied the maximum entropy method to two-dimensional microwave imaging problems. The method, which belongs to stochastic techniques, is based on the information theory approach. It demands that one chooses from the available data the solution which uses the maximum information from the available data. In this method, the method of moments is used to discretize the integral field equation. The entropy is defined in terms of the current density distribution. The aim of the method is to maximize the difference between the entropy and the Gaussian and excess noise. The problem of maximization has no explicit solution and has to be solved iteratively. The image obtained using this method uses more of the available data and is a regularized solution. Also, the effect of the noise can be easily included in this method. Yet, the main

drawback is that although the method has only been applied to simple two-dimensional dielectric scatterers, the computational time needed is very long.

4.4.11 Simulated Annealing Approach:

This approach is based on stochastic techniques to search for the optimum state of a system and to avoid iterative processes being trapped to a local minimum. The usage of simulated annealing technique can bypass the need to invert large matrices and enables one to obtain the solution using an iterative procedure. This approach has only been applied to simple two-dimensional problems [104], [105] and its main disadvantage is the large computation time involved.

4.3.12 Time Domain Methods:

Moghaddam and Chew [112] proposed a method to solve a two-dimensional problem in time domain. In their method, the time domain problem is transformed by using Fourier transformation. The integral equation obtained in the time domain is transformed into a set of integral equations in the spatial domain with different frequencies and then solved using a Born iterative technique. In the computation, the dielectric distribution is assumed to be independent of frequency.

Batrakov *et al* [113] proposed an algorithm based on the Newton-Kantorovich iterative procedure and Tikhonov regularization for solving two-dimensional inverse problems in the time domain. In their algorithm, most of the calculations are given in an explicit form, thus reducing the computational time and making the algorithm suitable for real time processing. Yet, their analysis is restricted to cylinderical objects with

permittivity varying in the radial direction only. Later, they extended their work [114] to handle objects with arbitrary complex permittivity distributions. In doing so, they introduced complexity to the calculations compared to their earlier work.

The advantage of the time domain methods is that more information is available. However, the computational cost is huge compared to spatial domain methods because the fields or their spectrum have to be calculated at different times.

CHAPTER 5

Reconstruction of Dielectric Bodies Using Unrelated Illumination

5.1 Introduction:

The reconstruction methods proposed so far fall into two main categories, namely the spectral domain methods and the spatial domain methods. The spectral domain methods have the privilege of being based on and making use of a well-developed theory and techniques. Yet, employing the Born and Rytov approximation in the reconstruction makes it only applicable in the presence of weak scatterers and low contrast dielectric bodies. The spatial domain methods theoretically impose no restrictions on the complex permittivity distribution of the dielectric bodies to be reconstructed. The main disadvantages of these methods are their sensitivity to the noise and the long reconstruction time required.

In this chapter, we are going to proceed with the discretization of the integral equations derived in the previous chapter. This is followed by a discussion of the reconstruction procedure normally used in inverse scattering techniques, and the problem

of ill-posedness of the system and the most common regularization techniques used. Finally, the unrelated illumination method is presented and its use to handle three-dimensional lossless and lossy dielectric objects is discussed.

5.2 Discretization of the Integral Equations:

In Chapter 4, starting from Maxwell's equations, we have derived the integral equations governing the forward and inverse scattering problems. In order to solve these integral equations in the spatial domain numerically, they have to be discretized. The body is partitioned into N subvolumes. The n^{th} subvolume is denoted by V_n and the position of a representative interior point of V_n is denoted by r_n. Writing equation (4.20) as:

$$\mathbf{E}(r) = \int_v \overline{\overline{\mathbf{G}}}(r', r)\mathbf{O}(r')\mathbf{E}(r')dv' + \mathbf{E}^i(r) \tag{5. 1}$$

Applying the method of moments [3], we can expand the object function **O**(r) and the total field **E**(r) inside the body in a piece wise constant manner:

$$\mathbf{O}(r) = \sum_{n=1}^{N} O_n f_n(r) \tag{5. 2}$$

$$\mathbf{E}(r) = \sum_{n=1}^{N} E_n f_n(r) \tag{5. 3}$$

where f_n(r) is called the basis function and O_n and E_n are the coefficients. Using a pulse basis function:

$$f_n(r) = \begin{cases} 1, \ldots\ldots\ldots\ldots r \in V_n \\ \\ 0, \ldots\ldots\ldots\ldots r \notin V_n \end{cases} \tag{5.4}$$

Using Dirac delta as the weighting function, equation (5.1) can be rewritten as:

$$\mathbf{E}(r) - \mathbf{E}^i(r) = \sum_{n=1}^{N} \int_{v_n} \overline{\overline{\mathbf{G}}}(r_n', r_m) E_n O_n dv_n' \tag{5.5}$$

where r_m represents the m^{th} measurement point. In this way, we obtain a linear system that can be rewritten in a matrix form:

$$[\mathbf{E}] - [\mathbf{E}^i] = [\mathbf{G}_1][\mathbf{O}][\mathbf{E}] \tag{5.6}$$

or

$$[\mathbf{E}^i] = ([\mathbf{I}] - [\mathbf{G}_1][\mathbf{O}])[\mathbf{E}] \tag{5.7}$$

where $\mathbf{E}^i$ is a $3N$ dimensional array containing the components of the incident field at the N subvolumes, $\mathbf{E}$ is a $3N$ dimensional array containing the components of the total field at the N subvolumes. The matrix $\mathbf{O}$ is a $3N \times 3N$ diagonal matrix whose elements are the contrast or the difference of the wave number of the subvolume and that of the observation region which is assumed to be free space. $\mathbf{G}_1$ is a $3N \times 3N$ matrix depending on the wave number, cell size and location.

Following the same notation, the scattered field at the measuring points can be given by:

$$[\mathbf{E}^s] = [\mathbf{G}_2][\mathbf{O}][\mathbf{E}] \tag{5.8}$$

Where $\mathbf{E}^s$ is the $3M$ dimensional array containing the components of the scattered field at the M measuring points. $\mathbf{G}_2$ is a matrix $3M \times 3N$ depending on the wave number, cell size, cell location and the location of the measuring points.

Using the equivalent current modeling, which was discussed in the previous chapter, the scattered field at the measuring points can be rewritten as:

$$[\mathbf{E}^s] = [\mathbf{G}_2][\mathbf{J}_{eq1}] \tag{5.9}$$

where,

$$[\mathbf{J}_{eq1}] = [\mathbf{O}][\mathbf{E}] \tag{5.10}$$

In equation (5.9) $\mathbf{J}_{eq1}$ is a $3N$ dimensional array whose elements are the unknown components of the equivalent current density inside the N discretization subvolumes of the body.

5.3 Reconstruction Procedure:

The reconstruction procedure usually starts by solving the forward problem so as to obtain the scattered field at the measuring points, which simulate the measured field. The values of the incident field are calculated at the center of each subvolume or cell. This is followed by the calculation of the Green's function matrix $\mathbf{G}_1$. Assuming that the permittivity distribution of the body is known and thus the matrix $\mathbf{O}$, the total field $\mathbf{E}$ at each subvolume is calculated using (5.7) as follows:

$$[\mathbf{E}] = \left([\mathbf{I}] - [\mathbf{G}_1][\mathbf{O}]\right)^{-1}[\mathbf{E}^i] \tag{5.11}$$

The elements of the $3M \times 3N$ matrix $\mathbf{G}_2$, which relates the subvolumes to the measuring points, are then calculated. The scattered field at the measuring points is then calculated using (5.8).

In order to solve the inverse problem we have to use the equivalent current modeling. Knowing the scattered field $\mathbf{E}^s$, the equivalent current $\mathbf{J}_{eq1}$ is calculated using (5.9). This involves the calculation of the inverse of the matrix $\mathbf{G}_2$.

This matrix $\mathbf{G}_2$ is not necessarily square matrix depending on the number of measuring points. For the three-dimensional case and because of the field components, if the body is divided into N subvolumes, these requires the use of $3N$ measuring points or detectors so as to have a square Green's function matrix $\mathbf{G}_2$. Doing this increases the computation time. If this was the only problem with the matrix $\mathbf{G}_2$, it may be solved using special techniques for handling rectangular systems. Yet, this is not the case, as the matrix $\mathbf{G}_2$ is highly ill-conditioned even when it is square and thus the system described in (5.9) is ill-posed. So regularization techniques have been applied to obtain a well behaved, reasonable approximation of this ill-posed problem. The most widely used regularization techniques are the psuedoinverse transformation [82] and the Tikhonov regularization [92]. The latter is widely used by several researchers as has been shown in the previous chapter. These techniques usually require the availability of a priori information.

Assuming the process of regularization is successful, we proceed by calculating the diagonal elements of the object matrix $\mathbf{O}$. This is done using (5.10), by dividing the corresponding elements of the total field vector and the equivalent current vector. For the three-dimensional case and because of the presence of three field and current

components, we obtain three sets of contrast, corresponding to the x, y and z components, respectively. So averaging is used to obtain a single value for the contrast and thus the complex permittivity distribution.

Any proposed technique or method for the reconstruction of the complex dielectric permittivity should be tested first in the absence of noise. The next step is to add noise to the scattered field calculated by solving the forward problem. This is done to simulate measured data uncertainties. For a well-posed system, this wouldn't have been a problem, but being ill-posed and thus unstable regarding noise complicates the problem even more. Most of the published results require the use of multi-illumination techniques added to the use of a regularization procedure. Although this increases the computation time, it helps decreasing the ill-posedness of the system, aiming to obtain an acceptable reconstruction.

5.4 The Unrelated Illumination:

The unrelated illumination method, like most of the spatial domain methods, utilizes the method of moments (MoM) to discretize the nonlinear integral equation, which relates the scattered field data and the complex dielectric permittivity. Yet, it differs from other previous spatial methods in that the way of acquiring information helps overcoming the ill-posedness nature of the problem. This is done simply by redefining the problem, aiming to solve a well-posed system and hence eliminating the need to use special regularization techniques. The unrelated illumination method has been tested before with two-dimensional bodies [107], [108] and is extended here to handle three-dimensional inhomogeneous lossy and lossless dielectric bodies.

In this method, the body under investigation is illuminated with a group of unrelated incident fields. This is maintained by the proper arrangement of the polarization and the direction of these incident electric fields. Using this method, the scattered field measured at one point is sufficient to reconstruct the dielectric permittivity distribution of the body. Yet, for a body divided into N subvolumes, the method requires the use of $3N$ unrelated incident fields. This guarantees that the matrix formed of these incident fields is well-conditioned and thus invertible.

5.4.1 Mathematical Formulation:

Consider an inhomogeneous dielectric body of arbitrary shape that is characterized by a dielectric constant $\varepsilon_r(r)$ and an electric conductivity $\sigma(r)$, both generally variable from point to point. If the body is illuminated in free space by an incident wave with electric field $\mathbf{E}^i$ and using the method of moments, the total field at each subvolume and the scattered field at the measuring points were derived earlier in this chapter:

$$[\mathbf{E}^i] = ([\mathbf{I}] - [\mathbf{G}_1][\mathbf{O}])[\mathbf{E}] \tag{5.7}$$

$$[\mathbf{E}^s] = [\mathbf{G}_2][\mathbf{O}][\mathbf{E}] \tag{5.8}$$

The matrix $([\mathbf{I}] - [\mathbf{G}_1][\mathbf{O}])$ is always well-posed, thus knowing the incident field we can solve the forward problem and obtain the scattered field at the measuring points. On the other hand the matrix $\mathbf{G}_2$ is highly ill-conditioned especially when a large dielectric body is involved. Thus, as mentioned earlier trying to solve the system by computing its inverse renders the system ill-posed and forces the use of regularization techniques.

Usually $\mathbf{E}^i$ is a $3N \times 1$ vector containing the $\mathbf{E}_x$ components of the field at all N subvolumes, followed by the $\mathbf{E}_y$ components and the last N elements are the $\mathbf{E}_z$ components. By using a $3N$ unrelated incident fields, which is the key of the unrelated illumination method, $\mathbf{E}^i$ is a $3N \times 3N$ matrix. This differs from the multi-illumination technique used in other reconstruction methods in that it puts a constraint on the number of views, that it must be $3N$. Also, the incident fields used should be linearly independent or unrelated, thus allowing the inversion of the $3N \times 3N$ incident matrix. To obtain these $3N$ unrelated incident fields two planar phased array antennas are used, one in the xy plane and one in the xz plane as shown in Fig. 5.1. By adjusting the polarization of the array elements we can obtain a diagonally dominant incident matrix.

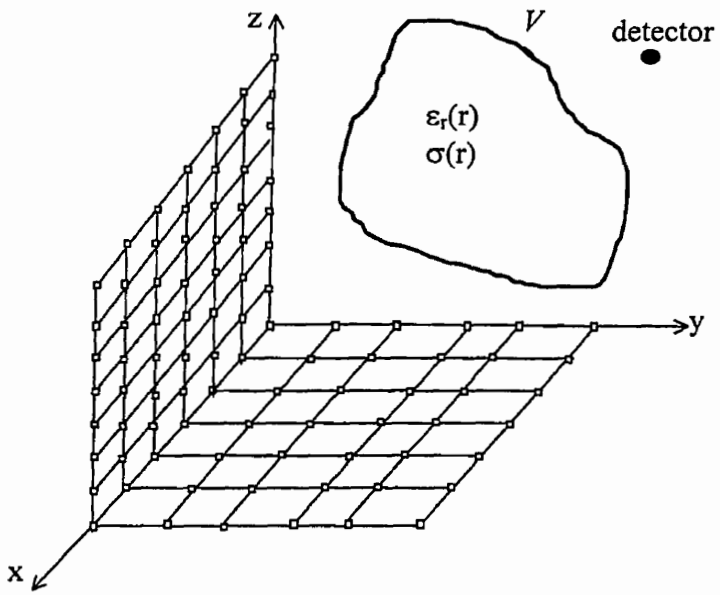

Fig. 5.1 An arbitrary shaped body illuminated by a group of unrelated incident fields from two planer phased arrays.

Writing equation (5.7) in the form:

$$[\mathbf{E}] = -([\mathbf{G}_1][\mathbf{O}] - [\mathbf{I}])^{-1}[\mathbf{E}^i] \tag{5.12}$$

and substituting (5.12) into (5.8) and taking into consideration that $\mathbf{E}^s$ is not a $3M$ array any more, it is now $3M \times 3N$ matrix corresponding to the $3N$ incident fields:

$$[\mathbf{G}_2][\mathbf{O}]([\mathbf{G}_1][\mathbf{O}] - [\mathbf{I}])^{-1}[\mathbf{E}^i] = -[\mathbf{E}^s] \tag{5.13}$$

Making use of the fact that the incident matrix is well conditioned and thus invertible, the matrices in (5.13) can be rearranged as follows:

$$([\mathbf{E}^s][\mathbf{E}^i]^{-1}[\mathbf{G}_1] + [\mathbf{G}_2])[\mathbf{O}] = [\mathbf{E}^s][\mathbf{E}^i]^{-1} \tag{5.14}$$

where the only unknown is the object or contrast matrix **O**. As shown by equation (5.14) the only matrix that needs to be inverted is the incident matrix. Then using simple vector and matrix operations we can obtain the object function of each cell.

For simplicity we can denote:

$$[\Psi] = [\mathbf{E}^s][\mathbf{E}^i]^{-1}[\mathbf{G}_1] + [\mathbf{G}_2] \tag{5.15}$$

and

$$[\Phi] = [\mathbf{E}^s][\mathbf{E}^i]^{-1} \tag{5.16}$$

Equation (5.14) can be written in a simplified form as:

$$[\Psi][\mathbf{O}] = [\Phi] \tag{5.17}$$

and the elements of the diagonal matrix **O** are obtained by comparing the corresponding elements at any row of [Ψ] and [Φ]. As m changes from 1 to $3M$, where M is the number of measuring points, the object function or the contrast of the n^{th} cell is given by:

$$O_{nn} = \Phi_{mn} / \Psi_{mn} \tag{5. 18}$$

By doing so we obtain $3M$ values of the object function of the n^{th} cell O_{nn}, thus averaging is used to obtain a single value of O_{nn}. Then using (4.18) we can obtain the permittivity and conductivity of each cell as follows:

$$\varepsilon_r(n) = \mathrm{Re}\left[O_{nn} / k_o^2 \right] + 1 \tag{5. 19}$$

$$\sigma(n) = -\mathrm{Im}\left[O_{nn} / k_o^2 \right] \times \omega \varepsilon_o \tag{5. 20}$$

In conclusion, for the unrelated illumination method, the body under investigation is illuminated by a group of unrelated incident fields. The method of moments is applied to discretize the problem. The forward scattering problem is solved via a technique similar to that applied by all other techniques. The only difference is that the total field is a matrix not a vector and so is the scattered field at the measuring points. Knowing the scattered field and making use of the fact that the incident matrix is invertible, we use simple vector and matrix operations to arrive at a system that can be solved easily to obtain the required object function matrix. In doing so, we eliminate the need to calculate the inverse of a highly ill-conditioned matrix and also eliminate the use of the equivalent current modeling procedure that is applied by all spatial domain techniques. Fig. 5.2

summarizes the steps used in the reconstruction process in the unrelated illumination method.

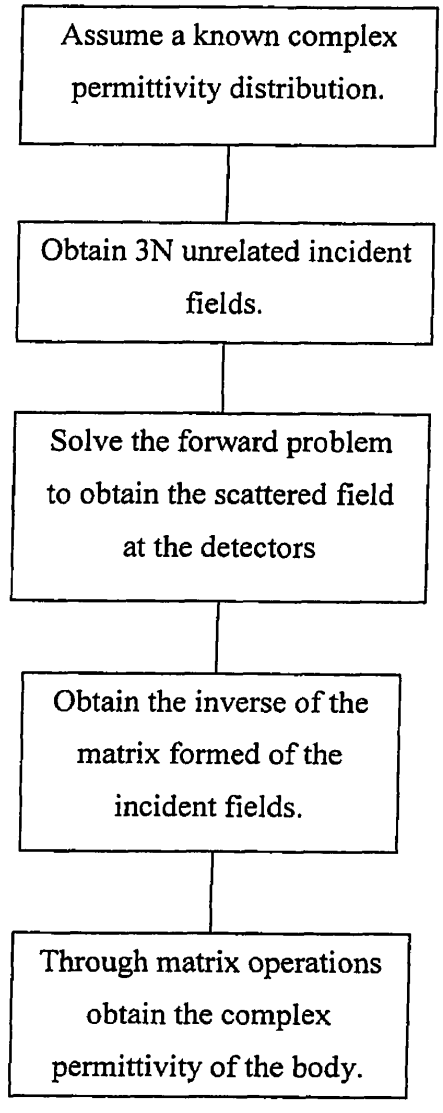

Fig. 5.2 Steps used in the reconstruction process.

5.5 Numerical Simulations and Results:

In the previous section, the unrelated illumination method was presented as a tool for the reconstruction of the complex dielectric permittivity of three-dimensional bodies. In this section, results of the numerical simulations that were carried out are presented and discussed. The aim of these simulations is to assess the capabilities of the method and to test its robustness in the presence of measured data uncertainties. Various three-dimensional dielectric bodies have been used including a simple cube, a model of the human body and a model of the head.

All the numerical simulations have been carried out using only one measuring point. Yet, because of the three-dimensional nature of the problem under consideration, one measuring point yields three measured values of the diagonal elements of **O** corresponding to the three components of the scattered field. Averaging is used to obtain a single value of the object function and hence the permittivity and conductivity. The values of the scattered electric field at the measuring point is obtained via a computer program that can determine the direct scattering from three-dimensional inhomogeneous dielectric bodies. For all simulations two planar phased arrays (Fig. 5.1) are used to illuminate the body with a group of unrelated incident fields. The number of elements and the spacing between them are varied according to the dielectric body under consideration.

The relative mean square error formulae are used to measure the error in the relative dielectric permittivity, conductivity and object function in all simulations:

$$\delta\varepsilon_r = \frac{\left[\sum_{n=1}^{N}\left(\varepsilon_{rn} - \varepsilon_{rn}^{'}\right)^2\right]^{1/2}}{\left[\sum_{n=1}^{N}\varepsilon_{rn}^2\right]^{1/2}} \tag{5.21}$$

$$\delta\sigma = \frac{\left[\sum_{n=1}^{N}\left(\sigma_n - \sigma_n^{'}\right)^2\right]^{1/2}}{\left[\sum_{n=1}^{N}\sigma_n^2\right]^{1/2}} \tag{5.22}$$

$$\delta O = \frac{\left[\sum_{n=1}^{N}\left(O_n - O_n^{'}\right)^2\right]^{1/2}}{\left[\sum_{n=1}^{N}O_n^2\right]^{1/2}} \tag{5.23}$$

where ε_{rn}, σ_n and O_n are the original relative dielectric permittivity, conductivity and object function of the n^{th} subvolume, respectively. $\varepsilon_{rn}^{'}$, $\sigma_n^{'}$ and $O_n^{'}$ are the reconstructed relative dielectric permittivity, conductivity and object function of the n^{th} subvolume, respectively. Because the error obtained with these formulae is the average error, in some of the simulations, the normalized error in every cell in the volume under consideration is plotted:

$$\delta\varepsilon_{rn} = \frac{\left(\varepsilon_{rn} - \varepsilon_{rn}^{'}\right)}{\varepsilon_{rn}}$$

$$\delta\sigma_n = \frac{\left(\sigma_n - \sigma_n^{'}\right)}{\sigma_n} \tag{5.24}$$

$$\delta O_n = \frac{\left(O_n - O_n^{'}\right)}{O_n}$$

In the absence of noise and irrespective of the permittivity distribution within the dielectric body, the error is found to be negligible, giving almost perfect reconstruction. In order to study the effect of measured data uncertainties on the reconstruction process, we added to the scattered field at the detector a random noise complex array **n**. The real and imaginary parts of this array are constituted by two independent sequences of random variables. These sequences have zero mean and a variance that can be varied to obtain different signal to noise (*S/N*) ratios:

$$S/N = 10\log \left\| \mathbf{E}^s \right\|^2 \Big/ \left\| \mathbf{n} \right\|^2 \tag{5.25}$$

5.5.1 Effect of varying the cell size:

In this simulation we attempt to study the effect of varying the cell size and hence the descritization on the accuracy of the reconstruction. The body under consideration is a $40 \times 40 \times 40\, cm$ body. The operating frequency is $900 MHz$. The body is divided into 8 cubic cells with $\varepsilon_r = 8$. The computer simulation is carried out, the body is then divided into 64 equal cubic cells of the same dielectric permittivity. Fig. 5.3 shows the error in the dielectric permittivity in both cases. As shown the smaller the cell size, the less the error and the better the reconstruction for the same S/N ratio.

A layer in the 8cell cube

S/N=25

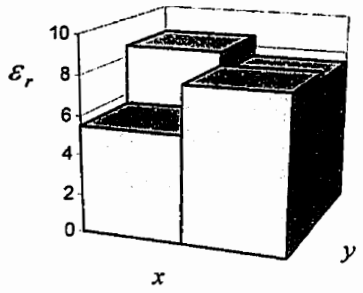

Equivalent layers in the 64cell cube

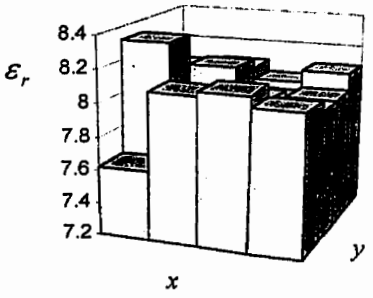

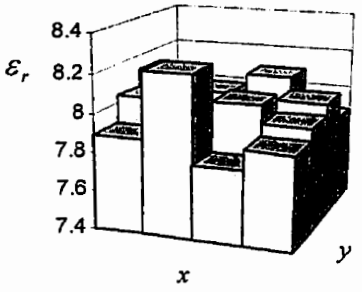

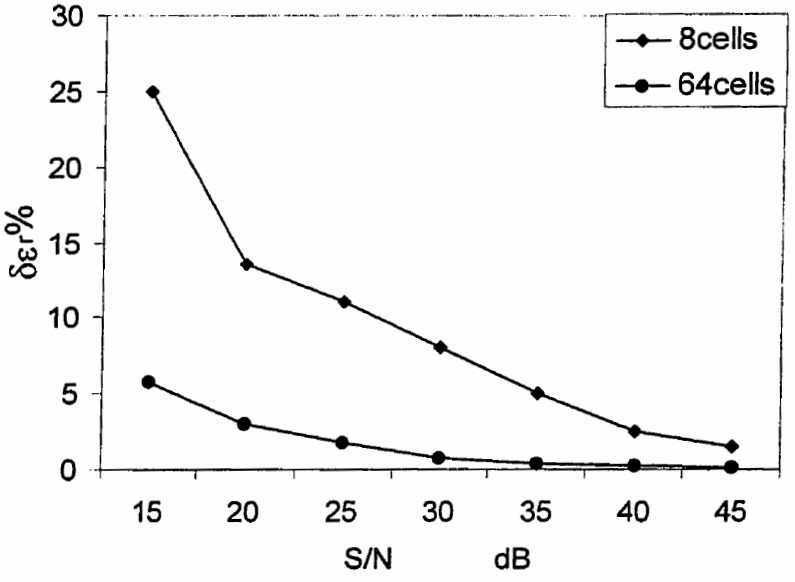

Fig. 5.3 Percentage error versus S/N ratio for cell sizes 10, 20 cm.

5.5.2 Effect of varying the strength of the scatterers:

Reconstruction procedures are highly sensitive to the strength of the scatterer under investigation. In this simulation, two scattering bodies are investigated, the first body has $\varepsilon_r = 8$ and the second has $\varepsilon_r = 32$. The simulation is carried out for the $40 \times 40 \times 40\,cm$ cube, which is divided into 64 equal cubic cells at $900MHz$. Fig. 5.4 shows the error in the reconstruction of the dielectric permittivity for these scattering strengths. At a S/N ratio of 25dB, the error for the cube whose $\varepsilon_r = 32$ is almost 9% while the error in the case when $\varepsilon_r = 8$ is almost 2%. So the reconstruction is better for weaker scatterers, yet, the 9% error at S/N ratio of 25dB is still acceptable.

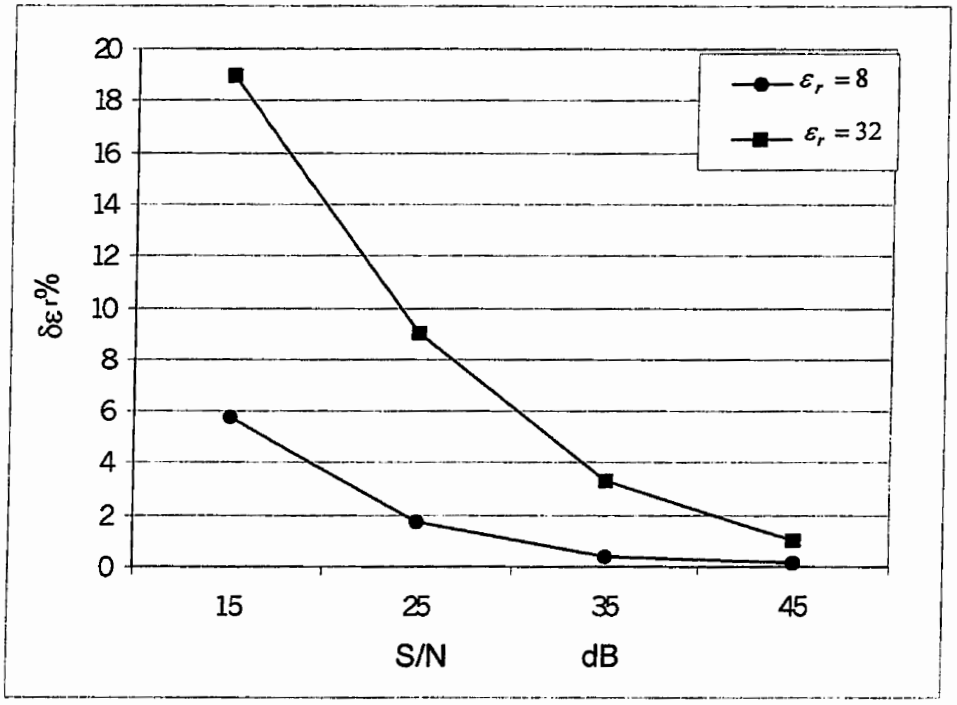

Fig. 5.4 Percentage error versus S/N ratio for different scattering strength.

5.5.3 Effect of changing the contrast:

In this simulation we attempt to study the effect of varying the contrast on the reconstruction of the dielectric permittivity. The $40 \times 40 \times 40\,cm$ cube is divided into 64 cells each of dielectric permittivity $\varepsilon_r = 1$, except for 8 cells in the core of the cube that have a dielectric permittivity $\varepsilon_r = 3$. For the next simulation, the eight cells in the core are given a permittivity $\varepsilon_r = 32$ thus increasing the contrast between the core and the surrounding cells. As shown in Fig. 5.5, the effect of the change in the contrast on the reconstruction of the permittivity distribution is minimal, still the reconstruction is slightly better for the low contrast body.

The next simulation, the $40 \times 40 \times 40\,cm$ cube is divided into 64 cells each of dielectric permittivity $\varepsilon_r = 3$, except for 8 cells in the core of the cube that have a dielectric permittivity $\varepsilon_r = 1$. For the next simulation, all the cells except the core are given a permittivity $\varepsilon_r = 32$ thus increasing the contrast between the core and the surrounding cells. As shown in Fig. 5.6, the effect of the change in the contrast on the reconstruction of the permittivity distribution in this case, which is the opposite of the case shown in Fig. 5.5, can not be ignored.

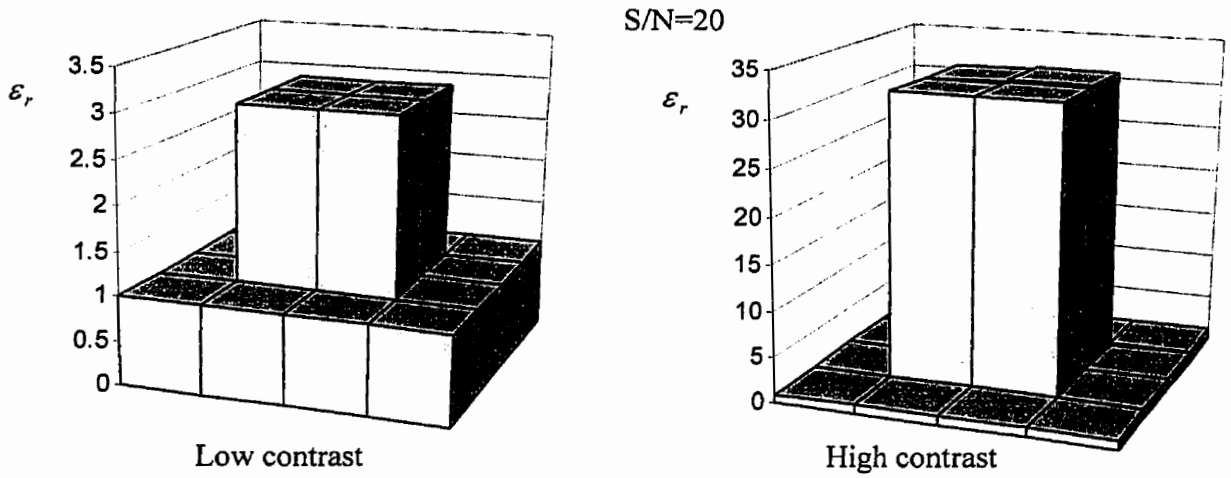

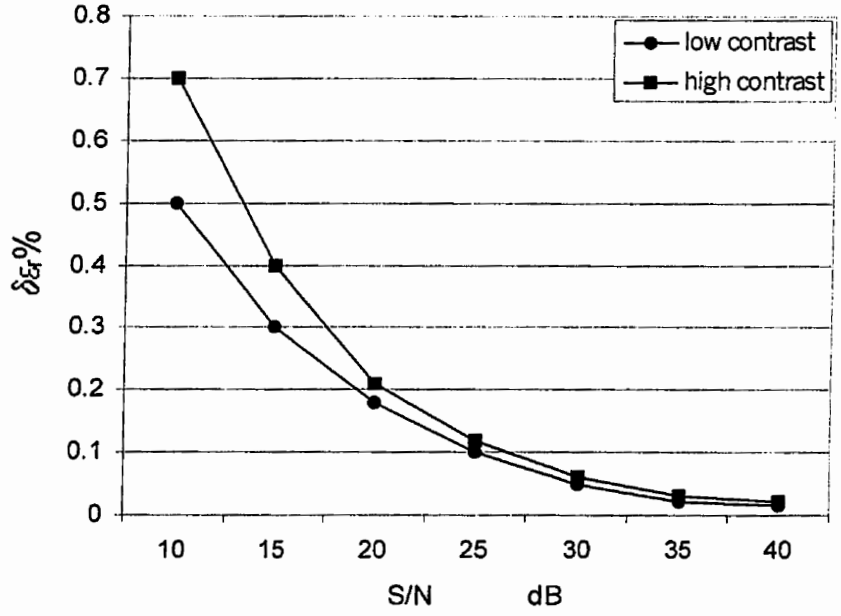

Fig. 5.5 Percentage error versus S/N ratio for different contrasts.

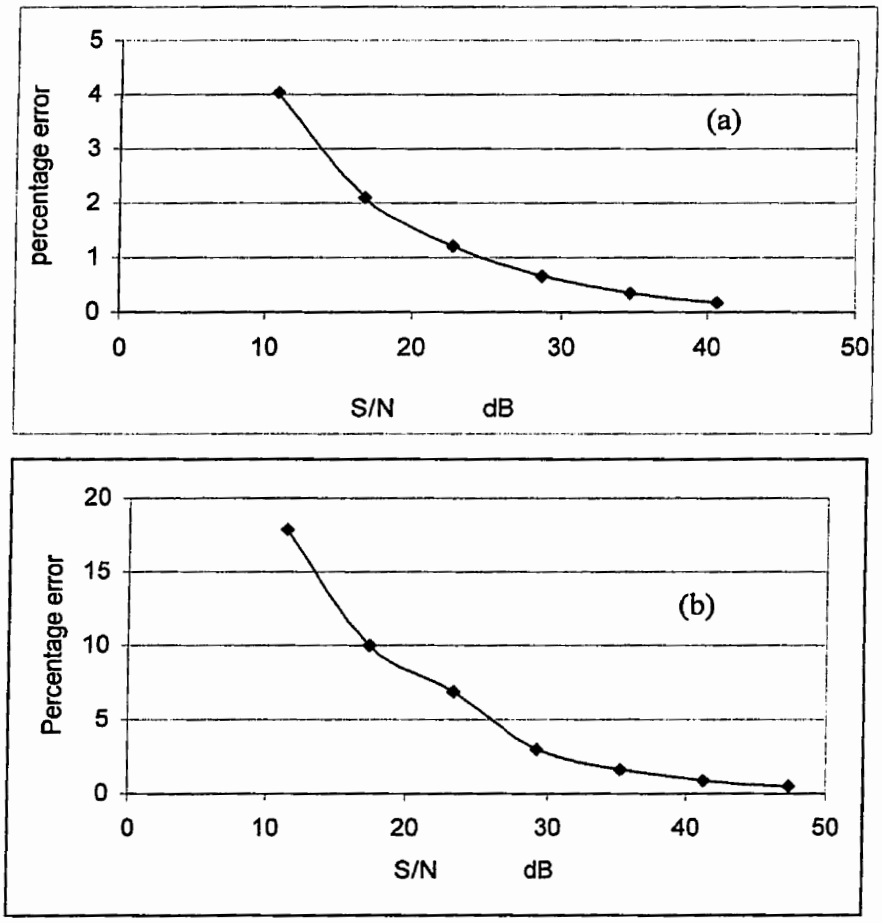

Fig. 5.6 Percentage error versus S/N ratio for outer cells of dielectric permittivity (a) $\varepsilon_r = 3$ and (b) $\varepsilon_r = 32$.

5.5.4 Effect of changing the number of scatterers:

Another issue to investigate is the effect of the number of scatterers within the body. It should follow from the previous simulations, that if the reconstruction is better for weaker scatterers and lower contrast, then it should be better for fewer number of scatterers. To check this the $40 \times 40 \times 40\,cm$ cube is divided into 64 cells. The case of 8 scatterers imbedded in the core of the cube is compared to when all of the 64 cells forming the cube are scatterers. The scatterers have a permittivity $\varepsilon_r = 3$. Fig. 5.7 shows the error in the reconstruction for both cases. As predicted, the error is less for the fewer number of scatterers. Yet, as shown at S/N ratio of 25dB, the error for the 64 scatterers case is only 1.1%.

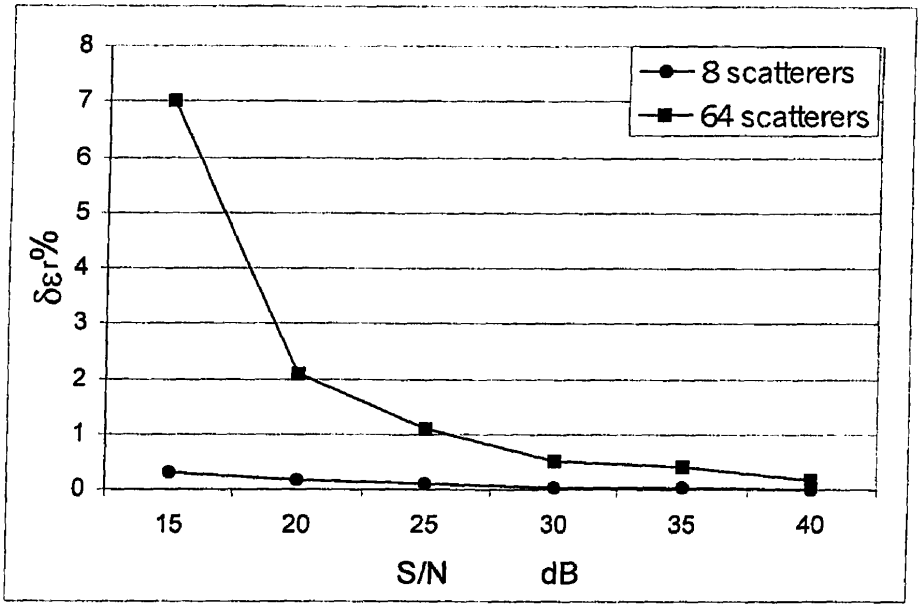

Fig. 5.7 Percentage error versus S/N ratio for different number of scatterers.

In all of the previous simulations, we have investigated lossless dielectric bodies. In the following simulations we are going to study lossy dielectric bodies of variable cell size and geometric complexity.

5.5.5 Reconstruction of a simplified human body model:

This simulation involves the use of a 180 cubic cell human body [109]. Fig. 5.8 shows the model. This model is characterised by a variable cell size together with the fact that the average values for the conductivity and dielectric permittivity for the different kinds of tissue have been used in certain cells.

The simulation is carried out at $300MHz$ as the model data is only available at this frequency. The cell size varies from $10cm$ to $1cm$ through out the model. The cell number, volume, relative location and the dielectric properties for this model are given in Appendex C. For some of the cells of size $10cm$ and $\varepsilon_r \approx 80$, which is the worst case electrical cell size, the method of moments requirements for discretization are violated. Fig. 5.9 shows the percentage mean square error in the reconstruction of the relative dielectric permittivity, conductivity and object function. As shown the error in the reconstruction of the conductivity is higher than that of the permittivity, yet, it is still acceptable at higher levels of noise. Fig. 5.10 shows the error in the reconstruction of the relative dielectric permittivity and conductivity at every cell in the body.

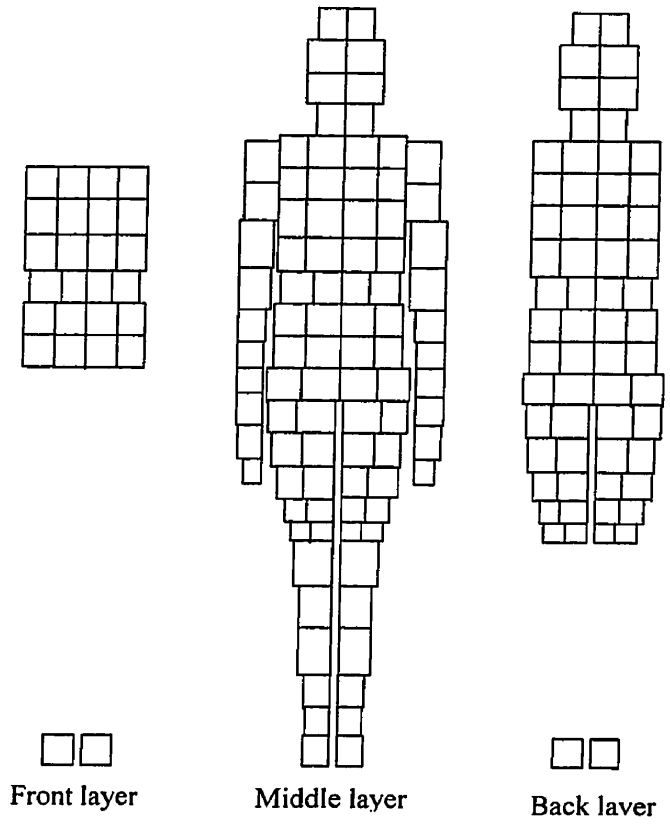

Fig. 5.8 Three layers constituting the 180-cell human body model.

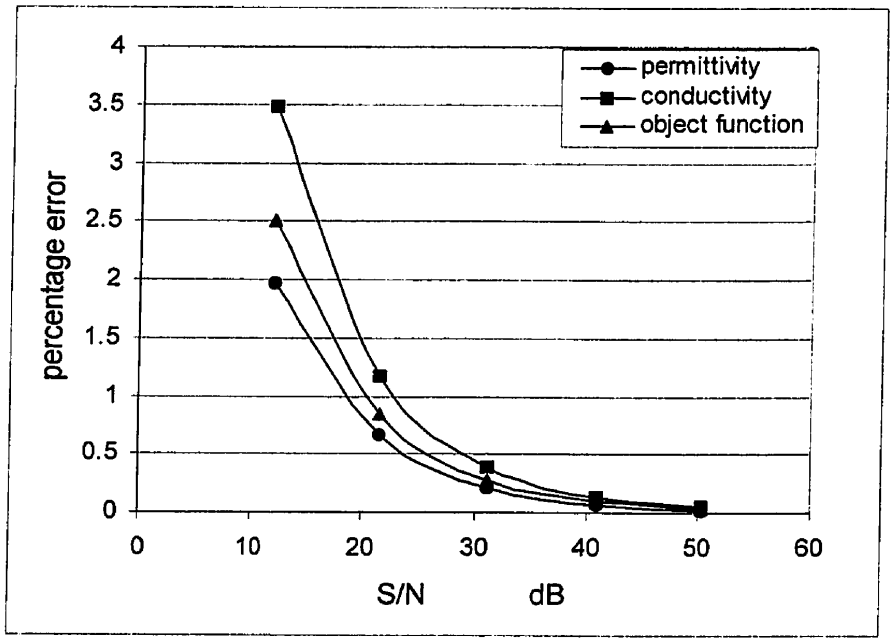

Fig.5.9 Reconstruction error in the human body model.

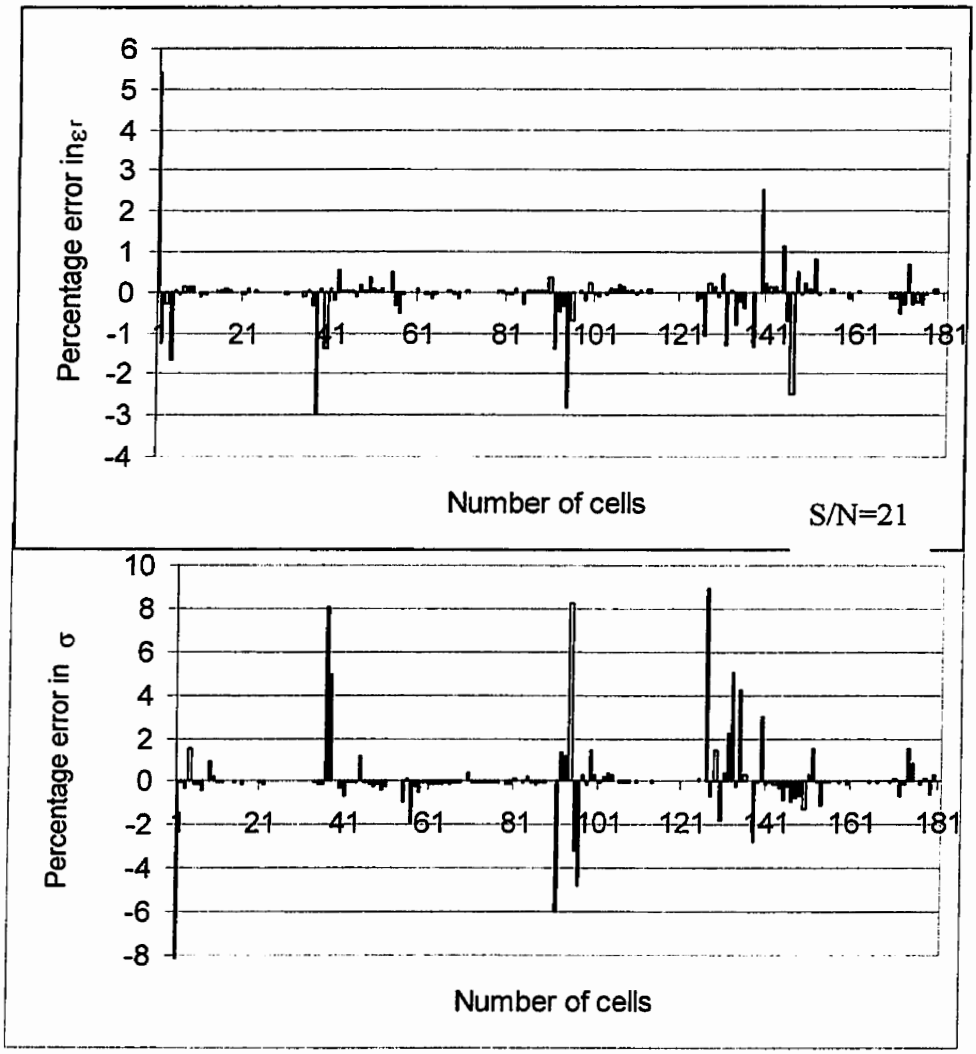

Fig.5.10 Reconstruction error in every cell of the human body model.

5.5.6 Reconstruction of a simplified head model:

In this simulation, the body under investigation is a simplified model of a human head. It is formed of 209 cells arranged in five layers and formed of four types of tissue: skin, bone, brain and eye (Fig. 3.11). The cell size is $2\times2\times2$ *cm*. The model is an

example of a geometrically irregular and inhomogeneous dielectric body. The values of the dielectric permittivity and conductivity for the tissue involved at 300*MHz* and 900*MHz* are given in table 5.1. These values have been obtained using the second order Debye dielectric equation given in Chapter 3. The parameters used in the equation are those given in Table 3.1. The simulation is carried out at 900*MHz* and the percentage mean square error in the reconstruction of the object function, dielectric permittivity and conductivity is shown in Fig.5.11. Fig. 5.12 shows the error in the reconstruction of the relative dielectric permittivity and conductivity at every cell in the simplified head model. From Fig. 5.12 it is clear that although the average error in the reconstruction of the dielectric properties for all cells is low (Fig. 5.11), at some cells the error is much higher.

Table 5.1 Dielectric properties of human tissue.

	300*MHz*		**900*MHz***	
Tissue	**Permittivity**	**Conductivity**	**Permittivity**	**Conductivity**
Bone	6.82205	0.0682344	6.13111	0.0871317
skin	53.0764	0.727464	46.7887	0.897553
Brain	54.9296	0.449199	50.3136	0.575565
Eye	55.7202	0.454412	52.3747	0.543721

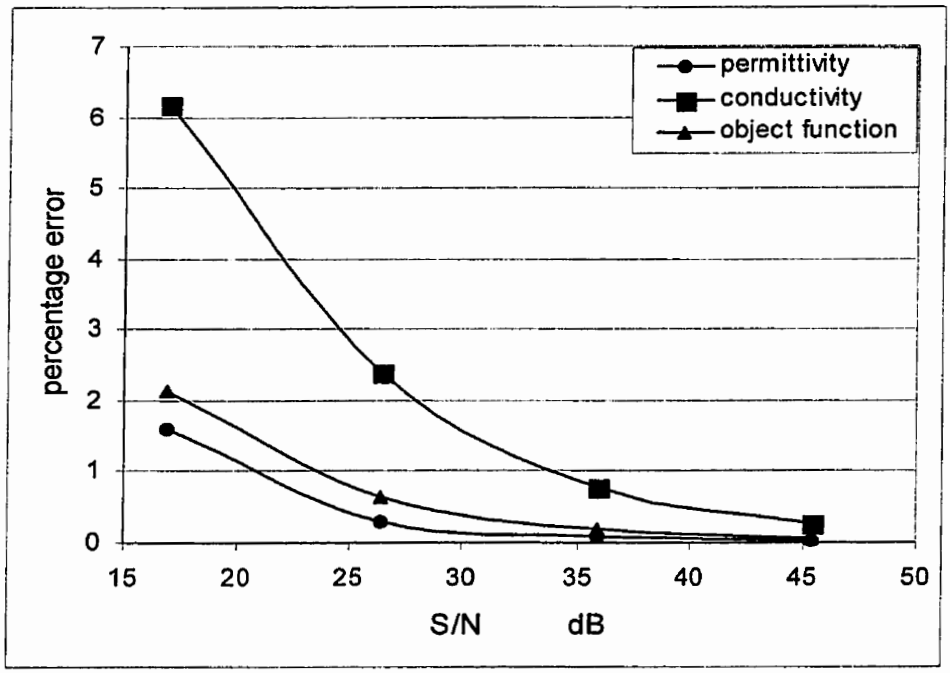

Fig. 5.11 Percentage error in the dielectric properties of the head.

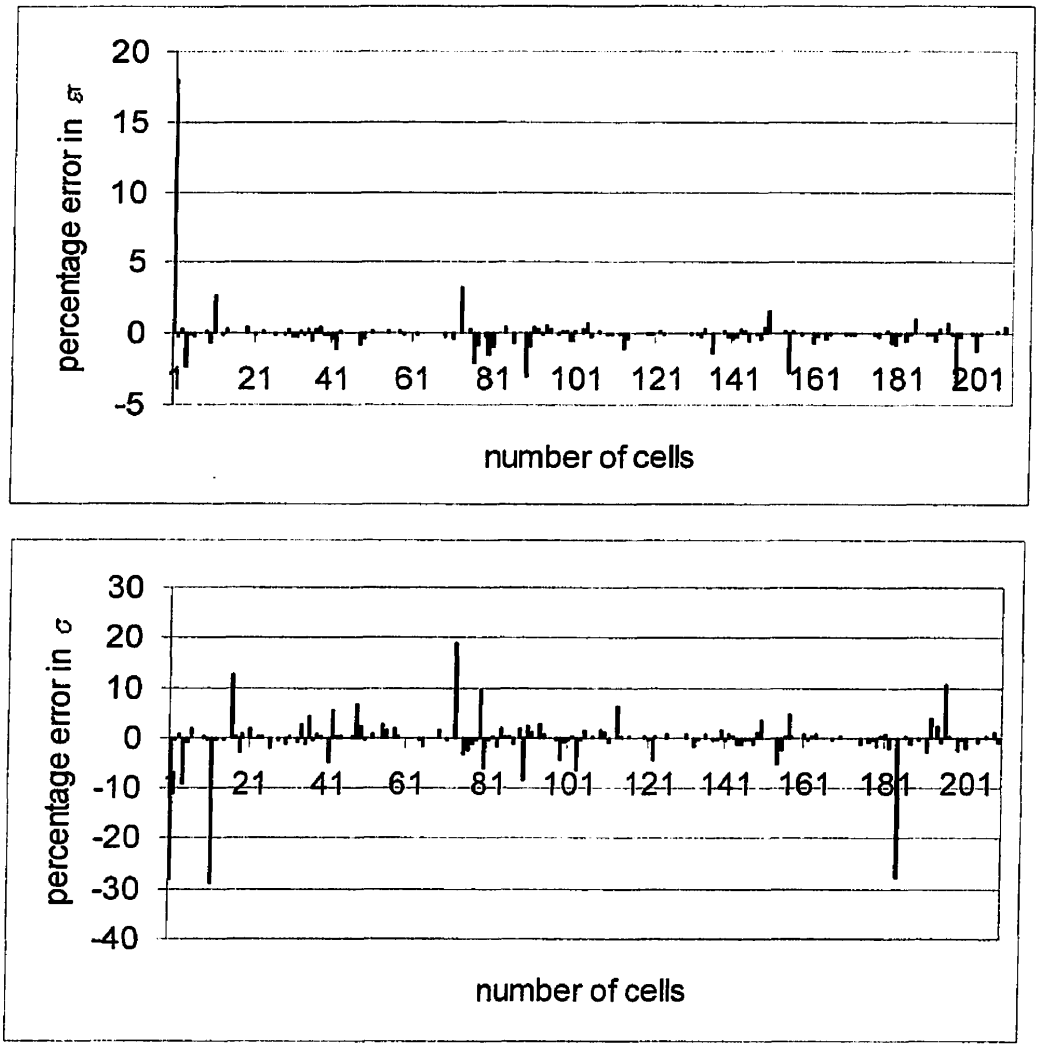

Fig.5.12 Reconstruction error in every cell of the head model at S/N=17.

5.5.7 Effect of varying the operating frequency:

These simulations involve the use of the same model of the head that was used in the previous section. The dielectric properties of the tissue used are kept constant for the three frequencies studied and correspond to those at 300*MHz*. This contradicts the

dispersive nature of biological tissue but is important for the sake of comparison. Three frequencies have been tried, $300MHz$, $900MHz$ and $3GHz$. A single detector at a fixed location has been used for all the simulations. Fig.5.13 shows the percentage relative mean square error in the object function. Fig. 5.14 and Fig. 5.15 show the percentage relative mean square errors in the relative dielectric permittivity and conductivity, respectively. As shown, the error in the reconstruction increases by increasing the frequency. The reason for this increase is that the incident matrix is not totally diagonally dominant. This is mainly because as the frequency increases, the physical size of the array decreases. This in turn decreases the effective aperture and hence the beam width of the incident ray. Thus, the incident field is not totally focussed on the required cell. Also, as the frequency increases, the physical size of the cells compared to the wave length of operation increases. This affects the performance of the method of moments especially at $3GHz$ when the size of the cell is 0.2λ. From the figures, for a typical signal to noise ratio (S/N) of 25, the reconstruction error is still acceptable for the three frequencies used.

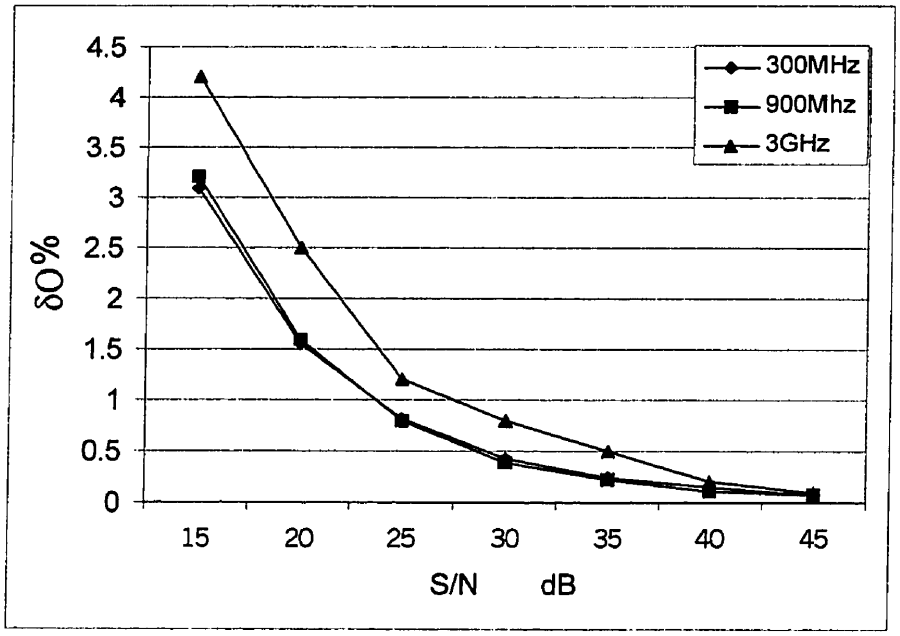

Fig. 5.13 Percentage relative mean square error in the object function *O*.

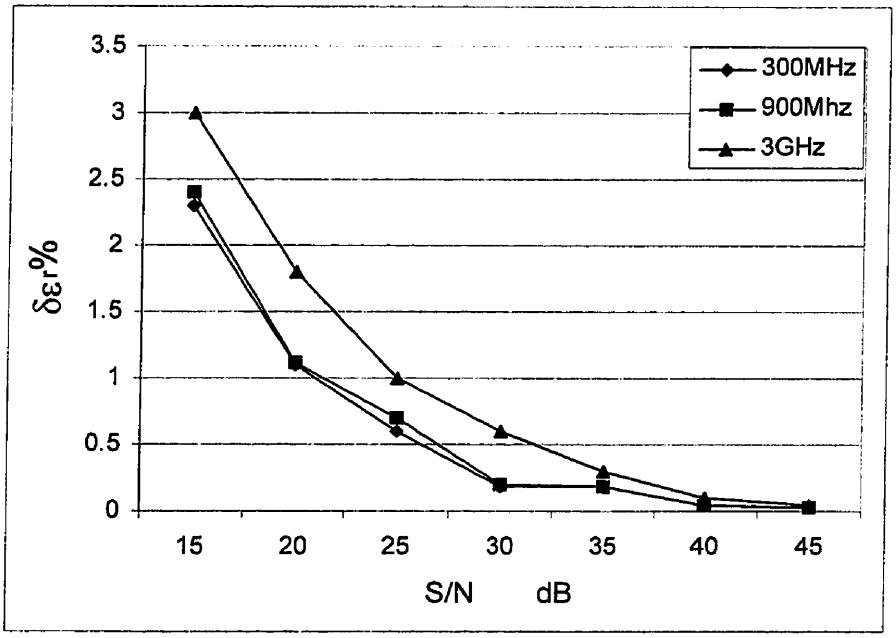

Fig. 5.14 Percentage relative mean square error in the relative permittivity.

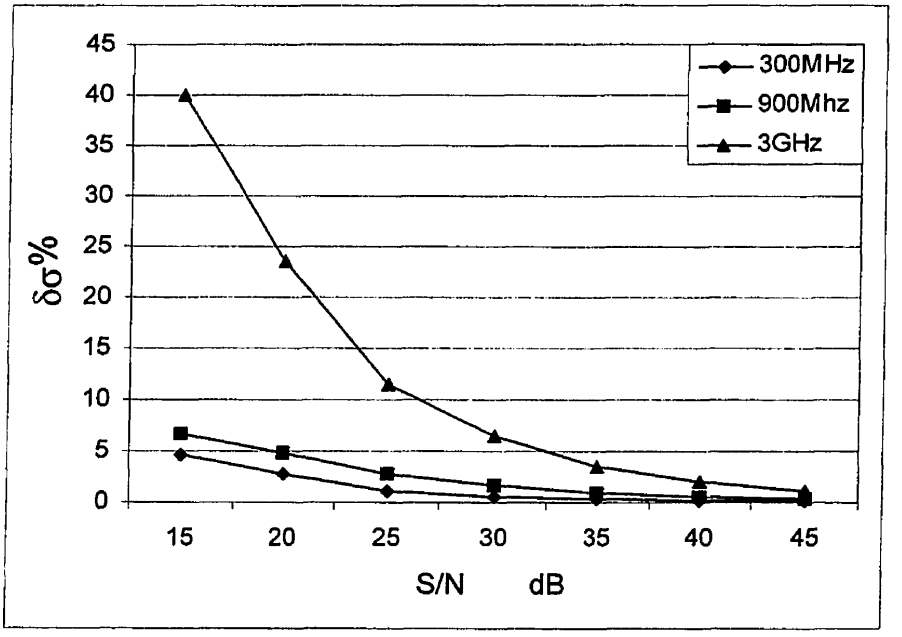

Fig. 5.15 Percentage relative mean square error in the conductivity.

5.5.8 Effect of varying the location of the detector:

All previous simulations, for a certain dielectric body, were carried out using one detector whose position has been kept constant. Acceptable error levels in the reconstruction of the dielectric properties have been obtained with only one detector in use. In this section, we attempt to study the effect of varying the detector location. The simulations that have been carried out show that the detector can be placed anywhere on the surface of sphere whose radius is at least one meter greater than that of a sphere containing the dielectric body which is the head model. Increasing the radius of the

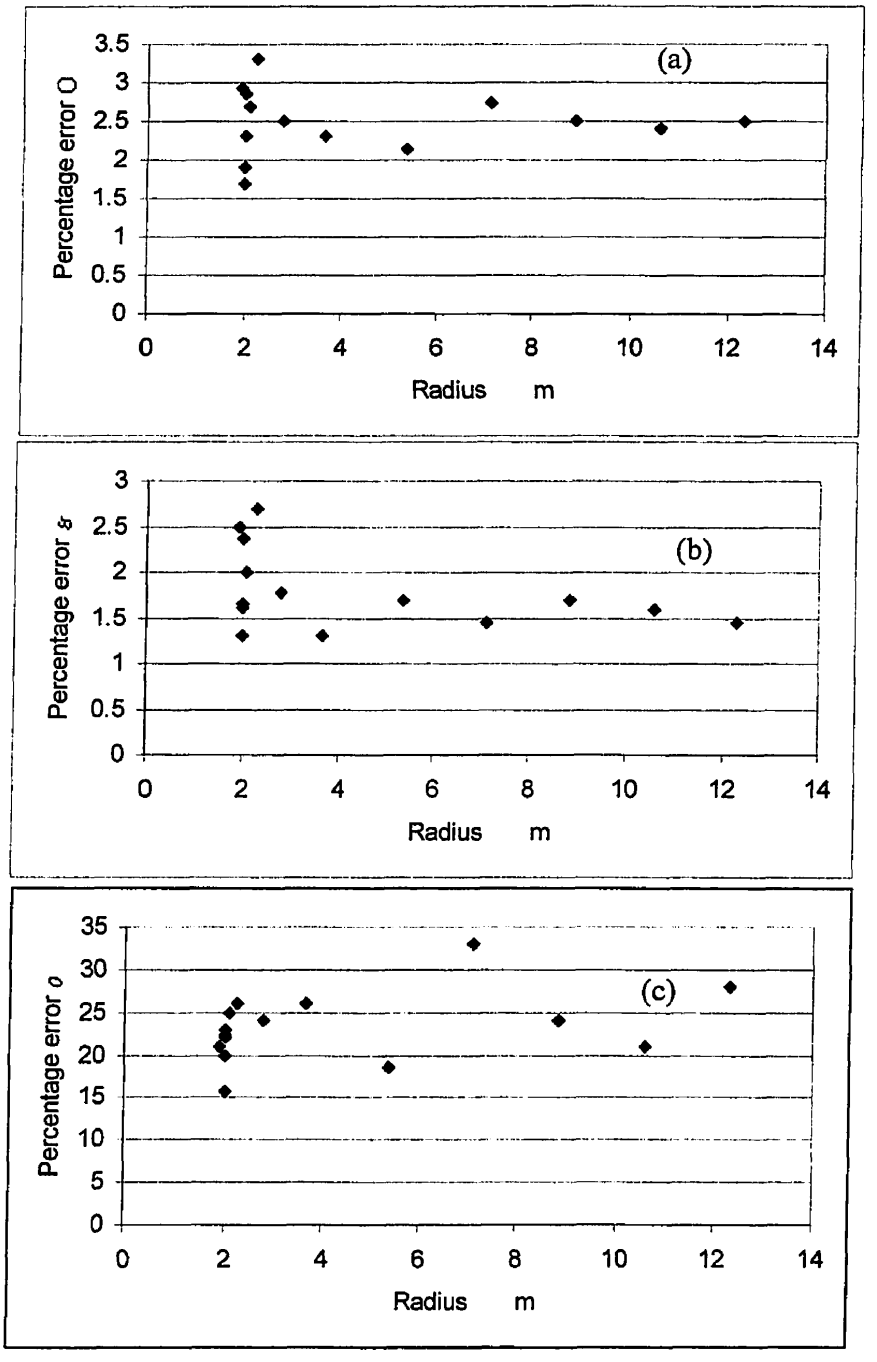

Fig. 5.16 Percentage relative mean square error in (a) object function, (b) dielectric permittivity and (c) conductivity for different locations of the detector.

spherical on which the detector is placed only presents minor fluctuations in the error level of the reconstruction of the dielectric parameters as shown in Fig. 5.16. As averaging is used to obtain a single value of the dielectric parameters, and because the error levels from different detectors are almost the same, using more than one detector does not guarantee better reconstruction. These conclusions are based solely on the simulations that were carried using the simplified head model

In the next simulation, we attempt to study whether the percentage error for a certain detector location is affected by frequency. Three different detector locations are tried, d, d/2 and 2d, where d=2m, at 300*MHz*, 900*Mhz* and 3*GHz*. As shown in Fig, 5.17, the fluctuations in the error levels make it unclear whether the effect of the detector location on the reconstruction error is influenced by the operating frequency. These conclusions are based solely on the simulations that were carried out using the simplified head model and for the specified three detector locations.

5.6 The planar phased array system:

As mentioned in the previous section, the required $3N$ unrelated incident fields are obtained by two planar phased arrays. Instead of using the arrays, a reflector antenna could have been used and mechanically steered to provide the required incident illumination. The arrays used are mainly selected to facilitate the numerical computations and to prove the numerical accuracy of the technique. The planar phased arrays have uniform amplitude and spacing. The orientation and polarization of the elements of the array, which are short dipoles, are varied to obtain the required components of the

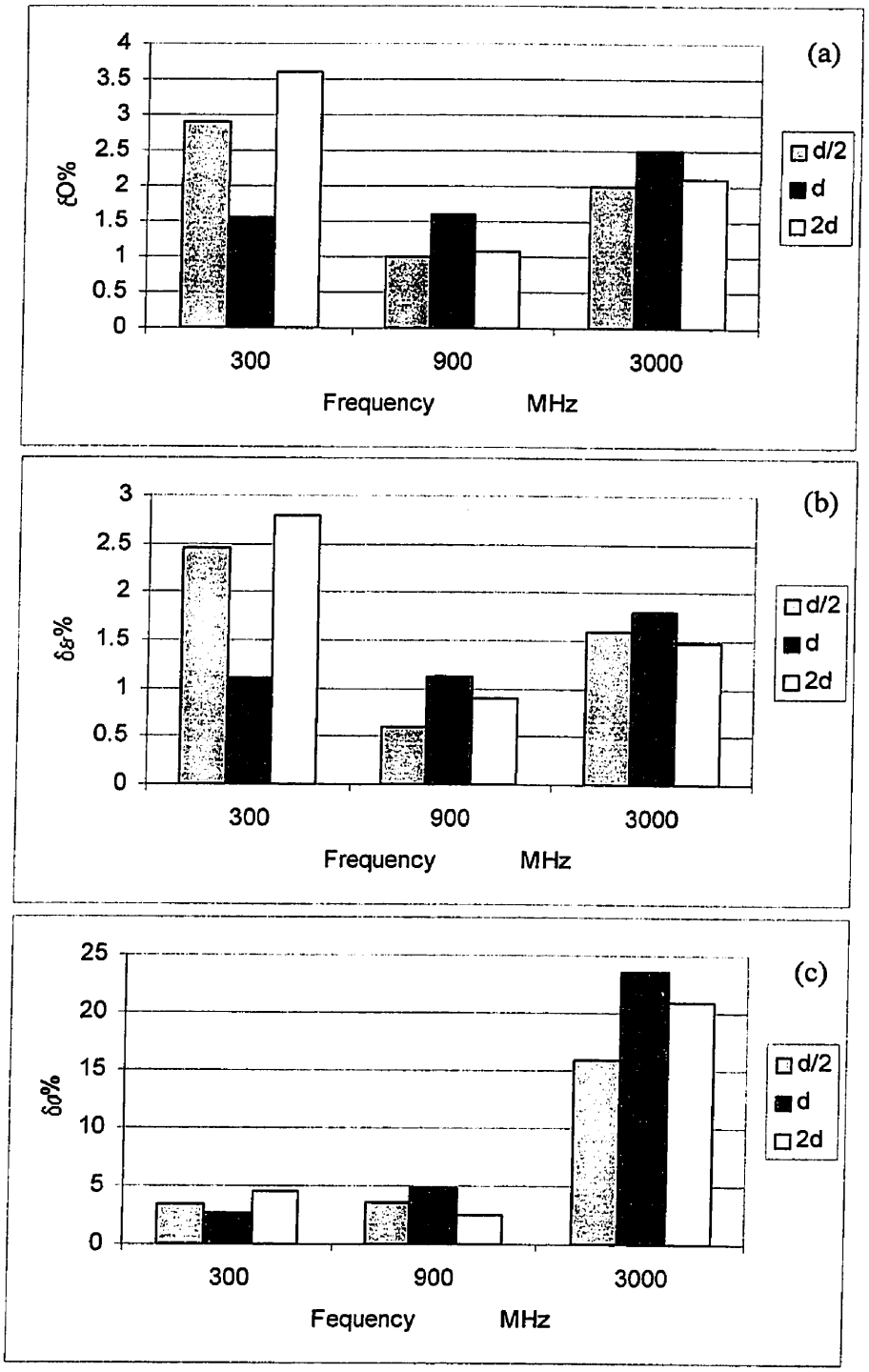

Fig. 5.17 Percentage relative mean square error in (a) object function, (b) dielectric permittivity and (c) conductivity for three detector locations S/N=20.

incident fields. The phase excitations between the elements are adjusted to aim the main radiation from the array to a certain subvolume within the body [115].

Most of the work was done initially at $300MHz$. Each planar array was 100×100 elements for the cube and 300×300 elements for the head model so as to have a small half power beam width (HPBW). The physical size of the array is large and can be a real hindrance when practical implementation is considered. Higher frequencies were then tried: $900MHz$ and $3GHz$, thus reducing the physical size of the array by two thirds and nine tenth, respectively. As shown in the previous section, acceptable reconstructions were obtained for both frequencies. This was done keeping the physical size and the discretization of the body under investigation constant. In other words, the numerical requirements of the simulation were not changed. For the $3GHz$ simulation and with cell size $2 \times 2 \times 2\,cm$ for the case of the head, this discretization is considered marginal for the method of moment optimal performance.

Numerous methods are available to decrease the physical size of the array for a given HPBW at a certain frequency. One of these methods is to mount the dipoles on a ground plane. By properly adjusting the height of the dipole above this ground plane (Fig. 5.18), the directivity of the dipole can be increased, hence achieving the required HPBW using a smaller array size and thus effectively reducing the size of the array.

The geometry and type of the array elements used determine the overall directivity and HPBW of a certain array as well as the size and weight of the overall array. The more directive the element is, the more directive the overall array will be. Yet, the choice of the element will probably dictate what type of feed network can be used. So another alternative, instead of using short dipoles, more directive elements could be used.

Microstrip antennas, for example, have a gain of approximately 6-8dB, as compared to less than 2dB for short dipoles. The size of the microstrip element itself is less than the corresponding dipole because of the presence of the dielectric substrate. Thus using microstrip antennas as array elements would reduce the overall size of the array. Added to this, microstrip antennas are easy to fabricate, inexpensive, and can be seamlessly incorporated with the appropriate feed networks. However, the microstrip feed network will suffer from substrate losses. These losses can be substantial especially at higher frequencies and for large feed networks. In this case amplifiers can be used to compensate for the dielectric losses.

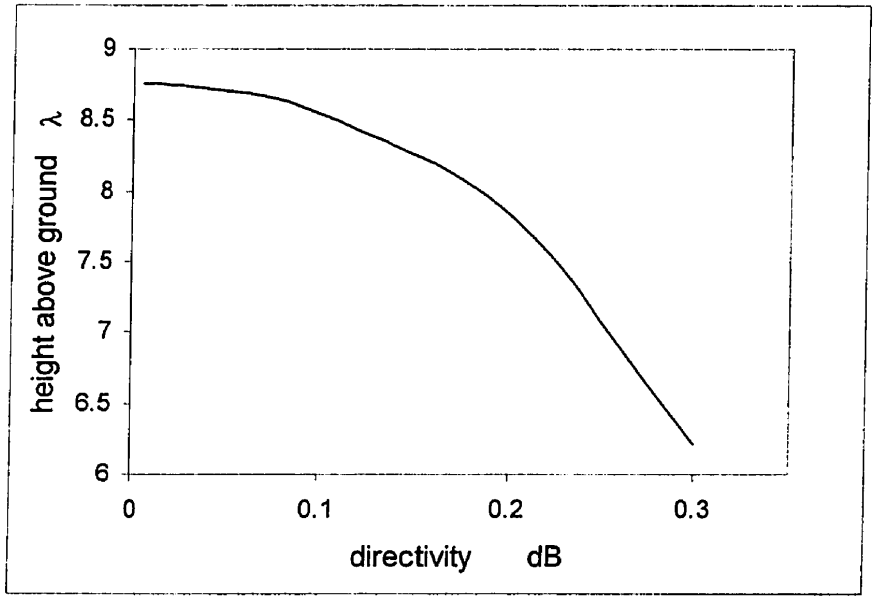

Fig. 5.18 Variation of the directivity with height from the ground plane for a horizontal short dipole. (directivity of the same dipole in free space is 1.78dB)

Another option is the use of superdirective arrays [116]-[117]. These arrays have directivities that are much larger than the directivity of an array of the same length and elements that is uniformaly excited. Superdirectivity applies in principle to both arrays of isotropic elements and to actual antenna arrays composed of nonisotropic elements such as dipoles [116]. A fixed aperture can achieve in theory any desired directivity value but the practical implications are not known. Superdirectivity is usually accomplished by inserting more elements within a fixed length thus decreasing the spacing between the elements. This eventually leads to rapid changes in the phase of the excitation coefficients of the array elements. In [117] two methods of achieving superdirectivity in uniform arrays of isotropic elements are presented. The first approach is achieved using alternating negative and positive phases with odd number of elements. In the second method, phases are adjusted to yield maximum directivity. The latter is achieved by applying an optimization technique.

5.7 Conclusion:

In this chapter we reviewed the basic reconstruction procedure employed by most of the spatial domain methods. The ill-posedness of the system in the inverse scattering problem was discussed and the necessity of using regularization techniques was pointed out. This was followed by a presentation of the unrelated illumination method and how it can be used to overcome the ill-posedness of the system. This was carried out by using a group of unrelated fields to illuminate the body, this guarantees that the incident matrix is invertible. Through some matrix operations and using the inverse of the incident fields matrix, the inverse problem is solved and the complex permittivity distribution at each

subvolume is obtained. It should be noted that the method does not put any constraints on the number of measuring points, in fact one measuring point provides sufficient data to reconstruct complex permittivity distribution of the body.

We then presented and discussed some of the numerical simulations that were carried out to assess the performance of the unrelated illumination method in the reconstruction of dielectric bodies. The scattered field at the measuring points or detectors was obtained via a computer program utilizing three-dimensional scattering from dielectric bodies. Measured data uncertainties were simulated by adding noise to the scattered field at the detectors. Several dielectric bodies, homogeneous, nonhomogeneous, lossless, lossy and geometrically complex bodies were reconstructed. The number of scatterers as well as the contrast have been varied and the accuracy of the reconstruction has been examined for each case. The effect of varying the operating frequency and the detector location on the error level of the reconstruction of the dielectric parameters have also been studied. The method has been proved to be robust and fairly accurate reconstruction technique.

CHAPTER 6

Conclusions

6.1 Conclusions:

In this thesis, we have attempted to study different aspects of interaction of electromagnetic waves with biological tissue. Two problems in particular were investigated. The first is three-dimensional scattering from biological tissue taking into consideration its dispersive nature. The other problem that was investigated is the three-dimensional reconstruction of the dielectric properties of a body from the scattered field data resulting from interrogation with electromagnetic waves. In the first problem forward scattering of electromagnetic waves was studied while in the latter both forward and inverse scattering of electromagnetic waves have been studied.

The specific absorption rate (SAR) is a measure of the amount of energy absorbed by the tissue as a result of irradiation by electromagnetic waves. This value is directly related to the various components of the field inside the body. The symmetric condensed node transmission line matrix method (SCN TLM) has been used to obtain the fields inside the body. Being a time domain method, it allows for obtaining the frequency

domain response over a wide frequency range via Fourier transformation and from a single run.

Second order Debye equation of the complex permittivity in the frequency domain has been used to simulate the dispersive nature of biological tissue in a modified TLM technique. In this technique the scattering matrix is independent of the dielectric properties of the medium, which are accounted for via lumped equivalent networks or sources connected to the nodes. These equivalent sources are calculated at each time step and included in the scattering procedure of the TLM.

Assuming a nondispersive nature of biological tissue, the nondispersive or stub-loaded SCN TLM method was used to obtain the near field data and the specific absorption rate (SAR) distribution. The results of both cases have been compared. Several simulations were carried out to check the validity and accuracy of the modified TLM technique for homogeneous nondispersive and dispersive dielectric bodies. The modified TLM technique was then applied to nonhomogeneous and geometrically complex dispersive body, which is the human head. Three models of the head were used: a simplified model of 209 coarse cells, a refined model of 24552 cells and a much refined model of 196416 cells.

To investigate the possibility of the reconstruction of three-dimensional dielectric bodies from scattered field data, the unrelated illumination method has been used. The method utilizes the method of moments (MoM) to discretize the nonlinear integral equation, which relates the scattered field data and the complex permittivity distribution of the body. It is thus a frequency domain technique. The method requires that the body under investigation be illuminated by a group of unrelated incident fields, thus forcing the

incident matrix to be nonsingular. This incident fields are obtained using two planar phased arrays. The values of the scattered field at the measuring points are obtained by solving the forward scattering problem. The inverse scattering procedure is based on obtaining the inverse of the incident field matrix. Through performing some simple matrix operations, the complex permittivity distribution of the body is reconstructed.

This method, although similar to the other multi-view illumination methods, has the advantage of providing accurate reconstruction using only one measuring point or detector and without any iterations. Thus it reduces the required computation time and still provides good accuracy. Numerical simulations were carried out to evaluate the capabilities of this method. In the absence of noise, the reconstruction error was negligible irrespective of the complex permittivity distribution or the cell size. To simulate realistic measurement conditions, the results are generated in the presence of Gaussian noise with zero mean added to the scattered field at the measuring points.

It has been shown that the method can handle both strong and weak scatterers of different densities. Also, better reconstruction has been obtained for smaller cell sizes. The unrelated illumination method can be used for the reconstruction of both lossless and lossy inhomogeneous dielectric bodies. It can also equally handle simple or geometrically complex bodies. Using a model for the human head and another for the human body, it has been shown that for realistic signal to noise ratios, the method provides a reliable basis for the reconstruction dielectric parameters. Acceptable error levels have been obtained for higher frequencies. The effect of varying the detector location has also been studied.

In conclusion, we have attempted to study both the forward and inverse electromagnetic scattering from biological tissue. Two numerical techniques have been used, the SCN TLM which is a time domain technique and the MoM which is a frequency domain technique. The choice of the technique was made based on its suitability to handle the problem under consideration.

6.2 Future Research:

The interaction of electromagnetic radiation with biological tissue has been studied in this thesis. Both the forward and inverse scattering problems of electromagnetic waves have been investigated. The ability to model the dispersive nature of biological tissue using second order Debye equation in a modified TLM technique can be considered as preliminary work. It offers an accurate way to study the energy deposition and the various fields that exist in a biological body after an exposure to electromagnetic waves. Further simulations can be carried out to model realistic situations especially those involving wireless communications. The results could be compared to those available assuming frequency independent biological tissue.

A different issue that could be further studied is using higher orders of Debye approximation, which are more accurate, to model dispersive tissue. How this would affect the SAR levels in a body after exposure to electromagnetic waves, is an interesting point and can help investigate the need to use higher order formulae to model dispersive tissue.

The reconstruction of the complex permittivity distribution of dielectric bodies using the method of moments (MoM) has been shown to be very proving. Yet, research

can still be done on the planner phased array antennas that are used to obtain the required incident field. Once an optimum design for an antenna array of acceptable size is available, it should be implemented physically. The whole procedure should then be tested as it has been proven theoretically, in this thesis, to be a very reliable three-dimensional imaging procedure. To further improve the resolution of the reconstructed bodies, the use of smaller cell size could also be studied. This is directly related to the design of the planner phased array antennas as it requires incident fields of smaller half power beam width (HPBW).

APPENDIX A

Modeling of Second Order Debye Dielectric

In Chapter 3, we have shown how to model a dispersive material that can be expressed as a second order Debye equation in the TLM method. The conductivity σ and the dielectric permittivity ε_r of a medium can be combined together to form the complex permittivity constant which is a frequency dependent quantity and defined as:

$$\varepsilon^* = \varepsilon' - j\frac{\sigma}{\omega\varepsilon_o} \quad \text{or} \quad \varepsilon^* = \varepsilon' - j\varepsilon'' \tag{A. 1}$$

For a dispersive dielectric medium the frequency domain permittivity constant $\varepsilon^*(\omega)$ can be modeled using second order Debye equation [59]:

$$\varepsilon^*(\omega) = \varepsilon_\infty + \frac{\varepsilon_{s1} - \varepsilon_\infty}{1 + j\omega\tau_1} + \frac{\varepsilon_{s2} - \varepsilon_\infty}{1 + j\omega\tau_2} \tag{A. 2}$$

Where ε_∞ is the permittivity at infinite frequency, $\varepsilon_s = \varepsilon_{s1} + \varepsilon_{s2} - \varepsilon_\infty$ is the zero or static permittivity and τ_1 and τ_2 are the relaxation time constants.

As shown in Chapter 3, the second order Debye equation (A.2) can be modeled by the *RC* circuit shown in Fig. A.1. In this section, we attempt to obtain the expressions

for the various circuit components in term of the parameters of the second order Debye equation (A.2).

The first step is to obtain the impedance of the circuit shown in Fig. A.1. The mathematical formula for the impedance is then compared with the relation between the voltage and current as obtained from equation (A.2), as will be shown. From the

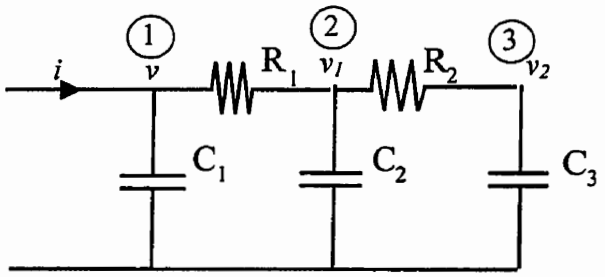

Fig. A.1. Circuit model for second order Debye dielectric.

comparison of the two equivalent formulae, we will be able to find the required expressions for the various circuit components.

The input impedance for the above circuit is given by combining the various series and shunt components as:

$$Z = \frac{v}{i} = \frac{1 + j\omega(C_3R_2 + C_2R_1 + C_3R_1) - \omega^2 C_2C_3R_1R_2}{j\omega(C_1 + C_2 + C_3) - \omega^2(C_1C_3R_2 + C_1C_2R_1 + C_1C_3R_1 + C_2C_3R_2) - j\omega^3 C_1C_2C_3R_1R_2} \quad \text{(A. 3)}$$

From equation (A.2), we get:

$$\varepsilon^*(\omega) = \frac{\varepsilon_s + j\omega(\varepsilon_{s1}\tau_2 + \varepsilon_{s2}\tau_1) - \omega^2\tau_1\tau_2\varepsilon_\infty}{1 + j\omega(\tau_1 + \tau_2) - \omega^2\tau_1\tau_2} \quad \text{(A. 4)}$$

The next step is to obtain the expression for (ε*-*1*):

$$\varepsilon^*(\omega) - 1 = \frac{(\varepsilon_s - 1) + j\omega((\varepsilon_{s1} - 1)\tau_2 + (\varepsilon_{s2} - 1)\tau_1) - \omega^2\tau_1\tau_2(\varepsilon_\infty - 1)}{1 + j\omega(\tau_1 + \tau_2) - \omega^2\tau_1\tau_2} \quad \text{(A. 5)}$$

The polarization P is related to the electric field E via this equation:

$$P(\omega) = (\varepsilon^*(\omega) - 1)E(\omega) \quad \text{(A. 6)}$$

Substituting for $(\varepsilon^*(\omega) - 1)$ in equation (A.6)

$$P(\omega)(1 + j\omega(\tau_1 + \tau_2) - \omega^2\tau_1\tau_2) = ((\varepsilon_s - 1) + j\omega((\varepsilon_{s1} - 1)\tau_2 + (\varepsilon_{s2} - 1)\tau_1) - \omega^2\tau_1\tau_2(\varepsilon_\infty - 1))E(\omega)$$

(A. 7)

And writing the above equation in the time domain:

$$P + (\tau_1 + \tau_2)\frac{dP}{dt} + \tau_1\tau_2\frac{d^2P}{dt^2} = (\varepsilon_s - 1)E + ((\varepsilon_{s1} - 1)\tau_2 + (\varepsilon_{s2} - 1)\tau_1)\frac{dE}{dt} + \tau_1\tau_2(\varepsilon_\infty - 1)\frac{d^2E}{dt^2}$$

(A. 8)

The polarization current *i* is related to the polarization *P*:

$$i = 2\Delta t\frac{dP}{dt} \quad \text{(A. 9)}$$

From the analogy between field and circuit quantities:

$$E = v \quad \text{(A. 10)}$$

Substituting (A.9) and (A.10) in (A.8):

$$\frac{1}{2\Delta t}\left(i+(\tau_1+\tau_2)\frac{di}{dt}+\tau_1\tau_2\frac{d^2i}{dt^2}\right)=(\varepsilon_s-1)\frac{dv}{dt}+\left((\varepsilon_{s1}-1)\tau_2+(\varepsilon_{s2}-1)\tau_1\right)\frac{d^2v}{dt^2}+\tau_1\tau_2(\varepsilon_\infty-1)\frac{d^3v}{dt^3}$$

(A. 11)

Changing to the frequency domain and rearranging, we get the relationship between the voltage and current in terms of the second order Debye parameters:

$$\frac{v}{i}=\frac{1+j\omega(\tau_1+\tau_2)-\omega^2\tau_2\tau_2}{2\Delta t\left[(\varepsilon_s-1)j\omega-\omega^2\left(\tau_1(\varepsilon_{s2}-1)+\tau_2(\varepsilon_{s1}-1)\right)-j\omega^3\tau_1\tau_2(\varepsilon_\infty-1)\right]} \tag{A. 12}$$

Through comparing the coefficients of the various terms of equations (A.3) and (A.12), we can get the expressions for the circuit components of Fig. A.1 in terms of the second order Debye parameters. The five equations that result from the coefficients comparison are:

$$C_3R_2+C_2R_1+C_3R_1=\tau_1+\tau_2 \tag{A.13}$$

$$C_2C_3R_1R_2=\tau_1\tau_2 \tag{A.14}$$

$$(C_1+C_2+C_3)=2\Delta t(\varepsilon_s-1) \tag{A.15}$$

$$(C_1C_3R_2+C_1C_2R_1+C_1C_3R_1+C_2C_3R_2)=2\Delta t(\varepsilon_{s1}\tau_2+\varepsilon_{s2}\tau_1-\tau_1-\tau_2) \tag{A.16}$$

$$C_1C_2C_3R_1R_2=\tau_1\tau_2(\varepsilon_\infty-1)2\Delta t \tag{A.17}$$

Through simple mathematical substitutions in the previous five equations, we get the following expressions:

$$C_1=(\varepsilon_\infty-1)2\Delta t \tag{A.18}$$

$$C_2 = \frac{2\Delta t(\varepsilon_{s1}\tau_2 + \varepsilon_{s2}\tau_1 - \varepsilon_\infty(\tau_1+\tau_2))^2}{(\varepsilon_{s1}\tau_2 + \varepsilon_{s2}\tau_1 - \varepsilon_\infty(\tau_1+\tau_2))(\tau_1+\tau_2) - \tau_1\tau_2(\varepsilon_s - \varepsilon_\infty)} \quad \text{(A. 19)}$$

$$C_3 = 2\Delta t(\varepsilon_s - \varepsilon_\infty) - \frac{2\Delta t(\varepsilon_{s1}\tau_2 + \varepsilon_{s2}\tau_1 - \varepsilon_\infty(\tau_1+\tau_2))^2}{(\varepsilon_{s1}\tau_2 + \varepsilon_{s2}\tau_1 - \varepsilon_\infty(\tau_1+\tau_2))(\tau_1+\tau_2) - \tau_1\tau_2(\varepsilon_s - \varepsilon_\infty)} \quad \text{(A. 20)}$$

$$R_1 = \tau_1\tau_2 / 2\Delta t(\varepsilon_{s1}\tau_2 + \varepsilon_{s2}\tau_1 - \varepsilon_\infty(\tau_1+\tau_2)) \quad \text{(A. 21)}$$

$$R_2 = \frac{2\Delta t(\varepsilon_{s1}\tau_2 + \varepsilon_{s2}\tau_1 - \varepsilon_\infty(\tau_1+\tau_2))}{C_2 C_3} \quad \text{(A. 22)}$$

APPENDIX B

Green's Function Formulation

In Chapter 4, starting from Maxwell's equation we have derived the equations relating the total and scattered field inside a dielectric body:

$$\mathbf{E}^s(r) = \int_v \overline{\overline{\mathbf{G}}}(r,r')(k^2(r') - k_b^2)\mathbf{E}(r')dv' \tag{B. 1}$$

Using the equivalent current density $\mathbf{J}_{eq}$, equation (B.1) can be written as:

$$\mathbf{E}^s(r) = \int_v \overline{\overline{\mathbf{G}}}(r,r') \cdot \mathbf{J}_{eq}(r')dv' \tag{B. 2}$$

In the above equation $\overline{\overline{\mathbf{G}}}(r,r')$ has a singularity, the integral equation (B.1) will diverge if the field point r is inside the volume v of the body. This diversion is overcome by defining the principal value (PV) to which a correction term is added. The principal value PV is an integral equation that is valid everywhere except where the singularity occurs. The correction term is added only when the source and the field point approach each other. It can be evaluated by excluding a small volume surrounding the singular field point first and then letting the small volume approach zero. Equation (B.2) can thus be written as:

$$\mathbf{E}^s(r) = PV\int_v \overline{\overline{\mathbf{G}}}(r,r')\cdot\mathbf{J}_{eq}(r')dv' + \left[\mathbf{E}^s(r)\right]_{correction} \tag{B. 3}$$

The correction term depends on the geometry of the volume over which equation (B.3) is evaluated. It has been shown that the correction term for a sphere is [110]:

$$\left[\mathbf{E}^s(r)\right]_{correction} = -\frac{\mathbf{J}_{eq}(r)}{3j\omega\varepsilon_o} \tag{B. 4}$$

Rewriting equation (B.3):

$$\mathbf{E}^s(r) = PV\int_v \overline{\overline{\mathbf{G}}}(r,r')\cdot\mathbf{J}_{eq}(r')dv' - \frac{\mathbf{J}_{eq}(r)}{3j\omega\varepsilon_o} \tag{B. 5}$$

The total electric field $\mathbf{E}$ at an arbitrary point r can be expressed in terms of the incident and scattered fields as:

$$\mathbf{E}(r) = \mathbf{E}^i(r) + \mathbf{E}^s(r) \tag{B. 6}$$

Substituting equation (B.5) in (B.6) and rearranging:

$$\left[1 + \frac{\Gamma(r)}{3j\omega\varepsilon_o}\right]\mathbf{E}(r) - PV\int_v \Gamma(r')\overline{\overline{\mathbf{G}}}(r,r')\cdot\mathbf{E}(r')dv' - \mathbf{E}^i(r) \tag{B. 7}$$

where

$$\Gamma(r) = \sigma(r) + j\omega[\varepsilon(r) - \varepsilon_o] \tag{B. 8}$$

In equation (B.7) the only unknown is the total field inside the body and can be determined using the method of moments.

The inner product in equation (B.7) can be represented as:

$$\overline{\overline{\mathbf{G}}}(r,r')\cdot\mathbf{E}(r)=\begin{bmatrix}\mathbf{G}_{xx}(r,r') & \mathbf{G}_{xy}(r,r') & \mathbf{G}_{xz}(r,r')\\ \mathbf{G}_{yx}(r,r') & \mathbf{G}_{yy}(r,r') & \mathbf{G}_{yz}(r,r')\\ \mathbf{G}_{zx}(r,r') & \mathbf{G}_{zy}(r,r') & \mathbf{G}_{zz}(r,r')\end{bmatrix}\begin{bmatrix}E_x(r,r')\\ E_y(r,r')\\ E_z(r,r')\end{bmatrix} \tag{B. 9}$$

Denoting x, y and z by x_1, x_2 and x_3, the entries in the matrix above can be written as:

$$G_{x_p x_q}(r,r')=-j\omega\mu\left[\delta_{pq}+\frac{1}{k_o^2}\frac{\partial^2}{\partial x_q\partial x_p}\right]G_o(r,r') \tag{B. 10}$$

where $p,q = 1,2,3$.

The method of moments with pulse basis function and point matching procedure can now be applied to equation (B.7). This results in the following expressions for the elements of the Green's function matrix:

For non-diagonal elements:

$$G_{x_p x_q}^{mn}=\frac{-j\omega\mu k_o\Gamma(r_n)\Delta V_n\exp(-j\alpha_{mn})}{4\pi\alpha_{mn}^3}\left[\left(\alpha_{mn}^2-1-j\alpha_{mn}\right)\delta_{pq}+\cos\theta_{x_p}^{mn}\theta_{x_p}^{mn}\left(3-\alpha_{mn}^2+3j\alpha_{mn}\right)\right] \tag{B. 11}$$

where

$$\alpha_{mn}=k_o|r_m-r_n|,\ \cos\theta_{x_p}^{mn}=\frac{\left(x_p^m-x_p^n\right)}{|r_m-r_n|}\ \text{and}\ \cos\theta_{x_q}^{mn}=\frac{\left(x_q^m-x_q^n\right)}{|r_m-r_n|}$$

and $r_m=\left(x_1^m,x_2^m,x_3^m\right)\qquad r_n=\left(x_1^n,x_2^n,x_3^n\right)$

For the diagonal elements:

$$G_{x_p x_q}^{nn}=\delta_{pq}\left\{\frac{-2j\omega\mu\Gamma(r_n)}{3k_o^3}\left[\exp(-jk_o a_n)(1+jk_o a_n)-1\right]-\left[1+\frac{\Gamma(r_n)}{3j\omega\varepsilon_o}\right]\right\} \tag{B. 12}$$

Detailed derivation of the expressions of the Green's function matrix are given in [109]-[110].

APPENDIX C

Parameters of the Human Body Model

The 180 cubic cell human body model that has been used is characterised by a variable cell size. The parameters of the model including the cell number, volume, relative location and dielectric properties are given in Table C.1.

Table C.1 Volume, location and dielectric properties of the 180-cell human body model.

Cell no.	volume	x	y	z	σ	$\varepsilon_o\varepsilon_r$
1	2.88E-04	1.717	0.033	0.1678	0.38	7.16E-10
2	4.65E-04	1.6452	0.0388	0.162	0.84	7.07E-10
3	4.65E-04	1.5677	0.0388	0.177	0.84	7.07E-10
4	1.74E-04	1.4998	0.0292	0.1335	0.843	7.07E-10
5	4.22E-04	1.433	0.0375	0.15	0.84	7.07E-10
6	4.22E-04	1.433	0.1125	0.15	0.84	7.07E-10
7	4.22E-04	1.358	0.0375	0.1875	1.0849	7.07E-10
8	4.22E-04	1.358	0.1125	0.1875	0.84	7.07E-10
9	4.22E-04	1.283	0.0375	0.1875	0.843	8.63E-10
10	4.22E-04	1.283	0.1125	0.1875	0.84	7.07E-10
11	4.22E-04	1.208	0.0375	0.1875	0.84	7.07E-10
12	4.22E-04	1.208	0.1125	0.1875	0.84	7.07E-10
13	3.14E-04	1.1365	0.034	0.177	0.84	7.07E-10
14	3.14E-04	1.1365	0.102	0.177	0.84	7.07E-10
15	4.22E-04	1.065	0.0375	0.1875	0.84	7.07E-10
16	4.22E-04	1.065	0.1125	0.1875	0.84	7.07E-10
17	4.22E-04	0.99	0.0375	0.1875	0.84	7.07E-10

18	4.22E-04	0.99	0.1125	0.1875	0.84	7.07E-10
19	5.77E-04	0.9109	0.0416	0.1249	0.84	7.07E-10
20	5.77E-04	0.9109	0.1249	0.1249	0.84	7.07E-10
21	5.51E-04	0.8282	0.0435	0.1249	0.84	7.07E-10
22	5.51E-04	0.8282	0.1255	0.1249	0.84	7.07E-10
23	3.73E-04	0.7513	0.0385	0.1249	0.84	7.07E-10
24	3.73E-04	0.7513	0.1102	0.1249	0.84	7.07E-10
25	2.16E-04	0.6853	0.0325	0.1189	0.84	7.07E-10
26	2.16E-04	0.6853	0.0925	0.1189	0.84	7.07E-10
27	1.85E-04	0.6267	0.031	0.1174	0.84	7.07E-10
28	1.85E-04	0.6267	0.088	0.1174	0.84	7.07E-10
29	1.41E-04	0.5723	0.0285	0.1149	0.84	7.07E-10
30	1.41E-04	0.5723	0.0802	0.1149	0.84	7.07E-10
31	1.11E-03	0.4945	0.0543	0.1149	0.84	7.07E-10
32	1.11E-03	0.3908	0.0543	0.0887	0.84	7.07E-10
33	1.11E-03	0.2873	0.0543	0.0887	0.84	7.07E-10
34	4.39E-04	0.1975	0.0405	0.0887	0.84	7.07E-10
35	4.39E-04	0.1215	0.1165	0.0887	0.84	7.07E-10
36	5.93E-04	0.0415	0.0445	0.2269	0.84	7.07E-10
37	2.88E-04	1.717	0.033	0.1018	0.38	7.16E-10
38	4.65E-04	1.6452	0.0388	0.0845	0.84	7.07E-10
39	4.65E-04	1.5677	0.0388	0.0995	0.84	7.07E-10
40	2.00E-04	1.4998	0.0292	0.075	0.84	7.07E-10
41	4.22E-04	1.433	0.0375	0.075	0.84	7.07E-10
42	4.22E-04	1.433	0.1125	0.075	0.84	7.07E-10
43	4.22E-04	1.358	0.0375	0.1125	0.7	5.31E-10
44	4.22E-04	1.358	0.1125	0.1125	0.84	7.07E-10
45	4.22E-04	1.283	0.0375	0.1125	0.1	5.31E-10
46	4.22E-04	1.283	0.1125	0.1125	0.84	7.07E-10
47	4.22E-04	1.208	0.0375	0.1125	0.84	7.07E-10
48	4.22E-04	1.208	0.1125	0.1125	0.84	7.07E-10
49	3.14E-04	1.1365	0.034	0.109	0.84	7.07E-10
50	3.14E-04	1.1365	0.102	0.109	0.84	7.07E-10
51	4.22E-04	1.065	0.0375	0.1125	1.11	8.31E-10
52	4.22E-04	1.065	0.1125	0.1125	0.84	7.07E-10
53	4.22E-04	0.99	0.0375	0.1125	0.84	7.07E-10
54	4.22E-04	0.99	0.1125	0.1125	0.84	7.07E-10
55	4.22E-04	1.358	0.0375	0.0375	0.84	7.07E-10
56	4.22E-04	1.358	0.1125	0.0375	0.84	7.07E-10
57	4.22E-04	1.283	0.0375	0.0375	0.84	7.07E-10
58	4.22E-04	1.283	0.1125	0.0375	0.84	7.07E-10
59	4.22E-04	1.208	0.0375	0.0375	0.84	7.07E-10

60	4.22E-04	1.208	0.1125	0.0375	0.84	7.07E-10
61	3.14E-04	1.1365	0.034	0.041	0.84	7.07E-10
62	3.14E-04	1.1365	0.102	0.041	0.84	7.07E-10
63	4.22E-04	1.065	0.0375	0.0375	0.84	7.07E-10
64	4.22E-04	1.065	0.1125	0.0375	0.84	7.07E-10
65	4.22E-04	0.99	0.0375	0.0375	0.84	7.07E-10
66	4.22E-04	0.99	0.1125	0.0375	0.84	7.07E-10
67	5.77E-04	0.9109	0.0413	0.0416	0.84	7.07E-10
68	5.77E-04	0.9109	0.1249	0.0416	0.84	7.07E-10
69	5.51E-04	0.8282	0.0435	0.0845	0.84	7.07E-10
70	5.51E-04	0.8282	0.1255	0.0845	0.84	7.07E-10
71	3.73E-04	0.7513	0.0385	0.0529	0.84	7.07E-10
72	3.73E-04	0.7513	0.1102	0.0529	0.84	7.07E-10
73	2.16E-04	0.6853	0.0325	0.0589	0.84	7.07E-10
74	2.16E-04	0.6853	0.081	0.0589	0.84	7.07E-10
75	1.85E-04	0.6267	0.031	0.0604	0.84	7.07E-10
76	1.85E-04	0.6267	0.088	0.0604	0.84	7.07E-10
77	1.41E-04	0.5723	0.0285	0.0629	0.84	7.07E-10
78	1.41E-04	0.5723	0.0802	0.0629	0.84	7.07E-10
79	5.93E-04	0.0389	0.0445	0.1429	0.84	7.07E-10
80	5.93E-04	0.0389	0.0445	0.0589	0.84	7.07E-10
81	5.93E-04	1.433	0.192	0.1125	0.84	7.07E-10
82	5.93E-04	1.349	0.192	0.1125	0.84	7.07E-10
83	5.93E-04	1.265	0.197	0.1125	0.84	7.07E-10
84	5.31E-04	1.1825	0.1985	0.1125	0.84	7.07E-10
85	5.31E-04	1.1015	0.1985	0.1125	0.84	7.07E-10
86	4.22E-04	1.0235	0.2015	0.1125	0.84	7.07E-10
87	4.22E-04	0.9485	0.2015	0.1125	0.84	7.07E-10
88	2.27E-04	0.8805	0.2015	0.1125	0.84	7.07E-10
89	1.95E-04	0.8201	0.2	0.1125	0.84	7.07E-10
90	1.11E-04	0.768	0.195	0.1125	0.84	7.07E-10
91	2.88E-04	1.717	-0.033	0.1678	0.38	7.16E-10
92	4.65E-04	1.6452	-0.039	0.162	0.84	7.07E-10
93	4.65E-04	1.5677	-0.039	0.177	0.84	7.07E-10
94	1.74E-04	1.4998	-0.029	0.1335	0.84	7.07E-10
95	4.22E-04	1.433	-0.038	0.15	0.84	7.07E-10
96	4.22E-04	1.433	-0.113	0.15	0.84	7.07E-10
97	4.22E-04	1.358	-0.038	0.1875	1.0849	8.63E-10
98	4.22E-04	1.358	-0.113	0.1875	0.84	7.07E-10
99	4.22E-04	1.283	-0.038	0.1875	0.84	7.07E-10
100	4.22E-04	1.283	-0.113	0.1875	0.84	7.07E-10
101	4.22E-04	1.208	-0.038	0.1875	0.84	7.07E-10

102	4.22E-04	1.208	-0.113	0.1875	0.84	7.07E-10
103	3.14E-04	1.1365	-0.034	0.177	0.84	7.07E-10
104	3.14E-04	1.1365	-0.102	0.177	0.84	7.07E-10
105	4.22E-04	1.065	-0.038	0.1875	0.84	7.07E-10
106	4.22E-04	1.065	-0.113	0.1875	0.84	7.07E-10
107	4.22E-04	0.99	-0.038	0.1875	0.84	7.07E-10
108	4.22E-04	0.99	-0.113	0.1875	0.84	7.07E-10
109	5.77E-04	0.9109	-0.042	0.1249	0.84	7.07E-10
110	5.77E-04	0.9109	-0.125	0.1249	0.84	7.07E-10
111	5.51E-04	0.8282	-0.044	0.1249	0.84	7.07E-10
112	5.51E-04	0.8282	-0.126	0.1249	0.84	7.07E-10
113	3.73E-04	0.7513	-0.039	0.1249	0.84	7.07E-10
114	3.73E-04	0.7513	-0.11	0.1249	0.84	7.07E-10
115	2.16E-04	0.6853	-0.033	0.1189	0.84	7.07E-10
116	2.16E-04	0.6853	-0.093	0.1189	0.84	7.07E-10
117	1.85E-04	0.6267	-0.031	0.1174	0.84	7.07E-10
118	1.85E-04	0.6267	-0.088	0.1174	0.84	7.07E-10
119	1.41E-04	0.5723	-0.029	0.1149	0.84	7.07E-10
120	1.41E-04	0.5723	-0.08	0.1149	0.84	7.07E-10
121	1.11E-03	0.4945	-0.054	0.1149	0.84	7.07E-10
122	1.11E-03	0.3908	-0.054	0.0887	0.84	7.07E-10
123	1.11E-03	0.2873	-0.054	0.0887	0.84	7.07E-10
124	4.39E-04	0.1975	-0.041	0.0887	0.84	7.07E-10
125	4.39E-04	0.1215	-0.117	0.0887	0.84	7.07E-10
126	5.93E-04	0.0415	-0.045	0.2269	0.84	7.07E-10
127	2.88E-04	1.717	-0.033	0.1018	0.38	7.16E-10
128	4.65E-04	1.6452	-0.039	0.0845	0.84	7.07E-10
129	4.65E-04	1.5677	-0.039	0.0995	0.84	7.07E-10
130	2.00E-04	1.4998	-0.029	0.075	0.84	7.07E-10
131	4.22E-04	1.433	-0.038	0.075	0.84	7.07E-10
132	4.22E-04	1.433	-0.113	0.075	0.84	7.07E-10
133	4.22E-04	1.358	-0.038	0.1125	0.1	5.31E-10
134	4.22E-04	1.358	-0.113	0.1125	0.84	7.07E-10
135	4.22E-04	1.283	-0.038	0.1125	0.1	5.31E-10
136	4.22E-04	1.283	-0.113	0.1125	0.84	7.07E-10
137	4.22E-04	1.208	-0.038	0.1125	0.84	7.07E-10
138	4.22E-04	1.208	-0.113	0.1125	0.84	7.07E-10
139	3.14E-04	1.1365	-0.034	0.109	0.84	7.07E-10
140	3.14E-04	1.1365	-0.102	0.109	0.84	7.07E-10
141	4.22E-04	1.065	-0.038	0.1125	1.11	8.31E-10
142	4.22E-04	1.065	-0.113	0.1125	0.84	7.07E-10
143	4.22E-04	0.99	-0.038	0.1125	0.84	7.07E-10

144	4.22E-04	0.99	-0.113	0.1125	0.84	7.07E-10
145	4.22E-04	1.358	-0.038	0.0375	0.84	7.07E-10
146	4.22E-04	1.358	-0.113	0.0375	0.84	7.07E-10
147	4.22E-04	1.283	-0.038	0.0375	0.84	7.07E-10
148	4.22E-04	1.283	-0.113	0.0375	0.84	7.07E-10
149	4.22E-04	1.208	-0.038	0.0375	0.84	7.07E-10
150	4.22E-04	1.208	-0.113	0.0375	0.84	7.07E-10
151	3.14E-04	1.1365	-0.034	0.041	0.84	7.07E-10
152	3.14E-04	1.1365	-0.102	0.041	0.84	7.07E-10
153	4.22E-04	1.065	-0.038	0.0375	0.84	7.07E-10
154	4.22E-04	1.065	-0.113	0.0375	0.84	7.07E-10
155	4.22E-04	0.99	-0.038	0.0375	0.84	7.07E-10
156	4.22E-04	0.99	-0.113	0.0375	0.84	7.07E-10
157	5.77E-04	0.9109	-0.041	0.0416	0.84	7.07E-10
158	5.77E-04	0.9109	-0.125	0.0416	0.84	7.07E-10
159	5.51E-04	0.8282	-0.044	0.0845	0.84	7.07E-10
160	5.51E-04	0.8282	-0.126	0.0845	0.84	7.07E-10
161	3.73E-04	0.7513	-0.039	0.0529	0.84	7.07E-10
162	3.73E-04	0.7513	-0.11	0.0529	0.84	7.07E-10
163	2.16E-04	0.6853	-0.033	0.0589	0.84	7.07E-10
164	2.16E-04	0.6853	-0.081	0.0589	0.84	7.07E-10
165	1.85E-04	0.6267	-0.031	0.0604	0.84	7.07E-10
166	1.85E-04	0.6267	-0.088	0.0604	0.84	7.07E-10
167	1.41E-04	0.5723	-0.029	0.0629	0.84	7.07E-10
168	1.41E-04	0.5723	-0.08	0.0629	0.84	7.07E-10
169	5.93E-04	0.0389	-0.045	0.1429	0.84	7.07E-10
170	5.93E-04	0.0389	-0.045	0.0589	0.84	7.07E-10
171	5.93E-04	1.433	-0.192	0.1125	0.84	7.07E-10
172	5.93E-04	1.349	-0.192	0.1125	0.84	7.07E-10
173	5.93E-04	1.265	-0.197	0.1125	0.84	7.07E-10
174	5.31E-04	1.1825	-0.199	0.1125	0.84	7.07E-10
175	5.31E-04	1.1015	-0.199	0.1125	0.84	7.07E-10
176	4.22E-04	1.0235	-0.202	0.1125	0.84	7.07E-10
177	4.22E-04	0.9485	-0.202	0.1125	0.84	7.07E-10
178	2.27E-04	0.8805	-0.202	0.1125	0.84	7.07E-10
179	1.95E-04	0.8201	-0.2	0.1125	0.84	7.07E-10
180	1.11E-04	0.768	-0.195	0.1125	0.84	7.07E-10

REFERENCES:

[1] R. J. Spiegel, "A review of numerical models for predicting the energy deposition and resultant thermal response of humans exposed to electromagnetic fields," *IEEE Trans. Microwave Theory Tech.*, vol. 32, no. 8, pp. 730-745, 1984.

[2] H. T. Banks, *Modeling and Control in the Biomedical Sciences*, Springer-Verlag, 1975.

[3] R. F. Harrington, *Field Computation by Moment Methods*, Macmillan, 1968.

[4] J. B. Keller, "Geometrical theory of diffraction," *J. Opt. Soc. AM.*, vol. 52, pp. 116, 1962.

[5] R. Gomez, A. Salinas, A. Rubio Bretores and M. Martin, "Time-domain integral equation for EMP analysis transmission-line system," *Int. J. Num. Mod.*, vol. 4, pp. 153-162, 1991.

[6] E. K. Miller, "A selective survey of computational electromagnetics," *IEEE Trans. Antennas Propagat.*, vol. 36, pp. 1281-1305, 1988.

[7] K. S. Yee, "Numerical solution of initial boundary value problems involving Maxwell's equations in isotropic media," *IEEE Trans. Antennas Propagat.*, vol. 14, pp. 302-307, 1966.

[8] S. Akhtarzad and P. B. Johns, "Solution of Maxwell's equations in three space dimensions and time by the TLM method of numerical analysis," *Proc. IEE*, vol. 122, pp. 1344-1348, 1975.

[9] M. N. O. Sadiku, *Numerical Techniques in Electromagnetics*, CRC Press, 1992.

[10] T. Itoh, Ed. *Numerical Techniques for Microwave and Millimeter Wave Passive Structures,* John Wiley & Sons, New York, pp. 469-591, 1989.

[11] R. C. Booton Jr., *Computational Methods for Electromagnetics and Microwaves*, John Wiley & Sons, New York, 1992.

[12] P. Silvester, *Finite Elements for electrical Engineers*, Camberidge University Press, New York, 1983.

[13] G. Mur, "Finite difference method for the solution of electromagnetic waveguide discontinuity problem," *IEEE Trans. Microwave Theory Tech.*, vol. 22, pp. 54-57, 1974.

[14] D. E. Merewether and R. Fisher, "Finite-difference analysis of EM fields inside complex cavities driven by large apertures," *IEEE Trans. Electromag. Compat.*, vol. 24, pp. 406-410, 1982.

[15] N. Nabaya, P. E. Lagasse and P. Vandenbulcke, "Finite element analysis of optical waveguides," *IEEE Trans. Microwave Theory Tech.*, vol. 29, pp. 600-605, 1981.

[16] M. J. Beaubien and A. Wexler, "An accurate finite-difference method for higher order waveguide modes," *IEEE Trans. Microwave Theory Tech.*, vol. 16, pp. 1007-1017, 1968.

[17] S. Castillo, Z. Pantiac and R. Mittra, "Finite-element analysis of multiconductor printed-circuit transmission-line system," *Int. J. Num. Math. Engrg.*, vol. 29, pp. 1033-1047, 1980.

[18] Johns, P.B. and R. L. Beurle, "Numerical solution of 2 dimensional scattering problems using a transmission line matrix," *Proc. IEE*, vol. 118, no. 9, pp. 1203-1208, 1971.

[19] C. Christopoulos, *The Transmission-Line Modeling Method - TLM*, IEEE Press, 1995.

[20] W. J. R. Hoefer, "The transmission-line matrix method - theory and applications," *IEEE Trans. Microwave Theory Tech.*, vol. 33, no. 10, pp. 882-893, 1985.

[21] R. E. Collin, *Field Theory of Guided Waves*, IEEE Press, Piscataway N.J., 1991.

[22] R. F. Harrington, *Time-Harmonic Electromagnetic Fields*, Mc-Graw Hill, New York, 1961.

[23] P. Naylor and R. Ait-Sadi, "Simple method for determining 3 D TLM nodal scattering parameters in nonscalar problems," *IEE Electronic letters*, vol. 28, pp. 2353-2354, 1992.

[24] A. Taflove and K. Umashankar, "Review of FD-TD numerical modelling of electromagnetic wave scattering and radar cross section," *Proc. IEEE*, vol. 77, no. 5, pp. 682-699, 1989.

[25] P. B. Johns, "A symmetric condensed node for TLM method," *IEEE Trans. Microwave Theory Tech.*, vol. 35, no. 4, pp. 370-377, 1987.

[26] R. Allen, A. Mallik and P. B. Johns, "Numerical results for the symmetric condensed TLM node," *IEEE Trans. Microwave Theory Tech.*, vol. 35, no. 4, pp. 378-382, 1987.

[27] C. Christopoulus and J. L. Herring, "The application of transmission-line modelling (TLM) to electromagnetic compatability problems," *IEEE Trans. Electromag. Compat.*, vol. 35, pp. 185-191, 1993.

[28] J. L. Herring, P. Naylor and C. Christopoulus, "The application of transmission line modelling to electromagnetic compatability studies," *International Journal of Numerical Modelling*, vol. 4, pp. 143-152, 1991.

[29] P. Naylor and C. Christopoulus, "Coupling between electromagnetic fields and multimode transmission line using TLM," *Int. J. Num. Mod*, vol. 2, pp. 227-240, 1989.

[30] G. E. Mariki and C. Yeh, "Dynamic three-dimensionl TLM analysis of microstrip lines on anisotropic substrate," *IEEE Trans. Microwave Theory Tech.*, vol. 33, pp. 789-799, 1985.

[31] P. P. M. So, G. I. Eswarappa and W. J. R. Hoefer, "A two-dimensional transmission line matrix microwave field simulator using new concepts and procedures," *IEEE Trans. Microwave Theory Tech.*, vol. 37, pp. 1877-1884, 1989.

[32] A. P. Duffy, J. L. Herring, T. M. Benson and C. Christopoulos, "Improved wire modelling in TLM," *IEEE Trans. Microwave Theory Tech.*, vol. 42, pp. 1978-1983, 1994.

[33] P. Russer, M. Righi, C. Eswarappa and W. J. R. Hoefer, "Lumped element equivalent circuit parameter extraction of distributed microwave circuits via TLM simulation," *IEEE MTT-S International Symposium Digest*, pp. 887-890, 1994.

[34] F. J. German, G. K. Gothard and L. S. Riggs, "RCS of three-dimensional scatterers using the symmetric condensed TLM method," *Electronics Letters*, vol. 26, pp. 673, 1990.

[35] N. R. S. Simons, A. A. Sebak and E. Bridges, "Transmission-line matrix (TLM) method for scattering problems," *Computer Physics Comms.*, vol. 68, pp. 197-212, 1991.

[36] F. Ndagijimana, P. Saguet and M. Bouthinon, "Tapered slot antenna analysis with 3D TLM method," *Electronics Letters*, vol. 26, pp. 468-470, 1990.

[37] N. R. S. Simons, "Development and application of differential-equation based numerical techniques to electromagnetic scattering and radiation problems," PhD Dissertation, Department of Electrical and Computer Engineering, University of Manitoba, 1994.

[38] L. de Menezes and W. J. R. Hoefer, "Modeling frequency dependent dielectrics in TLM," *IEEE Antennas Propagat.-S Symp.* Dig., pp. 1140-1143, 1994.

[39] L. de Menezes and W. J. R. Hoefer, "Modelling nonlinear media in 2D-TLM," *24th European Microwave Conference Proc.*, pp. 1739-1744, 1994.

[40] L. de Menezes and W. J. R. Hoefer, "Modelling of general constitutive relationships in SCN TLM," *IEEE MTT-S Symp.* Dig., pp. 365-368, 1995.

[41] L. de Menezes and W. J. R. Hoefer, "Modelling anistropic dispersive materials in TLM," *First International Workshop on Transmission line Matrix (TLM) Modeling-Theory and Applications*, pp.91-94, 1995.

[42] L. de Menezes and W. J. R. Hoefer, "Modeling gyromagnetic media in symmetrical condensed node TLM," *IEEE MTT-S Symp.* Dig., pp. 294-301, 1997.

[43] L. de Menezes and W. J. R. Hoefer, "Modeling of general constitutive relationships in SCN TLM," *IEEE Trans. Microwave Theory Tech.*, vol. 44, pp. 854-861, 1996.

[44] A. M. Portis, *Electromagnetic Fields Sources and Media*, John Wiley & Sons, New York, 1978.

[45] L. Chua, C. Desoer and E. Kuh, *Linear and Nonlinear Circuits*, McGraw-Hill, NewYork, 1987.

[46] C. Gerald and P. Wheatley, *Applied Numerical Analysis*, Addison-Wesly, Massachusetts, 1984.

[47] C. H. Durney, P. W.Johnson, H. Massoudi, J. L. Lords, D. K. Ryser, S. J. Allen and J. C. Mitchell, *Radiofrequency Radiation Dosimetry Handbook*, USAF school of Aerospace Medicine, Brooks AFB, TX, Rep. USAF SAM-TR-85-73, 1986.

[48] R. Luebbers, H. P. Forrest, S. K. Kunz, R. B. Standler and M. Schneider, "A frequency–dependent finite-difference time-domain formulation for dispersive materials," *IEEE Trans. Electromag. Compat.*, vol. 32, pp. 222-227, 1990.

[49] M. D. Bui, S. S. Stuchly, and G. I. Costache, "Propagation of transients in dispersive dielectric media," *IEEE Trans. Microwave Theory Tech.*, vol. 39, pp. 1165-1172, 1991.

[50] R. J. Luebbers, H. P. Forrest and K. S. Kunz, "A frequency–dependent finite-difference time-domain formulation for transient propagation in plasma," *IEEE Trans. Antennas Propagat.*, vol. 39, pp. 29-34, 1991.

[51] R. Luebbers, D.Steich and K. Kunz, "FDTD calculation of scattering from frequency-dependent materials," *IEEE Trans. Antennas Propagat.*, vol. 41, pp. 1249-1257, 1993.

[52] D. M. Sullivan, "A frequency-dependent FDTD method for biological applications," *IEEE Trans. Microwave Theory Tech.*, vol. 40, pp. 532-539, 1992.

[53] T. Kashiwa, N. Yoshida, and I. Fukai, "A treatment by the finite-difference time-domain method of the dispersive characteristics associated with orientation polarization," *Trans. IEICE*, vol. E73, pp. 1326-1328, 1990.

[54] T. Kashiwa and I. Fukai, "A treatment by the FD-TD method of the dispersive characteristics associated with electronic polarization," *Microwave Opt. Technol. Lett.*, vol. 3, pp. 203-205, 1990.

[55] T. Kashiwa, Y. Ohtomo, and I. Fukai, "A finite-difference time-domain formulation for transient propagation in dispersive media associated with Cole-Cole's circular ARC law," *Microwave Opt. Technol. Lett.*, vol. 3, pp. 416-419, 1990.

[56] R. M. Joseph, S. C. Hagness, and A. Taflove, "Direct time integration of Maxwell's equations in linear dispersive media with absorption for scattering and propagation of femtosecond electromagnetic pulses," *Optics Lett.*, vol. 16, pp. 1412-1414, 1991.

[57] P. M. Goorjian and A. Taflove, "Direct time integration of Maxwell's equations in nonlinear dispersive media for propagation and scattering of femtosecond electromagnetic solitons," *Optics Lett.*, vol. 17, pp. 180-182, 1992.

[58] O. P. Gandhi, B. Q. Gao, and J. Y. Chen, "A frequency-dependent finite-difference time-domain formulation for induced current calculations in human beings," *Bioelectromagnetics*, vol. 13, no. 6, pp. 543-556, 1992.

[59] O. P. Gandhi, B. Q. Gao and J. Y. Chen, "A frequency dependent finite difference time domain formulation for general dispersive media," *IEEE Trans. Microwave Theory Tech.*, vol. 41, pp. 658-665, 1993.

[60] O. P. Gandhi and C. M. Furse, "Currents induced in the human body for exposure to ultrawideband electromagnetic pulses," *IEEE Trans. Electromag Compat.*, vol. 39, pp. 174-180, 1997.

[61] I. El-Babli, A. Sebak and N. Simons, "Application of the TLM method to the interaction of EM fields with dispersive dielectric bodies," *IEE Proc. Microw Antennas Propag.*, vol. 147, pp. 211-217, 2000.

[62] J. Chen, J. M. Jin, H. Gan and W. C. Chew, "Analysis of electromagnetic wave interaction with biological tissue using CG-FFT method," *IEEE Antennas Propagat. Symp.*, pp. 1814-1817, 1996.

[63] L. de Menezes, "Modeling of general medium cConstitutive relationships in the transmission line matrix method (TLM)," PhD Dissertation, Department of Electrical and Computer Engineering, University of Victoria, 1996.

[64] I. El-Babli and A. Sebak, "Unrelated illumination approach for the reconstruction of three-dimensional inhomogeneous dielectric bodies," *J. Electromagn. Waves Applic.*, vol. 12, pp. 371-385, 1998.

[65] M. Jensen and Y. Rahmat-Samii, "EM interaction of handset antennas and a human in personal communications," *Proc. IEEE*, vol. 83, pp. 7-17, 1995

[66] M. A. Stuchly and S. S. Stuchly, "Dielectric properties of biological substances tabulated," *J. Microwave Power*, vol. 15, pp.19-26, 1980.

[67] C. A. Balanis, H. W. Hill and R. D. Roger, "Radio-frequency imaging in geophysical applications," *J. Microwave Power*, vol. 18, pp.83-93, 1983.

[68] O. Yue, E. L. Rope and G. Tricoles, " Two reconstruction methods for microwave imaging of buried anomalies," *IEEE Trans. Comp.*, vol. C-24, pp. 381-390, 1975.

[69] N. H. Farhat, "High resolution microwave holography and the imaging of remote moving objects," *Optical Engrg.*, vol. 14, pp. 499-505, 1975.

[70] L. E. Larsen and J. H. Jacobi, *Medical Applications of Microwave Imaging*, IEEE press, New York, 1986.

[71] J. C. Lin and M. J. Clarke, "Microwave imaging of cerebral edema," *Proc. IEEE*, vol. 70, pp. 523-524, 1982.

[72] M. F. Iskander, R. Maini, C. H. Durney, and D. G. Bragg, "A microwave method for measuring changes in lung water," *IEEE Trans. Biomed. Eng.*, vol. BME-28, pp. 797-804, 1981.

[73] E. Wolf, "Three-dimensional structure determination of semitransparent objects from holographic data," *Opt. Commun.*, vol. 1, pp. 153-156, 1969.

[74] R. K. Muller, M. Kaveh, and G. Wade, "Reconstructive tomography and applications to ultrasonics," *Proc. IEEE*, vol. 67, pp. 567-587, 1979.

[75] M. Slaney, A. C. Kak, and L. E. Larsen, "Limitations of imaging with first order diffraction tomography," *IEEE Trans. Microwave Theory Tech.*, vol. MTT-32, pp. 860-873, 1984.

[76] J. V. Candy, and C. Pichot, "Active microwave imaging: a model based approach," *IEEE Trans. Antennas Propagat.*, vol. AP-39, pp. 285-290, 1991.

[77] F. C. Lin, and M. A. Fiddy, "Image estimation from scattered field data," *Int. J. Imaging Syst. Technol.*, vol. 2, pp. 76-95, 1990.

[78] L. Joffre, M. S. Hawley, A. Broquetas, E. Delos Reyes, M. Ferrando, and A. R. Elias-Fuste, "Medical imaging with microwave tomographic scanner," *IEEE Trans. Biomed. Eng.*, vol. BME-37, pp. 303-312, 1990.

[79] M. Slaney, M. Azimi, A. C. Kak, and L. E. Larsen, "Microwave imaging with first order diffraction tomography," Medical Applications of Microwave Imaging, L. E. Larsen and J. H. Jacobi Ed., pp.184-212, 1986.

[80] D. K. Ghodgaonkar, O. P. GandhI, and M. J. Hagmann, "Estimation of complex permittivities of three-dimensional inhomogeneous biological bodies," *IEEE Trans. Microwave Theory Tech.*, vol. MTT-31, pp. 442-446, 1983.

[81] M. M. Ney, A. M. Smith, and S. S. Stuchly, "A solution of electromagnetic imaging using pseudo-inverse transformation," *IEEE Trans. Med. Imaging*, vol. MI-3, pp. 155-162, 1984.

[82] C. N. Dorny, *A Vector Space Approch to Models and Optimization*, Huntigton, New York: Krieger, 1980.

[83] S. Coarsi, G. L. Gragnani, and M. Pastorino, "Electromagnetic vision-oriented numerical solution to three-dimensional inverse scattering," *Radio Sci.*, vol. 23, pp. 1094-1106, 1988.

[84] S. Coarsi, G. L. Gragnani, and M. Pastorino, "Equivalent current density reconstruction for microwave imaging purpose," *IEEE Trans. Microwave Theory Tech.*, vol. MTT-37, pp. 910-916, 1989.

[85] S. Coarsi, G. L. Gragnani, and M. Pastorino, "Two-dimensional microwave imaging by a numerical inverse scattering solution," *IEEE Trans. Microwave Theory Tech.*, vol. MTT-38, pp. 981-989, 1990.

[86] S. Coarsi, G. L. Gragnani, and M. Pastorino, "An approach to microwave imaging using a multiview moment method solution for a two-dimensional finite cylinder," *IEEE Trans. Microwave Theory Tech.*, vol. MTT-39, pp. 1062-1067, 1991.

[87] S. Coarsi, G. L. Gragnani, and M. Pastorino, "Redundant electromagnetic data for microwave imaging of three-dimensional dielectric objects," *IEEE Trans. Antennas Propagat.*, vol. AP-42, pp. 581-589, 1994.

[88] S. Coarsi, S. Ciaramella, and L. Gragnani, "On the use of regularization techniques in numerical inverse-scattering solutions for microwave imaging applications," *IEEE Trans. Microwave Theory Tech.*, vol. MTT-43, pp. 632-640, 1995.

[89] Y. M. Wang, and W. C. Chew, "An iterative solution of two-dimensional electromagnetic inverse scattering problem," *Int. J. Imaging Syst. Technol.*, vol. 1, pp. 100-108, 1989.

[90] Y. M. Wang, and W. C. Chew, "Reconstruction of two-dimensional permittivity distribution using the distorted Born iterative method," *IEEE Trans. Med. Imaging*, vol. 9, pp. 218-225, 1990.

[91] N. Joachimowicz, C. Pichot, and J. P. Hugonin, "Inverse scattering: an iterative numerical method for electromagnetic imaging," *IEEE Trans. Antennas Propagat.*, vol. AP-39, pp. 1742-1752, 1991.

[92] A. N. Tikhonov and V. Y. Arsenin, *Solution of Ill-Posed Problems*, V. H. Winston & Sons, 1977.

[93] Y. Liu, and I. R. Ciric, "A more convergent iterative algorithm for electromagnetic imaging," *IEEE Trans. Magnetics*, vol. 31, pp. 1302-1305, 1995.

[94] I. R. Ciric, and Y. Liu, "An adaptive algorithm for electromagnetic imaging," *IEEE Trans. Magnetics*, vol. 32, pp. 1302-1305, 1996.

[95] A. Franchois, and C. Pichot, "Microwave imaging-complex permittivity reconstruction with a Levenberg-Marquardt method," *IEEE Trans. Antennas Propagat.*, vol. AP-45, pp. 203-215, 1997.

[96] M. M. Ney, "Method of moments as applied to electromagnetic problems," *IEEE Trans. Microwave Theory Tech.*, vol. MTT-33, pp. 972-980, 1985.

[97] P. Lobel, R. Kleinman, C. Pichot, L. Feraud, and M. Barlaud, "Conjugate gradient method for solving inverse scattering with experimental data," *IEEE Antennas Propagat. Mag.*, vol. 38, pp. 45-51, 1996.

[98] P. Lobel, C. Pichot, L. Feraud, and M. Barlaud, "Conjugate gradient algorithm with edge-preserving regularization for image reconstruction from experimental data," *IEEE AP-S Int. Symp.*, vol. 1, pp. 644-647, Baltimore, USA, 1996.

[99] P. M. Meaney, K. D. Paulsen, and T. R.Ryan, "Two-Dimensional hybrid element image reconstructed for TM illumination," *IEEE Trans. Antennas Propagat.*, vol. AP-43, pp. 239-247, 1995.

[100] Y. Qin, I. R. Ciric, "High resolution electromagnetic imaging of lossy objects in the presence of noise," *IEEE Trans. Magnetics*, vol. 31, pp. 1936-1939, 1995.

[101] Y. Qin, I. R. Ciric, "Efficient techniques for choosing the regularization parameter for electromagnetic imaging," *Proc. ANTEM'96*, 1996, (Montreal, Canada).

[102] Y. Qin, I. R. Ciric, "Method of selecting regularization parameter for microwave imaging," *Electron. Letters*, vol. 30, pp. 2028-2029, 1994.

[103] M. Baribaud, "Microwave imagery: analytical method and maximum entropy method," *J. Appl. Phys.*, vol. 23, pp. 269-287, 1990.

[104] L. Garnero, A. Franchois, J. P. Hugonin, C.Pichot, and N. Joachimowicz, "Microwave imaging-complex permittivity reconstruction by simulated annealing," *IEEE Trans. Microwave Theory Tech.*, vol. MTT-39, pp.1801-1807, 1991.

[105] S. Coarsi, G. L. Gragnani, S. Medicina, M. Pastorino, and G. Zunino, "Microwave imaging method using a simulated annealing approach," *IEEE Microwave Guided Wave Letters*, vol. 1, pp. 331-333, 1991.

[106] J. Hadamard, *Lectures on Chauchy's Problem in Linear Partial Differential Equations*, New Haven, CT: Yale Univ. Press, 1923.

[107] W. Weiyan, and Z. Shourong, "Unrelated illumination method for electromagnetic inverse scattering of inhomogeneous lossy dielectric bodies," *IEEE Trans. Antennas Propagat.*, vol. 40, pp. 1292-1296, 1992.

[108] C. Chiu and R. Yang, "Image reconstruction for inhomogeneous biaxial dielectric cylinders," *Antennas Propagat Int. Sy*mp., vol. 3, pp. 1978-1981, 1994.

[109] R. E. Jong A Keim, "Electromagnetic radiation absorption in block models of human bodies," M.Sc. thesis, Florida Atlantic Univ., 1988.

[110] D. E. Livesay, and K. Chen, "Electromagnetic fields induced inside arbitrarily shaped biological bodies," *IEEE Trans. Microwave Theory Tech.*, vol. MTT-22, pp. 1273-1280, 1974.

[111] T. K. Sarkar, D. D. Weiner, and V. K. Jain, "Some mathematical considerations in dealing with inverse problems," *IEEE Trans. Antennas Propagat.*, vol. AP-29, pp. 373-37, 1981.

[112] M. Moghaddam, and W. C. Chew, "Study of some practical issues in inversion with the Born iterative method using time-domain data," *IEEE Trans. Antennas Propagat.*, vol. AP-41, pp. 177- 184, 1993.

[113] D. O. Batrakov, and N. P. Zhuk, "An iterative solution to the inverse problem of remote sensing of nonuniform media based on values of the polarization parameters" *J. Commun. Tech. Elec.*, vol. 38, pp. 108-115, 1993.

[114] D. O. Batrakov, and N. P. Zhuk, "Solution of a general inverse scattering problem using the distorted Born approximation and iterative technique," *Inverse Problems*, vol. 10, pp. 39-54, 1994.

[115] C. A. Balanis, *Antenna Theory Analysis and Design*, John Wiley & Sons, New York, 1997.

[116] R. C. Hansen, *Phased Array Antennas*, John Wiley & Sons, New York, 1998.

[117] R. C. Hansen and D. Gammon, "Superdirective linear arrays with uniform amplitudes," *Microwave Opt. Technol. Lett.*, vol. 20, pp. 28-31, 1999.